University of Strathclyde

Department of Naval Architecture, Ocean and Marine Engineering

Peridynamic Modelling of Localised Corrosion Damage

By

Dennj De Meo

A thesis submitted in fulfilment of the requirements for the degree of Doctor of Philosophy

Glasgow, U.K.

September, 2016

AUTHOR STATEMENT

This thesis is the result of the author's original research. It has been composed by the author and has not been previously submitted for examination which has led to the award of a degree.

Signed: Date:

ACKNOWLEDGEMENTS

I desire to express my deepest gratitude to my supervisor, Dr. Erkan Oterkus, who taught me how to carry out scientific research, guided me through the years of my PhD with dedication, passion, kindness and total availability to discuss technical and personal issues, and allowed me to enjoy my research in full freedom. I'm also grateful to him for the encouragement and all the opportunities he gave me to develop my communication skills through the writing of journal papers, conference papers, grant proposals and one chapter book, and the preparation and delivery of several presentations at the PMMA research group and at various exhibitions and meetings between industry, research centers and universities. I consider myself lucky for having met Dr. Oterkus at such a critical moment of my professional career. I would like to thank also Prof. Atilla Incecik, for his support, feedback and encouragement during the realisation of this work.

I'm also grateful to Prof. Siegfried Schmauder, Prof. Erdogan Madenci and Dr. Julia Race for the useful discussions occurred during the realisation of this work.

I'm particularly grateful to the Commonwealth Scientific and Industrial Research Organisation (CSIRO) Manufacturing Division in Clayton (Melbourne) for having hosted me for a month during the final stage of my PhD. In particular, I want to thank Prof. Ivan Cole for his support, kindness, encouragement and for having shared with me his deep knowledge and experience in the field of corrosion modelling. I also thank Dr. Fiona Chen for the useful discussions and suggestions about the numerical modelling of pitting corrosion. A special thank goes to my supervisor at CSIRO, Dr. Dayalan Gunasegaram, for his generosity, kindness, technical support and guidance during my studies at CSIRO. His supervision could not been better. I also want to thank all the other members of the research group, who made me feel part of the team since the first day I arrived at CSIRO.

I acknowledge the anonymous reviewers of the journal papers published as outcome of this research, whose time and contribution have been highly appreciated and have elevated the value of this work.

The financial support of the Defense Science and Technology Laboratory (Dstl) and the University of Strathclyde is also acknowledged.

I thank all the staff of the Naval Architecture, Ocean and Marine Engineering Department, Thelma and all my colleagues, which have always been collaborative, helpful and supportive, and have contributed in making the department a friendly and pleasant environment to work.

My family and my friends deserve a special thank. Their love and support helped me in overcoming the challenges I faced during my PhD.

Finally, I thank God for my splendid life, my health and for his blessing.

"There is nothing noble about being superior to another man; the true nobility lies in being superior to your previous self."

Upanishads

To Agata,
To Gerardo,
for your example and unconditional love and support

ABSTRACT

Due to their unpredictability, rapid growth and difficulty of detection, localised forms of corrosion represent a threat to human life and the environment. The current empirical and semi-empirical approaches used by engineers to hinder corrosion damage have several disadvantages and limitations. In this regard, numerical approaches can be a valuable complement. However, the majority of the numerical techniques currently available in the literature are based on partial differential equations, which become invalid in the presence of field's discontinuities such as cracks and sharp concentration gradients. In order to overcome these limitations, a recently introduced continuum theory of mechanics based on integro-differential equations, peridynamics, is used for the first time for the modelling of polycrystalline fracture, stress-corrosion cracking, pitting corrosion and crack propagation from corrosion pits in steels exposed to different corrosive environments. The results are validated against experimental data and other numerical results. It was found that the microstructure can have a significant impact on the fracture behaviour of the material, and that aqueous solutions of sulfuric acid can lead to an embrittlement of high-strength steels so severe that the material can fail at stress intensity factors even four times smaller than the value of the fracture toughness. It was also found that peridynamics can be successfully used to reproduce realistic pit morphologies and to model microstructural effects, such as the presence of clusters of cathodic intermetallic particles, which can channel the propagation of corrosion pits. Finally, it was demonstrated that peridynamics can also be used to simulate crack nucleation and propagation from corrosion pits, without the need for any assumption on the location of crack nucleation, which, in contrast, is needed when using other numerical techniques. In conclusion, the results of this study support the idea that the peridynamic models produced as part of this research can be helpful in failure analysis and in the microstructural design of new fracture-resistant and corrosion-resistant materials.

TABLE OF CONTENTS

LIST OF FIGURES

LIST OF TABLES

ABBREVIATIONS

304 SS	Stainless steel grade 304
AIDEC	Adsorption-induced decohesion
BCC	Body-centered cubic
BEM	Boundary element method
CAD	Computer-aided design
CCM	Classical continuum mechanics
CP	Cathodic protection
CRAs	Corrosion-resistant alloys
CZM	Cohesive zone model
DFT	Density functional theory
EDL	Electric double layer
EOM	Equation of motion
FEM	Finite element method
GB	Grain boundary
GBC	Grain boundary coefficient
GI	Grain interior
HE	Hydrogen embrittlement

HSLA	High-strength low-alloy
IMPs	Intermetallic particles
I-SCC	Intergranular stress-corrosion cracking
PD	Peridynamics
PDEs	Partial differential equations
SCC	Stress-corrosion cracking
SIF	Stress intensity factor
T-SCC	Transgranular stress-corrosion cracking
UBER	Universal binding energy relation

NOMENCLATURE

$\mathbf{x}$	Vector defining the position of a generic material point in the undeformed configuration
$\mathbf{x}'$	Vector defining the position of a generic neighbour of material point $\mathbf{x}$ in the undeformed configuration
$\mathbf{y}$	Vector defining the position of a generic material point in the deformed configuration
$\mathbf{y}'$	Vector defining the position of a generic neighbour of material point $\mathbf{y}$ in the undeformed configuration
$\mathrm{d}V_{\mathbf{x}'}$	Infinitesimal volume associated with material point $\mathbf{x}'$ [m^3]
$\rho(\mathbf{x})$	Density associated with material point $\mathbf{x}$ [Kg/m^3]
$\ddot{\mathbf{u}}(\mathbf{x},t)$	Acceleration associated with material point $\mathbf{x}$ [m/s^2]
σ	Stress tensor [N/m^2]
t	Time [s]
$\nabla\cdot$	Divergence operator
$\mathbf{b}(\mathbf{x},t)$	Body force acting on material point $\mathbf{x}$ [N/m^3]
$\mathbf{f}$	Mechanical response function [N/m^6]
$\mathbf{u}(\mathbf{x},t)$	Displacement of material point $\mathbf{x}$ [m]
$H_{\mathbf{x}}$	Horizon

δ	Radius of the horizon [m]
c	Bond constant [N/m^6]
s	Stretch
s_0	Critical stretch
s_0^*	Effective critical stretch
Δ	Grid space [m]
$\mathbf{x}_i$	Vector defining the position of the generic particle "*i*"
M	Number of family members
V_j	Volume of the generic particle "*j*"
v_c	Volume correction factor
s_{cf}	Surface correction factor
n_t	Current time step
n_{t+1}	Next time step
θ	Angle between fiber bonds and the crystal orientation [rad]
γ	Crystal orientation angle [rad]
C_{ij}	Elastic moduli [N/m^2]
c_{T1}	Type-1 bond constant [N/m^6]
c_{T2}	Type-2 bond constant [N/m^6]

h	Thickness of the body [m]
L	Length of the body [m]
W	Width of the body [m]
A	Surface area of the body [m^2]
ξ_{ij}	Length of the bond between particles "*i*" and "*j*" [m]
q_A	Number of PD bonds along directions A
q_B	Number of PD bonds along directions B
E	Young's modulus [N/m^2]
ν	Poisson's coefficient
G_c	Critical energy release rate [N/m]
K_{Ic}	Fracture toughness [MPa$\sqrt{\text{m}}$]
K_{Ic}^*	Effective fracture toughness [MPa$\sqrt{\text{m}}$]
$s_{0\,GB}$	Grain boundary critical stretch
$s_{0\,GI}$	Grain interior critical stretch
P	Mechanical load [N/m^2]
V	Velocity boundary condition [m/s]
dt	Time step size [s]

χ	Fracture toughness coefficient
D_{GB}	Grain boundary diffusion coefficient [m^2/s]
C_H	Hydrogen concentration [mol/m^3]
∇	Nabla operator
f_H	Hydrogen diffusion response function [$mol/(m^6 s)$]
d_{GB}	Grain boundary hydrogen diffusion bond constant [$m^{-2}s^{-1}$]
ψ	Hydrogen coverage
C_{SH}	Surface hydrogen concentration [mol/m^3]
C_{SH}^*	Surface hydrogen concentration saturation value [mol/m^3]
$\sigma_c(\psi)$	Critical stress [N/m^2]
u	Displacement-controlled load [m]
e	Electron
n	Valence number
ϕ	Electric potential [V]
i_0	Exchange current density [A/m^2]
η	Overpotential [V]
G	Gibbs energy [J]
ΔG^*	Free energy of activation [J]

T	Temperature [K]
R	Universal gas constant
E	Electrode potential [V]
E_0	Equilibrium electrode potential [V]
α	Transfer coefficient
i_a	Anodic current density [A/m^2]
F	Faraday's constant
β_a	Tafel constant
D_i	Diffusion coefficient of the generic specie "*i*"
C_i	Concentration of the generic specie "*i*"
U	Flow velocity [m/s]
D_{ld}	Effective diffusion coefficient in the liquid [m^2/s]
D_{sd}	Effective diffusion coefficient in the solid [m^2/s]
C_{MI}	Concentration of metal ions [mol/m^3]
M_{ol}	Number of moles [mol]
v_{int}	Velocity of the liquid/solid interface [m/s]
C_{solid}	Concentration of metal ions in the solid [mol/m^3]
C_{liquid}	Concentration of metal ions in the liquid [mol/m^3]

f_d	Metal dissolution response function
d_{MI}	Metal ions diffusion bond constant
D_{eff}	Effective diffusion coefficient [m^2/s]
l_{ij}	Length of the bond between particles "*i*" and "*j*"
$d(\mathbf{x},t)$	Damage index
N_f	Number of broken bonds of a generic particle
N_{tot}	Total number of bonds of a generic particle
P_r	Probability of bond rupture
d_{ANSYS}	Real constant for COMBIN14 elements in ANSYS
D_{sd}^*	Artificial effective coefficient of diffusion in the solid [m^2/s]
c_{pm}	Coefficient of pit morphology
W_{PD}	PD strain energy density [J/m^3]
W_{CCM}	CCM strain energy density [J/m^3]

1 INTRODUCTION

This chapter is divided in four sections. In the first part (Section 1.1), some basic information about corrosion is given, the cost of corrosion, its impact on society and the most popular corrosion control measures currently used by engineers are discussed. The limitations of these techniques are highlighted and the need for further research and numerical models of corrosion is explained. Peridynamics is introduced and the benefits of using this theory for the motivation of this research are described. In the second part (Section 1.2), the objectives of this research study are highlighted, while, in the third part (Section 1.3), the structure of the thesis is presented. Finally, a summary of the information contained in this chapter is given in Section 1.4.

1.1 Background and motivation

Corrosion is a natural process that can be described as the chemical (in the case of dry corrosion) or electrochemical (in the case of wet corrosion) reaction of an engineering material with the environment, which eventually leads to the deterioration of its mechanical properties. It's interesting to note that, as mentioned in (Groysman 2010), the term "corrosion" comes from the Latin word "corrodere", which means "to eat away". Some metals are called "noble" (e.g. gold, platinum, silver) because they have a low tendency to react with the environment. This is due to the fact that these metals are often found in nature in their pure form. In contrast, non-noble elements (e.g. iron, aluminium, titanium) are more reactive and, for this reason, they are usually found in nature in the form of metallic ores. In order to extract the metal (e.g. iron) from its ore, energy needs to be provided during the extraction process. The metal so created is therefore thermodynamically instable and in time it will naturally tend to come back to its original ore condition. The job of the corrosion control engineer is to prevent and hinder this natural phenomenon.

There are several types of corrosion mechanisms and, in regard to the form of the attack, they can be classified under uniform or general corrosion and localised corrosion. Due to their high unpredictability, rapid growth and difficulty of detection, the corrosion mechanisms belonging to the latter group generally produce greater concern among engineers. Some of the most common and dangerous localised corrosion mechanisms are stress corrosion cracking (SCC) and pitting corrosion.

The two most important reasons for studying corrosion are: 1) human health and safety and 2) environment protection. Despite the fact that corrosion is a topic that has been widely researched for many years, minor, major and catastrophic failures, which lead to human loss and environmental damage, still occur nowadays in a variety of industries and structures (e.g. bridges, nuclear power plants, aircraft, pipelines, storage tanks, boilers, pressure vessels). A third reason for studying corrosion is the high cost associated with it (e.g. repair, replacement, coating, design of cathodic protection systems, shutdown of industrial plants, loss of product, environmental damage, contamination of product and the use of corrosion inhibitors and corrosion resistant alloys). Indeed, as argued in (Mccafferty 2010), the cost of corrosion is approximately 3-5% of the gross national product of an industrialised nation. Therefore, in qualitative terms, in the UK the cost of corrosion is about 50% that of the national health care system. The fourth reason for studying corrosion is related to the conservation of historic structures and monuments (e.g. the Statue of Liberty and the Eiffel Tower).

The five most popular corrosion control measures are: 1) cathodic protection (CP), 2) corrosion allowance, 3) coating and the use of 4) corrosion inhibitors and 5) corrosion-resistant alloys (CRAs). Despite the usefulness of these techniques, they all have associated costs and they generally have side effects and disadvantages. For example, as argued in (Mccafferty 2010), impressed current cathodic protection systems can lead to hydrogen embrittlement, stray current corrosion and coating debonding. Corrosion inhibitors can be toxic and can have detrimental effects on the

environment. CRAs are more expensive and generally more difficult to weld compared to carbon steel. Corrosion allowance may not be always effective against localised corrosion damage, while coating systems often require the use of strict and specific procedures for surface preparation and coating application, which may be difficult to implement. In fact, as argued in (Black et al. 2015), recent studies have revealed that processing and application errors account for 43-68% of the cases of premature failure of coating systems. Moreover, the introduction of new technologies sometimes poses novel and serious corrosion challenges. For example, as argued in (Black et al. 2015), since the currently available standards for the corrosion protection of offshore wind turbines are widely based on those used for the oil & gas industry, unanticipated corrosion issues have been experienced in recent years. More precisely, the current guidelines and standards for corrosion protection of internal surfaces of monopole structures, which are often used as foundation for offshore wind turbines in shallow water, seem inadequate (Black et al. 2015). Since these structures are unmanned, corrosion monitoring and maintenance is more problematic; certain areas are not even accessible (e.g. the mud zone) and, therefore, corrosion data and rates may not be available. As argued in (Black et al. 2015), in light of this lack of experience and knowledge, currently, many owners prefer to opt for very conservative and costly solutions rather than exposing their asset to the risk of catastrophic failures.

In general, corrosion control strategies are based on tabulated experimental data, the interaction material/environment is not fully understood at present and the limits of acceptable corrosion damage are not well-defined (Black et al. 2015). This stems from the fact that corrosion is a complex phenomenon, which is influenced by several environmental factors (e.g. temperature, pH, concentration of ionic species) and metallurgical variables (e.g. the microstructural features of the material and its properties). Therefore, in order to overcome the difficulties encountered in experimental investigations, numerical modelling of corrosion is often used to gain insight into the roles of the various variables contributing to the overall corrosion

behaviour of materials, with the ultimate goal of designing corrosion-resistant materials and predicting corrosion damage.

Several numerical approaches are available in the literature for the modelling of corrosion damage (vid. Chapter 2), and many of them are based on the theory of classical continuum mechanics (CCM), whose mathematical formulation is described by partial differential equations, which become invalid in the presence of field's discontinuities such as cracks and sharp concentration gradients (vid. Chapter 2). In this study, with the aim to overcome this limitation, a recently introduced continuum theory of mechanics based on integro-differential equations, peridynamics (PD), is used for the modelling of fracture in polycrystalline materials, and structural damage produced by various localised forms of corrosion, i.e. stress-corrosion cracking, pitting corrosion and crack propagation from corrosion pits in steels exposed to different corrosive environments.

1.2 Objectives of research

The research described in this thesis has four main objectives:

- Creation of a numerical model based on PD theory for the investigation of the microstructural fracture behaviour of cubic polycrystals, which are commonly found in nature (e.g. iron, chromium, tungsten, copper, aluminium, silver, gold). This framework is used as starting point for the creation of the PD models of SCC and pit-to-crack transition described in Chapter 5 and Chapter 7, respectively. To the best of the author's knowledge, there is currently no study available in the literature concerning the PD modelling of fracture and crack growth in cubic polycrystals that also provides detailed investigation and description of the mathematical formulation. This goal is achieved in (De Meo, Zhu, et al. 2016) as part of the research described in this thesis (Chapter 4).

- Creation of a numerical model based on PD theory for the investigation of hydrogen grain boundary diffusion, embrittlement, and resulting SCC. To the best of the author's knowledge, this is the first attempt to create a PD framework for the modelling of SCC. The results of this study have been published in (De Meo, Diyaroglu, et al. 2016).

- Creation of a numerical model based on PD theory for the investigation of pitting corrosion (Chapter 6). This work is based on a recent PD model of pitting corrosion, which can be found in (Chen & Bobaru 2015). However, the approach used in the present study is different and offer the advantage of a reduced computational time. Moreover, the capabilities of the numerical framework have been extended to the modelling of 1) realistic pit morphologies and 2) the influence of microstructural features of the material, e.g. intermetallic particles, which were lacking in (Chen & Bobaru 2015). Furthermore, this study forms the foundation of the pit-to-crack transition model presented in Chapter 7.

- Creation of a numerical model based on PD theory for the investigation of pit-to-crack transition (Chapter 7). To the best of the author's knowledge, this is the first time that PD is used to investigate such a problem (De Meo & Oterkus 2016).

In conclusion, the ultimate goal of this research is to produce non-conventional and more effective numerical frameworks that can be helpful in failure analysis and in the design of new fracture-resistant and corrosion-resistant materials.

1.3 Structure of the thesis

This thesis is constituted by the following eight chapters:

- Chapter 1. This chapter provides basic information about corrosion, its impact on society, the current approaches used by engineers to prevent and

hinder corrosion damage and their limitations, which justify the need for further research in this field. In this regard, the benefits of numerical simulations are highlighted and the objectives of research and the organisation of this thesis are described.

- Chapter 2. This chapter provides the historical overview and the advantages and limitations of the most popular numerical techniques used up to now to investigate the four problems considered in this thesis (i.e. fracture of polycrystalline materials, SCC, pitting corrosion and pit-to-crack transition). The limitations of these techniques are used to justify the current numerical approach (i.e. PD). Moreover, the state of the art and the major findings of studies relevant to the problems here considered (i.e. fracture of polycrystalline materials, SCC, pitting corrosion and pit-to-crack transition) are discussed and the current research is put into perspective.

- Chapter 3. This chapter provides basic information about the numerical approach used for investigating the problems considered in this research study (i.e. PD).

- Chapter 4. This chapter describes the PD micro-mechanical model of polycrystalline materials and its mathematical formulation; the related derivation is given in Appendix A. Various static and dynamic loading conditions are considered, results in plane stress and in plane strain configurations are compared and the impact of the following factors on time-to-failure, crack speed, fracture morphology and fracture behaviour of the material is investigated: grain boundary strength, grain size, fracture toughness and grain orientation (De Meo, Zhu, et al. 2016).

- Chapter 5. This chapter describes the PD model of SCC and its mathematical formulation. Loads with various magnitude are considered and the resulting fracture and branching behaviour of the material and the intergranular crack

propagation speed is compared against experimental data available in the literature (De Meo, Diyaroglu, et al. 2016).

- Chapter 6. This chapter describes the PD model of pitting corrosion and its mathematical formulation. The numerical results are discussed and compared against experimental and other numerical data available in the literature.

- Chapter 7. This chapter describes the PD model of pit-to-crack transition and its numerical implementation. Various realistic pit morphologies are considered and a mechanical load is applied to the structure to investigate the phenomenon of crack propagation from corrosion pits (De Meo & Oterkus 2016).

- Chapter 8. This chapter reviews the research objectives, summarises the major findings, highlight the novelty and contribution to the field of this research study, discusses the gaps and the recommended future work, and closes with final remarks.

1.4 Summary

Corrosion is a natural process and the current approaches used by engineers to hinder corrosion damage have several disadvantages and limitations. Due to their unpredictability, rapid growth and difficulty of detection, localised forms of corrosion (e.g. SCC and pitting) are usually considered the most dangerous. The cost of corrosion is high and major structural failures that endanger human lives and the environment still occur nowadays and are often attributed to some form of corrosion or assisted-corrosion mechanism. Further research in this field is therefore needed and numerical techniques can be used to overcome the limitations of experimental investigations. In this study, PD theory is used in order to overcome the major shortcomings of the currently available numerical approaches. This thesis is constituted of eight chapters. The four objectives of this research study are the

modelling of 1) fracture of polycrystalline materials, 2) SCC, 3) pitting and 4) pit-to-crack transition, and the ultimate goal is to produce non-conventional and more effective numerical frameworks that can be helpful in failure analysis and in the design of new fracture-resistant and corrosion-resistant materials.

2 Literature review

2.1 Introduction

The scope of this chapter is to present a summary of the literature review undertaken for the realisation of this work. As already mentioned in Chapter 1, this research aims to produce four different numerical models: 1) PD model for the prediction of fracture and crack growth in polycrystalline materials, 2) PD model of SCC, 3) PD model of pitting corrosion and 4) PD model of pit-to-crack transition. Therefore, the next section (Section 2.2) provides 1) the historical overview of the most popular numerical approaches used up to now to model the problems considered in this work, 2) a discussion on the advantages and limitations of these methods, and 3) a justification for the numerical approach used in this study (i.e. PD). Moreover, the state of the art concerning the numerical modelling of fracture in polycrystalline materials, SCC damage, pitting corrosion damage and pit-to-crack transition, along with a discussion on the major findings of relevant studies, is given in Section 2.3, Section 2.4, Section 2.5 and Section 2.6, respectively. Finally, a summary of the information contained in this chapter is given in Section 2.7.

2.2 Historical overview of numerical methods to predict structural damage

Within the framework of CCM, the most popular numerical approaches used up to now to model the problems described in the next four sections are: the boundary element method (BEM), the finite element method (FEM), the cohesive zone model implemented within the FEM via the use of finite cohesive elements (CZM/FEM) and the extended finite element method (XFEM).

One of the first applications of BEM to solve elastostatic problems can be found in (Rizzo 1967). This numerical technique is considered by many a worthy rival of FEM (Aliabadi & Rooke 1991). As argued in (Sadd 2005), in general BEM presents

two major advantages with respect to FEM: lower computational cost (since only the boundary of the domain needs to be discretized) and greater accuracy (since the inside of the body is not meshed) in modelling problems with high volume/surface ratios (e.g. geomechanics problems). However, additional computation is required if the user wants to know the solution at internal points. Moreover, some years after the publication of the first studies on BEM, it became evident that the numerical formulation of the method was not suitable for modelling problems with discontinuities (e.g. cracks) and, thus, it could not be used straight away in its original formulation for modelling problems such as fracture and crack growth. Therefore, in the subsequent years, several modifications and different approaches were used to overcome this issue. A general overview, a brief description and a discussion of the advantages and limitations of these approaches can be found in (Aliabadi & Rooke 1991).

FEM was one of the first numerical tools used to solve problems involving discontinuous fields. One of the first studies concerning the applications of FEM to solve crack problems can be found in (Swedlow et al. 1965). Similar to BEM, the original formulation of FEM was not adequate to produce reasonable levels of accuracy in proximity to the crack tip (Aliabadi & Rooke 1991) and, therefore, several modifications were implemented in the subsequent years, such as the introduction of special crack tip elements (Tracey 1971) and quarter-point elements (Barsoum 1975). Additional difficulties and limitations were found when researchers decided to move from the modelling of stationary cracks to the modelling of propagating cracks. Indeed, as argued in (Madenci & Oterkus 2014), within the realm of FEM, remeshing is necessary after each incremental crack growth. This is relatively easy to do in case of elastic problems, but for elastic-plastic materials, where stresses and strains are history dependent, remeshing procedures become more problematic since the information of the plastic strain field must be passed to the next meshed model (Anderson 2005).

With the main purpose of overcoming these limitations, the cohesive zone model of fracture mechanics (Dugdale 1960) (Barenblatt 1962) was implemented within the FEM framework by introducing a new type of finite elements: the cohesive zone elements (Hillerborg et al. 1976), which led to the CZM/FEM approach. Despite the significant progress, new limitations were introduced. For example, softening of the material with decreasing mesh size (Madenci & Oterkus 2014) and predetermined crack paths (Anderson 2005) are common with CZM/FEM.

The XFEM (Belytschko & Black 1999) was introduced to overcome these shortcomings and it has been successfully employed until now to solve several problems in the field of materials failure. However, XFEM is not perfect and its major drawbacks are the complexity of the method, the difficulty in handling highly distorted meshes (e.g. problems with large deformations and fragmentation) and the inaccurate predictions of stress intensity factors (Rabczuk et al. 2010).

All the numerical approaches described so far are based on CCM and, therefore, on top of the limitations above mentioned and specific to the particular numerical technique, they also present intrinsic drawbacks. For instance, the basic assumption of CCM is that the solid remains continuous as it deforms; therefore, its mathematical formulation becomes invalid in the presence of discontinuities (e.g. cracks) (Madenci & Oterkus 2014). This obstacle may be overcome by adopting external crack growth criteria based on fracture mechanics that inform the numerical model. However, this solution is not always viable and presents several drawbacks. Firstly, kinetic fracture criteria are not available for novel materials and are generally difficult to obtain and time consuming. Secondly, the fracture behaviour of materials can be significantly influenced by several factors (e.g. grain boundaries, grain size, voids, grain orientation, second phases, microcracks, dislocations, structural ageing) and, therefore, the experimental investigation can become cumbersome. Thirdly, the majority of the studies based on fracture mechanics focus on crack propagation rather than crack nucleation (Madenci & Oterkus 2014). These limitations can be overcome by considering atomistic models, but the computational

power necessary to perform this type of simulations at engineering lengthscales and timescales is still lacking (Van der Weeën et al. 2014).

With the aim of overcoming these limitations, a generalisation of CCM theory, PD theory, was presented for the first time in (Silling 2000). PD is a non-local continuum theory, whose governing equations are integro-differential rather than partial-differential (vid. Chapter 3). This represents a formidable advantage when dealing with discontinuous fields. In contrast with CCM, material failure is part of PD formulation and, therefore, PD does not require any external criteria for predicting speed, direction, oscillation, branching, arrest and coalescence of cracks, which naturally nucleates and propagates along the most energetically favourable paths (Madenci & Oterkus 2014). This is the reason why PD is chosen for the realisation of this work, where propagating cracks and discontinuous concentration fields are expected. More details about PD can be found in Chapter 3.

2.3 Numerical modelling of fracture and crack growth in polycrystalline materials

As argued in (Sukumar et al. 2003), the use of FEM for studying the problem of fracture and crack growth in polycrystalline materials has been hindered by the limitations of the computational techniques mentioned in Section 2.2. The majority of the numerical studies carried out so far is based on XFEM and BEM, but the most popular approach seems to be CZM/FEM (Sfantos & Aliabadi 2007b).

In the realm of cohesive failure models, the linear law presented in (Camacho & Ortiz 1996) and (Ortiz & Pandolfi 1999), and the potential-based laws described in (Tvergaard 1990) and (Xu & Needleman 1996) are probably the most popular (Sfantos & Aliabadi 2007a) (Benedetti & Aliabadi 2013). For instance, the studies described in (Espinosa & Zavattieri 2002b) (Espinosa & Zavattieri 2002a) and in (Wei & Anand 2004) are based on the above mentioned cohesive laws implemented in a CZM/FEM framework. The first two studies analyse the mechanical response of

alumina to quasi-static and dynamic loads; the authors concluded that the fracture toughness of the material has a significant influence on the crack density evolution and the crack pattern. The latter study, which focuses on the fracture response of nanocrystalline nickel in simple tension, concludes that the macroscopic stress-strain response of the material is determined by the competition grain interior/grain boundary deformation. A significant progress was made with the introduction of multiscale CZM/FEM models, e.g. (Zeng & Li 2010) and (Qian & Li 2011),where, in contrast with the conventional models based on cohesive laws, the interface constitutive relationship changes from interface to interface for taking into account local effects and stress states (Qian & Li 2011). The study presented in (Lin et al. 2015) investigated the role of cohesive law parameters on fracture pattern and fracture modes of polycrystalline alumina in the realm of CZM/FEM.

The cohesive laws above mentioned are also used within the BEM 2D framework in the study reported in (Sfantos & Aliabadi 2007a) where, as argued by the authors, the BEM is used for the first time for simulating intergranular fracture in polycrystalline materials. This model was then extended to 3D in the study reported in (Benedetti & Aliabadi 2013). In contrast, the study reported in (Sukumar et al. 2003) investigated the intergranular and transgranular fracturing of brittle polycrystalline materials by using XFEM.

The first numerical results concerning the PD modelling of fracture in polycrystalline materials (silicon polycrystal) was presented in (Askari et al. 2008) where, however, no detailed investigation and formulation were provided. The study concludes that a transition from transgranular to intergranular fracture mode occurs when the grain boundary toughness is inferior to the grain interior toughness. A novel peridynamic formulation for hexagonal crystals was given in (Ghajari et al. 2014), where the fracture behaviour of alumina polycrystals is analysed and similar conclusions to the first peridynamic study (Askari et al. 2008) were drawn. However, to the best of the author's knowledge, there is currently no study available in the literature concerning the PD modeling of fracture and crack growth in cubic

polycrystals that also provides detailed investigation and description of the formulation. This goal has been achieved in (De Meo, Zhu, et al. 2016) as part of the research described in this thesis (vid. Chapter 4).

2.4 Numerical modeling of SCC

Several mechanisms (individually or combined) can lead to SCC and they are generally grouped in different categories (vid. Section 5.2). One of these categories is represented by hydrogen-based mechanisms. As argued in (Lynch 2011b), for those materials that are often found to suffer from SCC hydrogen-based mechanisms during their service (e.g. high strength steels, nickel alloys, titanium alloys, aluminium alloys and magnesium alloys), the mechanisms of SCC and hydrogen embrittlement (HE) are basically the same. The PD model described in Chapter 5 concerns with a specific SCC hydrogen-based mechanism and, thus, the literature review here presented focuses on numerical models of HE.

One of the first FEM models for the study HE was described in (Sofronis & McMeeking 1989), where the transport of hydrogen near a blunting crack tip was analysed. It was concluded that hydrogen traps produced by plastic strain and not hydrogen accumulation at lattice sites encouraged by tensile hydrostatic stress is the predominant mechanism for the determination of hydrogen distribution. The FEM model proposed in (Krom et al. 1999) extends the work described in (Sofronis & McMeeking 1989) by including a strain rate factor that lead to a correct hydrogen balance; it was concluded that, in contrast to the hydrogen concentration at trap sites, the hydrogen concentration at lattice sites is significantly influenced by the strain rate. The CZM/FEM model described in (Liang & Sofronis 2003) couples mechanisms of hydrogen transport (Krom et al. 1999) (Sofronis & McMeeking 1989) and interfacial decohesion in the presence of hydrogen in a nickel-base alloy 690. The authors concluded that, due to high concentration gradients, hydrogen tends to migrate to freshly generated intergranular cracks, which are further encouraged to propagate due to the cohesion reduction action of hydrogen (i.e.

hydrogen embrittlement). A significant progress was made with the study reported in (Serebrinsky et al. 2004) based on CZM/FEM, where first-principle calculations and upscaling renormalisation were used for describing the reduction of cohesive energy due to the presence of hydrogen in high strength steels. However, as highlighted by the authors, microstructural effects were not explicitly taken into account and, as a result, the applicability of the model was limited. Indeed, according to the numerical model of HE reported in (Jothi et al. 2014), inhomogeneous stresses and, as a result, non-uniform hydrogen accumulation, are generated within polycrystalline materials even if the external load applied to the structure is uniform. The work described in (Rimoli & Ortiz 2010) represents an important step forward in addressing this shortcoming within the framework of CZM/FEM. Indeed, this study includes additional features such as grain boundary hydrogen diffusion, multiscale analysis and the explicit modelling of the polycrystalline structure of the material. In the same direction, another work worth of note is the microstructural numerical model reported in (Wu & Zikry 2015), which predicts hydrogen diffusion and embrittlement in martensitic steels and concludes that HE encourages crack propagation, which occur earlier, at lower strain values and with a smaller crack opening displacement compared to the case without hydrogen embrittlement. To the best of the author's knowledge, no PD model currently exists for the investigation of SCC. The first PD model of SCC was published in (De Meo, Diyaroglu, et al. 2016) as part of the research described in this thesis (vid. Chapter 5).

2.5 Numerical modelling of pitting corrosion

As argued in (Cicek 2014), once the pit has been formed, the mechanisms of pitting corrosion and crevice corrosion are considered to be the same. This is the reason why the literature survey described in this section focuses on the numerical modelling of both pitting corrosion and crevice corrosion.

One of the first finite element models developed for predicting the propagation of corrosion crevices and pits is described in (Sharland et al. 1989), where the steady-state electrochemistry of the pit solution in carbon steel is predicted by solving a set of mass-conservation equations. One year later, another steady-state model of pitting and crevice corrosion (Walton 1990) was introduced for iron exposed to acetate and sulphuric acid. The predictions of both models were found to be in good agreement with experimental data. However, as argued in (Walton et al. 1996), since the results produced by these models were steady-state, it was not possible to simulate the transition from a fully passive state (i.e. the passive film protects the underlying material from the corrosive environment) to an active state (i.e. the passive film has been destroyed and the underlying material is now affected by corrosion). The model described in (Walton et al. 1996) for iron and stainless steel exposed to different electrolyte solutions overcomes this limitation. Moreover, the study concludes that the electrochemical reactions at the metal/solution interface are the most important factors for the accurate prediction of the chemical environment within the pit or crevice. Another work worth of note is the study described in (Laycock et al. 1998), where FEM is used to create a model for the development of lace-like pit covers in stainless steel, which play a fundamental role in pit stability by helping in maintaining a concentrated local chemistry (Laycock & White 2001). An extension of this work to include the modelling of local chemistry, dissolution kinetics and pit propagation in austenitic stainless steels under potentiostatic control is described in (Laycock & White 2001) and the results concerning pit morphology and propagation are in good agreement with experimental data. This study concluded that dissolution occurs more slowly in diffusion-controlled regime than in activation-controlled regime (vid. Section 6.2 for an explanation of the difference between these two corrosion regimes). These last two models are both based on the approach described in (Isaacs 1973), where Fick's law is employed in combination with the Faraday's law, which is used to relate the corrosion current density to the mass of dissolved metal. However, as pointed out in (Scheiner & Hellmich 2007), this approach does not specifically account for the moving boundary problem

represented by the propagation of the pit cavity and, as argued in (Sharland 1987), this limitation affects negatively the reliability of the model. This shortcoming is overcome by the model presented in (Scheiner & Hellmich 2007), where Stefan conditions are used to describe the moving interface, and the size and shape of the pits are not prescribed, but naturally evolve by complying with the mass conservation law for a solid metal/solution system. The model predicts the time evolution of pit shape and electric current for the stainless steel 1D pencil electrode test and 2D foil electrode test in diffusion-controlled regime. This work was extended two years later (Scheiner & Hellmich 2009) to model both activation-controlled and diffusion-controlled pitting corrosion regimes. However, as argued in (Duddu 2014) and in (Onishi et al. 2012), the pit interface was not consistently tracked and, as a result, the pit boundaries had a non-realistic zigzag shape. Another study worth of note is described in (Xiao & Chaudhuri 2011), where the FEM is used to model pit propagation and repassivation around a cathodic intermetallic particle in aluminium alloys. However, as argued in (Duddu 2014), the modelling of pit propagation by using FEM is not an easy task since special procedures of moving mesh and remeshing are often needed. Moreover, as argued in (Vagbharathi & Gopalakrishnan 2014), if remeshing techniques are used, the finite element matrices have to be recalculated for every time step. In order to overcome these difficulties, an alternative numerical approach to the FEM can be the use of XFEM. For example, the studies reported in (Vagbharathi & Gopalakrishnan 2014) and (Duddu 2014) describe numerical models of corrosion pit propagation in stainless steel based on the XFEM framework and Fick's law of diffusion. An extension to the latter work is described in (Duddu et al. 2015), where the Fick's law of diffusion is replaced by the Nernst-Planck equation and crevice corrosion in Al-Mg alloy microstructures is investigated. In general, all the models discussed so far have been quite effective in predicting the corrosion rates reported in the experimental literature. However, according to (Chen & Bobaru 2015), due to the fact that the majority of corrosion deterministic models currently available only consider diffusion within the electrolyte solution, none of these models have been able to

predict corrosion subsurface damage, which is a phenomenon documented in the experimental literature (Song et al. 2014). With the aim of filling this gap, PD has been recently used to create a model of pitting corrosion (Chen & Bobaru 2015) based on a modified Nernst-Planck equation. This work was extended in (Chen et al. 2015), where the influence of the pit cover on the pit morphology was investigated. The work described in Chapter 6 is based on the PD model of pitting corrosion described in (Chen & Bobaru 2015). However, the approach used in the study here described is different and allows for a reduction of the computational cost, the prediction of realistic pit morphologies, the modelling of metal dissolution in the presence of a cluster of intermetallic particles and it serves as basis for the creation of the pit-to-crack transition model described in Chapter 7.

2.6 Numerical modelling of pit-to-crack transition

The experimental and numerical study described in (Suter et al. 2001) analyses the effect of tensile stress on the pitting behaviour of austenitic stainless steel in salt water. The authors found out that tensile stress can encourage the development of stable pits by reducing the value of pitting potential and promoting pit-to-crack transition. The simulations based on the finite difference scheme found pH values of around 2 within the cracks formed from the pits. The approach proposed in (Kondo 1989) for the prediction of fatigue crack initiation life based on pit growth is used in (Turnbull et al. 2006a) and in (Turnbull et al. 2006b), where pit-to-crack transition in steam turbine discs is investigated. As argued in (Turnbull et al. 2009), the Kondo's approach, which assumes cracks propagating from the pit base, may not be suitable for the description of pit-to-crack transition produced by non-cyclic loads, since recent X-ray tomographic images have shown that multiple SCC cracks can initiate and coalesce also in proximity of the pit mouth (Horner et al. 2011). The work reported in (Ståhle et al. 2007) employs the FEM with remeshing at each increment of time to investigate crack nucleation from pits. However, as mentioned by the authors, the crack length could not be calculated accurately and, due to numerical convergence issues, crack branching could not be captured. In the study

described in (Pidaparti & Rao 2008), a coupled experimental and computer-aided-design (CAD) procedure is used to generate 3D models representing the time evolution of corrosion pits in aluminium alloys. FEM is then used to predict the stress field around pits subjected to static tensile load and the sites of possible crack nucleation. A similar study is reported in (Pidaparti & Patel 2008), where the level of stresses increases and then reaches a plateau with increasing corrosion time. Another model based on FEM is described in (Turnbull et al. 2010), where a single pit in a cylindrical steel specimen subjected to tensile axial stress is analysed. The model predicts that, for low applied stress and assuming fully elastic material, the maximum stresses occur at the pit shoulder just below the pit mouth. More complex loading conditions were considered in (Rajabipour & Melchers 2013), where corroded pipes subjected to both internal pressure and axial load were considered. The study reported in (Zhu et al. 2013), where FEM was used to predict stress and strain fields around corrosion pits in austenitic stainless steel subjected to ultra-low elastic stress, confirmed that the highest stresses and strains occurred at the pit shoulder and that their magnitudes increases as the size of the pit increases. To the best of the author's knowledge, no PD model of pit-to-crack transition is currently available in the literature. Therefore, the PD model described in Chapter 7 is the first of its kind (De Meo & Oterkus 2016).

2.7 Summary

The historical overview and the advantages and limitations of the most popular numerical techniques used up to now to investigate the four problems considered in this thesis have been examined (i.e. fracture in polycrystalline materials, SCC damage, pitting corrosion damage and pit-to-crack transition). The use of the current numerical approach (i.e. PD) is justified in light of its superior capabilities concerning the modelling of materials failure and the treatment of discontinuous fields. Finally, the state of the art and the major findings of studies relevant to the problems considered here have been discussed and the current research has been put

into perspective. The following list summarises the findings that are of most relevance to this research:

- Macroscopic (e.g. fracture toughness) and microscopic (e.g. grain boundary strength) material properties have a significant effect on the fracture behaviour of materials.
- SCC and HE investigations require explicit modelling of the microstructure of the material.
- HE encourages crack propagation.
- Pitting corrosion modelling requires explicit solution of the moving boundary problem.
- The majority of deterministic pitting corrosion models currently available in the literature consider diffusion only within the electrolyte solution and, therefore, cannot predict subsurface damage.
- Corrosion pits give rise to higher local stresses that can lead to material fracturing (i.e. pit-to-crack transition).
- Experimental investigations show that pit-to-crack transition does not necessarily occur at the pit base; it often occurs at the pit shoulder and pit mouth.
- To the best of the author's knowledge, there is currently no study available in the literature concerning the PD modelling of fracture and crack growth in cubic polycrystals that also provides detailed investigation and description of the mathematical formulation.
- To the best of the author's knowledge, no PD framework is currently available for the modelling of SCC.

- To the best of the author's knowledge, no PD framework of pitting corrosion currently available in the literature can reproduce realistic pit morphologies or capture the effect of microstructural features such as intermetallic particles.

- To the best of author's knowledge, no PD numerical model is currently available for investigating crack propagation from corrosion pits.

3 Peridynamics

3.1 Introduction

The aim of this chapter is to introduce the reader to PD, which is the numerical technique used in this research study. At present, three different versions of PD exist: 1) bond-based PD (Silling 2000), 2) ordinary state-based PD (Silling et al. 2007) (Madenci & Oterkus 2014), and 3) non-ordinary state-based PD (Silling et al. 2007) (Warren et al. 2009). The main limitation of bond-based PD is that it is restricted to the analysis of materials with Poisson's ratio of 1/4 and 1/3 for 3D and 2D models, respectively. Ordinary state-based PD overcomes this limitation, but both formulations are restricted to central force interactions. In contrast, in non-ordinary state-based PD, the bonds are represented with strain and stress tensors, which allows the use of already existing constitutive models, and bond forces can be in any direction (Warren et al. 2009). In this study, bond-based PD is used for the following two reasons: 1) the simplicity of the formulation, and 2) the materials considered in this research are suitable to be modelled within the framework of bond-based PD. In this thesis, if not otherwise specified, the terms "peridynamics" and "PD" refer to the bond-based version of PD. This chapter is organised as follows: the reasons for the introduction of PD are given in Section 3.2. In Section 3.3, some basic information about PD theory and a comparison with CCM is provided. A description of the numerical solution method is given in Section 3.4, while a summary of the information contained in this chapter can be found in Section 3.5.

3.2 Purpose and applications of peridynamics

PD is a new mathematical theory of mechanics that was presented for the first time to the scientific community in (Silling 2000). PD is a generalisation of CCM, which was introduced by the French mathematician Cauchy more than two centuries ago. CCM disregards the true nature of matter, which is discrete and generally

inhomogeneous (e.g. atoms, voids, microstructural features, discontinuities, cracks), and assumes that any solid object is continuum, which means that it can always be subdivided into smaller volumes that have identical properties (i.e. the bulk material properties). In many cases, when the lengthscale of the problem is much greater than the atomic distances, this simplification leads to accurate results, which can be obtained by solving differential equations derived from fundamental conservation laws (e.g. energy, mass, momentum). Indeed, nowadays well-known and widely-used commercial software for stress analysis (e.g. ANSYS, ABAQUS) are based on CCM, whose governing equations are solved through FEM. A second limitation of CCM is related to the fact that it is a local theory, which means that whatever happens at a certain material point depends only on what happens to the material points that are in its closest neighbourhood, i.e. all internal forces are contact forces (Silling & Lehoucq 2010) and, therefore, long-range forces (e.g. van der Waals forces) are not accounted for (Fig. 1).

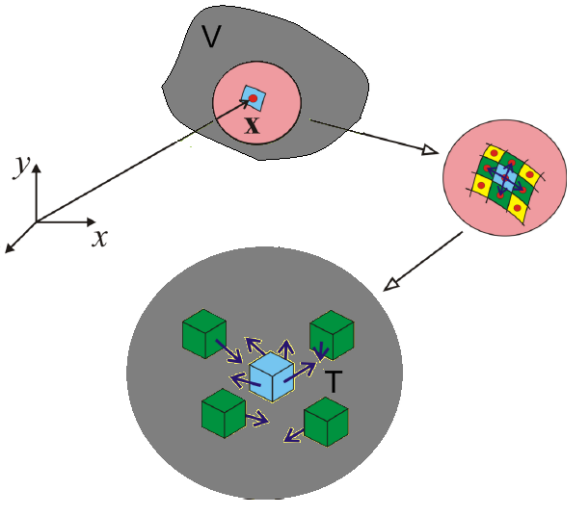

Fig. 1 CCM interactions in 2D

Finally, since the governing equations of CCM are based on partial differential equations (PDEs), its mathematical formulation breaks down in the presence of discontinuities such as cracks. Indeed, as argued in (Silling & Bobaru 2005), spatial derivatives do not exist on crack tips or surfaces. In other words, CCM assumes that

a body remains continuous as it deforms (Madenci & Oterkus 2014). As explained in (Silling & Lehoucq 2010), this limitation is partially overcome with the adoption of external crack growth criteria based on fracture mechanics. However, as mentioned in Section 2.2, this approach presents its own limitations and may not be suitable for the analysis of crack growth in nanoscale structures (Silling & Bobaru 2005). Nanotechnologies are becoming more and more popular nowadays and, due to the simplifications and assumptions on which CCM is based, in its current form, it is not suitable to analyse nanoscale structures and materials. Atomistic simulations (e.g. molecular dynamics) can overcome these limitations, but the required computational power necessary to investigate engineering timescales and lengthscales is still lacking (Silling & Lehoucq 2010). Therefore, in light of the limiting assumptions and difficulties of the current approaches, and with the aim to produce a comprehensive mathematical theory able to link macroscopic, mesoscopic and nanoscopic lengthscales in the same framework and more suitable for the analysis of materials failure and nanoscale structures, a new mathematical formulation of mechanics was developed in (Silling 2000), which was called "peridynamics". Concerning the research study described in this thesis, the benefits of using PD have been explained in Chapter 2.

PD is nowadays an active area of research and, thanks to the advantages of its mathematical formulation, several studies in diverse areas of physics have been published since its introduction. The major topics investigated up to now are: plastic materials, e.g. (Silling et al. 2007) and (Mitchell 2011), viscoelastic materials, e.g. (Kilic et al. 2009), viscoplastic materials, e.g. (Foster et al. 2011), impact, e.g. (Silling & Askari 2004), dynamic fracture, e.g. (Ha & Bobaru 2010) and (Ha & Bobaru 2011), buckling, e.g. (Kilic & Madenci 2009), extreme loadings on reinforced concrete structures, e.g. (Demmie & Silling 2007) and (Oterkus et al. 2012), composite materials, e.g. (Oterkus & Madenci 2012), heat transfer, e.g. (Kilic & Madenci 2010), electromigration, e.g. (Gerstle et al. 2008), nanofibers networks (Bobaru 2007), membranes, e.g. (Silling & Bobaru 2005), hygro-thermal diffusion (Oterkus et al. 2014), polycrystalline fracture, e.g. (De Meo, Zhu, et al. 2016),

corrosion, e.g. (Chen & Bobaru 2015) and (De Meo, Diyaroglu, et al. 2016). For a more comprehensive list, the reader is referred to (Madenci & Oterkus 2014).

3.3 Peridynamic theory

As mentioned in Section 3.2, the governing equations of CCM are PDEs and, therefore, they are not suitable to model discontinuities such as cracks. For example, the CCM equation of motion (EOM) of a generic material point $\mathbf{x}$ can be written as:

$$\rho(\mathbf{x})\ddot{\mathbf{u}}(\mathbf{x},t) = \nabla\cdot\sigma + \mathbf{b}(\mathbf{x},t) \tag{1}$$

where $\rho(\mathbf{x})$ and $\ddot{\mathbf{u}}(\mathbf{x},t)$ denote the density and acceleration of the material point $\mathbf{x}$ at time *t*, respectively. In Eq. (1), σ represents the stress tensor and the term $\mathbf{b}(\mathbf{x},t)$ is the body force acting on material point $\mathbf{x}$ at time *t*. Finally, $\nabla\cdot$ represents the divergence operator. Therefore, Eq. (1) requires time derivation and spatial derivation.

In contrast, the governing equations of PD are integro-differential. Indeed, the PD EOM of a generic material point $\mathbf{x}$ can be written as (Silling 2000)

$$\rho(\mathbf{x})\ddot{\mathbf{u}}(\mathbf{x},t) = \int_{H_{\mathbf{x}}} \mathbf{f}\left(\mathbf{u}(\mathbf{x}',t)-\mathbf{u}(\mathbf{x},t),\mathbf{x}'-\mathbf{x}\right) \mathrm{d}V_{\mathbf{x}'} + \mathbf{b}(\mathbf{x},t) \tag{2}$$

where $\mathbf{u}(\mathbf{x},t)$ denotes the displacement of the material point $\mathbf{x}$ at time *t* and $\mathbf{f}\left(\mathbf{u}(\mathbf{x}',t)-\mathbf{u}(\mathbf{x},t),\mathbf{x}'-\mathbf{x}\right)$ represents the PD force between material points $\mathbf{x}$ and $\mathbf{x}'$ (also called mechanical response function). $\mathrm{d}V_{\mathbf{x}'}$ is the volume associated with material point $\mathbf{x}'$. According to this new formulation, a material point can interact with other material points not only within its nearest neighbourhood, but also with material points in a larger neighbourhood (Fig. 2).

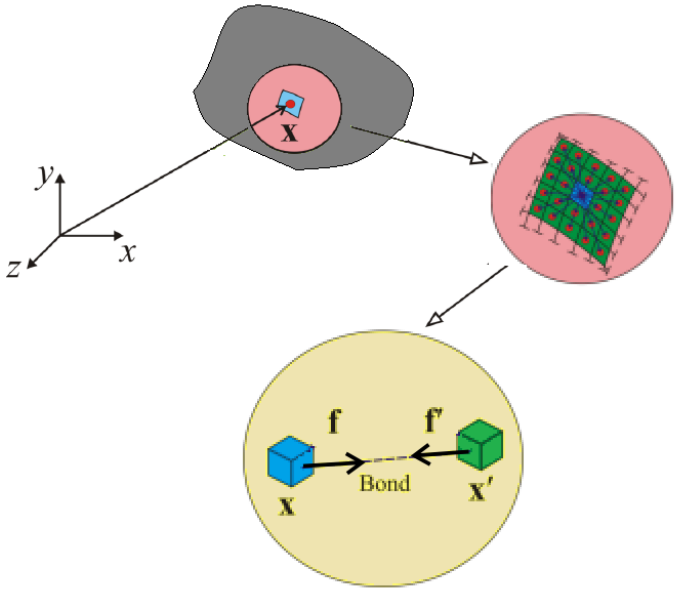

Fig. 2 PD interactions in 2D

Therefore, CCM is a local theory, while PD is a non-local theory. This difference makes PD suitable for the modelling of long-range forces (e.g. van der Waals forces), which become important as the lengthscale of the problem approaches the nanoscale (Silling & Bobaru 2005), (Bobaru 2007).

It is assumed that the interaction between material points decreases as the distance between them increases. Therefore, an influence domain, named horizon, H_x, is defined for each material point as shown in Fig. 3.

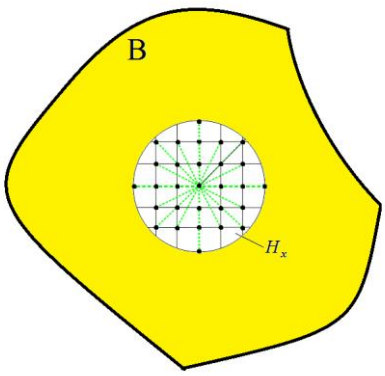

Fig. 3 PD horizon

Therefore, the material point $\mathbf{x}$ can only interact with material points within this domain, which are called the "family" of $\mathbf{x}$. This interaction is called "bond" and its length is simply the distance in space between the two material points. The radius of the horizon, δ, is chosen depending on the nature of the problem in such a way that the model is able to fairly represent the physical mechanisms of interest (Bobaru & Hu 2012). As δ decreases, the interactions become more local and, therefore, CCM can be considered as a special case of PD theory.

In the case of an elastic material, the peridynamic force between material points $\mathbf{x}$ and $\mathbf{x}'$, can be expressed as:

$$\mathbf{f} = c\, s \frac{\mathbf{y}' - \mathbf{y}}{|\mathbf{y}' - \mathbf{y}|} \tag{3}$$

where $\mathbf{y}$ represents the location of the material point $\mathbf{x}$ in the deformed configuration as shown in Fig. 4, i.e. $\mathbf{y} = \mathbf{x} + \mathbf{u}$, while c is the bond constant which can be related to material constants of CCM as described in (Madenci & Oterkus 2014).

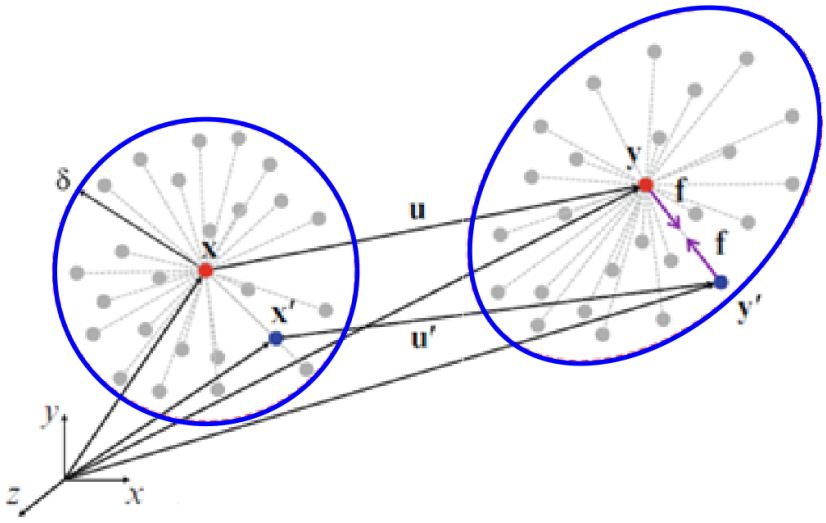

Fig. 4 PD undeformed configuration (left) and deformed configuration (right)

In Eq. (3), the stretch parameter s is defined as

$$s = \frac{|\mathbf{y}' - \mathbf{y}| - |\mathbf{x}' - \mathbf{x}|}{|\mathbf{x}' - \mathbf{x}|} \tag{4}$$

In the case of brittle material behaviour, the peridynamic force and the stretch relationship are shown in Fig. 5.

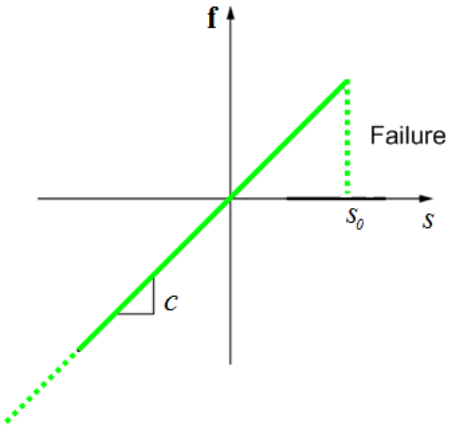

Fig. 5 PD bond behaviour for brittle materials

The parameter s_0, in Fig. 5, is called critical stretch and if the stretch of a peridynamic bond exceeds this critical value, the peridynamic interaction (bond) is broken. As a result, the peridynamic force between the two material points reduces to zero and the load is redistributed among the other bonds, leading to unguided material failure. PD predictions of autonomous crack propagation have been compared against results available from experimental investigations and, in many cases, a remarkable match was found (Madenci & Oterkus 2014), (Ha & Bobaru 2011), (Oterkus et al. 2012), (Ghajari et al. 2014). In PD theory, local damage is defined as the ratio between the number of failed bonds (i.e. those bonds whose stretch is greater than s_0) and the original number of bonds. The value of this index varies from 0 to 1, where a null value means no damage, while a unit value means that all the bonds have failed and, therefore, the particle is totally detached from the rest of the body. As shown qualitatively in Fig. 6, when the damage index reaches

the value 0.5, a new crack nucleates (the dashed red lines represent the failed bonds, while the solid green lines represent the intact bonds) (Madenci & Oterkus 2014).

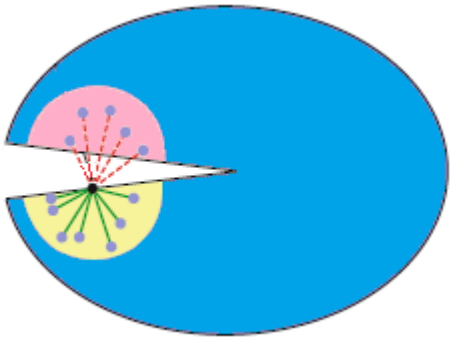

Fig. 6 PD definition of a crack

3.4 Numerical solution method

As already mentioned in Section 3.3, the PD EOM is integro-differential and, in general, it cannot be solved analytically, which means that only an approximated solution can be found. Therefore, numerical techniques for time and spatial integration are usually needed to solve the PD governing equations.

Concerning spatial integration, a meshless scheme and the collocation method can be used, which means that the domain is divided in smaller parts (Fig. 7), where each part has an associated volume and integration material point, which is also called collocation point. In case of a uniform grid, the distance among the material points is the same in all directions, and is usually indicated as Δ (Fig. 8).

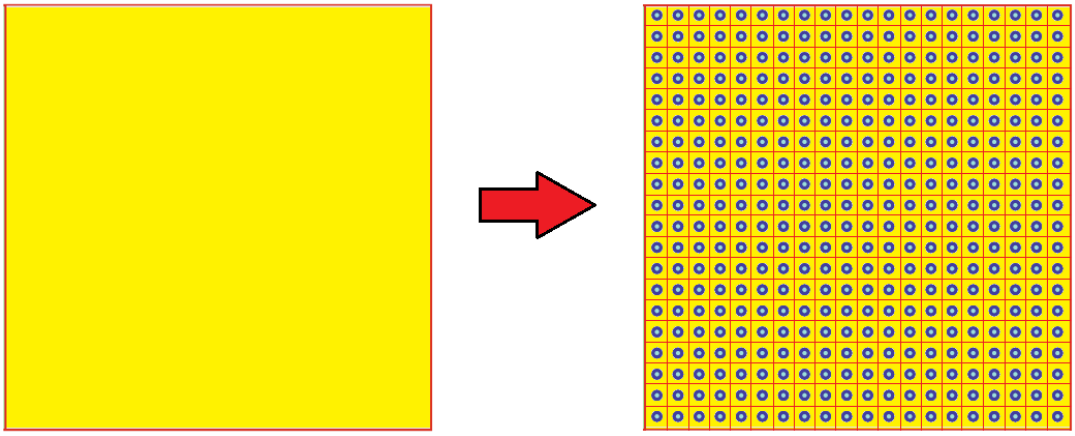

Fig. 7 PD domain discretisation in 2D

As mentioned in Section 3.3, for a generic material point $\mathbf{x}$, the spatial integration is performed only over the part of the body that is contained within the horizon of particle $\mathbf{x}$. Therefore, for a generic PD particle $\mathbf{x}_i$, the discretised form of Eq. (2) can be written as

$$\rho(\mathbf{x}_i)\ddot{\mathbf{u}}(\mathbf{x}_i,t)=\sum_{j}^{M}\mathbf{f}\left(\mathbf{u}(\mathbf{x}_j,t)-\mathbf{u}(\mathbf{x}_i,t),\mathbf{x}_j-\mathbf{x}_i\right)V_j+\mathbf{b}(\mathbf{x}_i,t) \tag{5}$$

where M is the number of family members of particle $\mathbf{x}_i$ (i.e. the pink volumes in Fig. 8). However, as shown in Fig. 8, not all considered volumes are fully embedded within the horizon. Indeed, some of them are truncated and, therefore, need correction, which is performed by multiplying V_j by a term, v_c, called "volume correction factor", which is calculated as explained in (Madenci & Oterkus 2014). Basically, $v_c=1$ for all bonds whose length is smaller or equal to (δ-r) and $v_c=0.5$ when the bond length is equal to δ. For all other bonds, the value of v_c changes linearly between these two values as a function of the bond length.

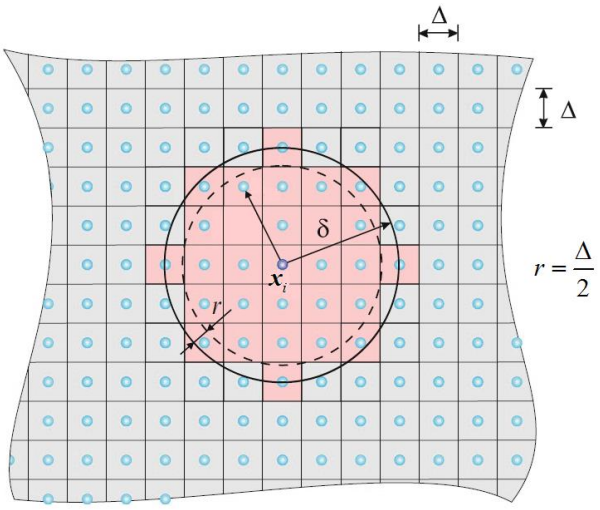

Fig. 8 Meaning of the volume correction factor

The discretised PD EOM with volume correction can be written as

$$\rho(\mathbf{x}_i)\ddot{\mathbf{u}}(\mathbf{x}_i,t) = \sum_j^M \mathbf{f}\left(\mathbf{u}(\mathbf{x}_j,t) - \mathbf{u}(\mathbf{x}_i,t), \mathbf{x}_j - \mathbf{x}_i\right)(V_j\, v_{c_j}) + \mathbf{b}(\mathbf{x}_i,t) \tag{6}$$

As argued in (Madenci & Oterkus 2014), solution inaccuracies can arise due to the fact that material points in proximity of free surfaces have fewer bonds than other material points. Therefore, the PD force **f** is multiplied by a term called "surface correction factor", s_{cf}, which can be calculated as described in (Madenci & Oterkus 2014). The PD EOM with volume correction and surface correction can be written as

$$\rho(\mathbf{x}_i)\ddot{\mathbf{u}}(\mathbf{x}_i,t) = \sum_j^M \mathbf{f}\left(\mathbf{u}(\mathbf{x}_j,t) - \mathbf{u}(\mathbf{x}_i,t), \mathbf{x}_j - \mathbf{x}_i\right)(V_j\, v_{c_j}\, s_{cf_{ij}}) + \mathbf{b}(\mathbf{x}_i,t) \tag{7}$$

Initial cracks can be defined by the removal of all those PD bonds which cross the crack surfaces as shown in Fig. 9.

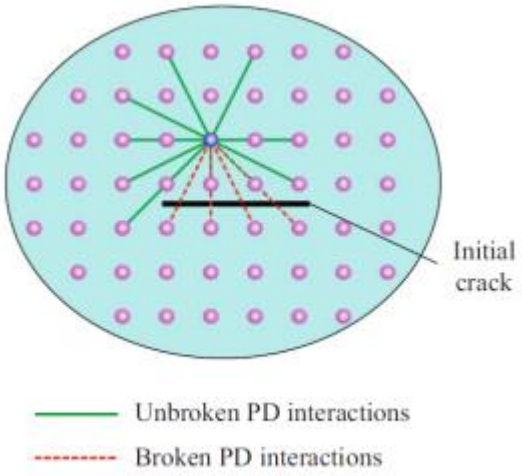

Fig. 9 PD definition of initial crack

Concerning the time integration, initial displacement and velocity have to be defined before the beginning of the integration, which can be carried out via an explicit central difference scheme as described in (Silling & Askari 2005). Thus, for the generic particle $\mathbf{x}_i$, the acceleration at the current time step "n_t", i.e. ($\ddot{\mathbf{u}}_i^{n_t}$), is calculated by using Eq. 7. Then, the velocity and displacement of $\mathbf{x}_i$ at the next time step (i.e. n_t+1), $\dot{\mathbf{u}}_i^{n_t+1}$ and $\mathbf{u}_i^{n_t+1}$, can be predicted by using Eq. 8 and Eq. 9, respectively (Madenci & Oterkus 2014).

$$\dot{\mathbf{u}}_i^{n_t+1} = \dot{\mathbf{u}}_i^{n_t} + \ddot{\mathbf{u}}_i^{n_t} \cdot \Delta t \tag{8}$$

$$\mathbf{u}_i^{n_t+1} = \mathbf{u}_i^{n_t} + \dot{\mathbf{u}}_i^{n_t} \cdot \Delta t \tag{9}$$

In the case of explicit time integration, the numerical solution is stable only if the time step size '*dt*' is sufficiently small. In particular, as shown in (Silling & Askari 2005), the limit on the time step size can be calculated on the basis of a von Neumann stability analysis as shown in Eq. (10).

$$dt < \sqrt{\frac{2\rho\Delta}{\pi\delta^2\Delta c}} \tag{10}$$

PD governing equations can also be solved via implicit time integration, which is the approach used for the simulations in Chapter 5 (SCC modelling), Chapter 6 (pitting corrosion modelling), and Chapter 7 (pit-to-crack transition modelling). More precisely, in order to take advantage of its accuracy, stability and efficiency, the implicit Newmark time integration solver and the Newton-Raphson iterative algorithm implemented in the FEM software ANSYS 14.5 were used. According to the Newmark family of time integration schemes, the nodal velocity and displacement at the next time step can be written as

$$\dot{\mathbf{u}}_i^{n_t+1} = \dot{\mathbf{u}}_i^{n_t} + \left[(1-\tau) \cdot \ddot{\mathbf{u}}_i^{n_t} + \tau \cdot \ddot{\mathbf{u}}_i^{n_t+1} \right] \cdot \Delta t \tag{11}$$

$$\mathbf{u}_i^{n_t+1} = \mathbf{u}_i^{n_t} + \dot{\mathbf{u}}_i^{n_t} \cdot \Delta t + \left[\left(\frac{1}{2} - a \right) \cdot \ddot{\mathbf{u}}_i^{n_t} + a \cdot \ddot{\mathbf{u}}_i^{n_t+1} \right] \cdot \Delta t^2 \tag{12}$$

where a and τ are the Newmark's integration parameters, which have to satisfy the following two conditions for the method to be unconditionally stable:

$$\tau \geq \frac{1}{2} \tag{13}$$

$$a \geq \frac{1}{4} \cdot \left(\frac{1}{2} + \tau \right)^2 \tag{14}$$

Further details about this method can be found in (ANSYS, Mechanical User's Guide).

3.5 Summary

The bond-based version of PD theory is used in this research study for the simplicity of its formulation and its suitability to model the materials here considered. Thanks to the non-local and integro-differential nature of its mathematical formulation, PD

is particularly suitable to model materials failure at any lengthscale and is currently used to investigate and solve problems in several areas of physics and engineering. The concepts of horizon and critical stretch are an integral part of PD theory. In many cases, no analytical solution is available for the PD EOM. Therefore, numerical techniques are used to find approximate results. In this regard, meshless methods are popular for the discretisation of PD governing equations and volume and surface correction factors are often used to improve the accuracy of the solution.

4 Fracture of polycrystalline materials

4.1 Introduction

The aim of this chapter is to describe a novel PD formulation developed for predicting the mechanical response and fracture behaviour of cubic polycrystalline materials. The results obtained from static and dynamic PD analyses are presented, and comparisons with FEM results are also provided. Concerning the static analyses, firstly, a single cubic crystal is considered and the PD and FEM displacement fields are compared (Section 4.5.1). Secondly, a cubic polycrystal constituted of 100 grains is analysed and, again, the PD and FEM displacement fields are compared (Section 4.5.2). Concerning the dynamic analyses, firstly, the influence of the horizon and peridynamic discretisation on results is evaluated (Section 4.5.3.1). Secondly, the effect of the grain size and grain orientation on the time-to-failure and fracture behaviour is investigated (Section 4.5.3.2). Thirdly, the impact of the grain boundary strength on the crack speed is examined (Section 4.5.3.3). Fourthly, a comparison of fracture morphology is provided for different values of material fracture toughness K_{IC} (Section 4.5.3.4) and for plane stress/strain conditions (Section 4.5.3.5). Finally, Section 4.6 highlights the gaps and limitations of this study, while Section 4.7 provides a summary of the major information contained in this chapter. The study here described can be found in (De Meo, Zhu, et al. 2016) and, to the best of the authors' knowledge, this is the first time that a PD material model of cubic polycrystals is given and explored in detail. As previously mentioned, corrosion behaviour is influenced not only by environmental variables, but also by the microstructural characteristics and properties of the material. Therefore, the PD framework presented in this chapter, which is used as foundation for the corrosion models that are described in the next chapters, is important because it allows the direct modelling of the microstructure of the material and its fracture behaviour.

4.2 Background and motivation

Polycrystalline materials, such as common metals, rocks and many ceramics, are solids constituted by crystals (or grains) that can have different shape, size and random orientation, and interact with one another through their grain boundaries. As argued in (Benedetti & Aliabadi 2013), polycrystalline materials are among the most common materials used in practical engineering applications. Hence, in order to build safe structures without relying on excessive overdesign, it is necessary to fully understand the fracture behaviour of these materials. However, owing to the fact that the fracturing of polycrystalline materials is often influenced by the characteristics of its microstructure (e.g. grain size, differences in physical properties between grain and its boundaries, crystallographic orientation and the presence of flaws of different size, shape and orientation), the task is often challenging.

Several experimental approaches are available to study the fracture behaviour of this class of materials (Herbig et al. 2011), (Ludwig et al. 2009), (Groeber et al. 2006). Unfortunately, despite the resulting valuable information provided by experimental approaches, these techniques are not always viable due to the necessity of expensive equipment and complex and time consuming procedures for material preparation and analysis (Benedetti & Aliabadi 2013). Therefore, computational approaches represent a precious complement for understanding the fracturing of polycrystalline materials. However, as argued in (Sfantos & Aliabadi 2007b), despite the valuable results obtained by the latest numerical studies, the mathematical modelling of the transition from microscopic defects to macroscopic cracks is not entirely understood at present and, as a result, the current design codes and standards prescribe the use of safety factors to compensate this lack of understanding and predicting capability (Crocker et al. 2005). The literature review undertaken for this study can be found in Section 2.3.

4.3 Peridynamic model of cubic polycrystals

In this study, a microscopic material model is used to represent the behaviour of a cubic polycrystalline structure with random texture. For this purpose, a new PD material model is developed to express the deformation response of each crystal. The polycrystalline structure is generated by using the Voronoi tessellation method (Fig. 10). The procedure, implemented by using Fortran, is constituted of the following steps:

1. Generation of pseudo-random seeds within the domain. The number of seeds has to be equal to the number of crystals that the user wants to have within the domain. This is achieved by generating pseudo-random x and y coordinates for each seed from a uniform distribution between 0 and 1.

2. A number and a colour is assigned to each seed.

3. The first PD particle is considered and its distance from all the seed is calculated.

4. The closest seed to the PD particle under consideration is selected.

5. The number and colour of this seed is then associated to the PD particle under consideration.

6. Points 3-5 are repeated for all PD particles.

At the end of the procedure, each PD particle will be associated to a particular colour as shown in Fig. 10 (b). The main steps of the procedure are given in Fig. 10 (a).

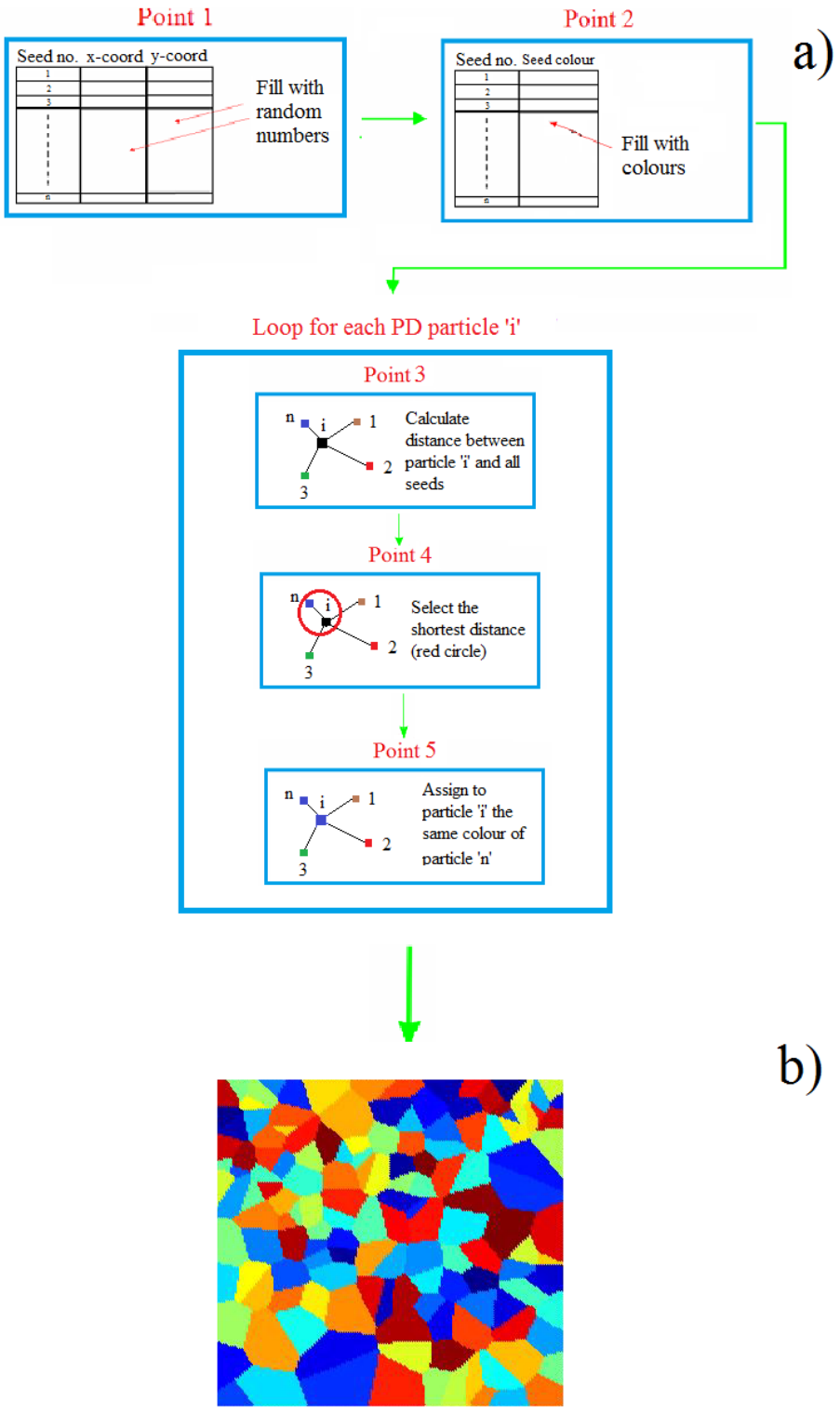

Fig. 10 Flowchart for the generation of the Voronoi polycrystal (a), final Voronoi polycrystal visualised with MATLAB (b)

The micro-mechanical PD model of cubic polycrystals is constituted of the following two types of PD bonds (Fig. 11):

- Type-1 bonds (dashed green lines) – exists in all directions (i.e. $\theta = 0 - 2\pi$)
- Type-2 bonds (solid red lines) – exists only for the following directions:

$$\theta = \frac{\pi}{4}, \frac{3}{4}\pi, \frac{5}{4}\pi, \frac{7}{4}\pi$$

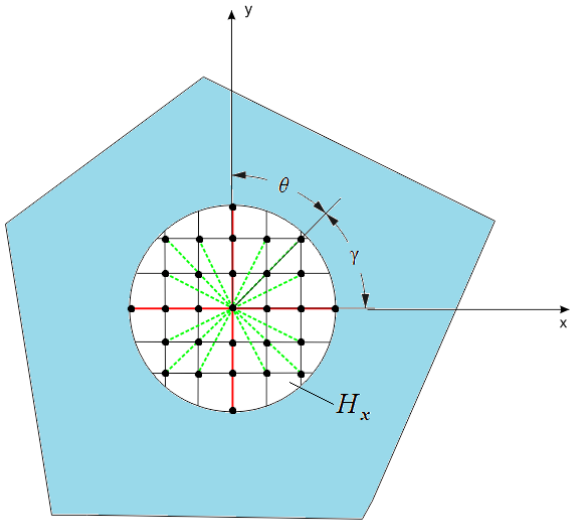

Fig. 11 Type-1 (dashed green lines) and type-2 (solid red lines) bonds for the PD micro mechanical model

Note that the angle θ is defined with respect to the orientation of the crystal. In the special case shown in Fig. 11, the crystal orientation γ equals π/4 and it is always measured with respect to the x-axis, while, in general, an algorithm is used to assign a random orientation γ to the grain. As a result of this procedure, when a polycrystalline system of random texture is represented by this model, type-2 bonds will exist in many different directions according to the random orientations of the crystals.

The bond constants for type-1 and type-2 PD bonds can be expressed in terms of the material constants of a cubic crystal, C_{ij} (vid. Section 4.4), by following a procedure similar to that explained in (Madenci & Oterkus 2014). In the case of plane stress condition, the bond constants can be expressed as

$$c_{T1} = \frac{12(c_{11}^2 - c_{11}c_{12})}{\pi h \delta^3 c_{11}} \qquad c_{T2} = \frac{4(3c_{11}c_{12} - 2c_{12}{}^2 - c_{11}^2)}{(\beta_A + \beta_B)c_{11}} \tag{15}$$

where h is the thickness of the structure. The quantities β_A and β_B can be expressed as

$$\beta_A = \sum_{j=1}^{q_A} \xi_{ij} V_j \qquad \beta_B = \sum_{j=1}^{q_B} \xi_{ij} V_j \tag{16}$$

where subscript A is associated with directions $\theta = \frac{\pi}{4}, \frac{5}{4}\pi$, whilst subscript B is associated with directions $\theta = \frac{3}{4}\pi, \frac{7}{4}\pi$.

In Eq. (16), i and j refer to a generic particle and its neighbour, respectively, V_j denotes the volume of particle j, ξ_{ij} is the initial length of the bond between particles i and j, and q_A and q_B represent the number of PD bonds along the directions associated with A and B, respectively. Similarly, in the case of plane strain condition, the bond constants can be expressed as

$$c_{T1} = \frac{12(c_{11} - c_{12})}{\pi h \delta^3} \qquad c_{T2} = \frac{4(3c_{12} - c_{11})}{(\beta_A + \beta_B)} \tag{17}$$

The detailed derivation of type-1 and type-2 PD bond constants for both plane stress and plane strain configuration is given in Appendix A. The model was fully validated by using the FEM's deformation field as a reference and a good agreement between the two approaches was observed as shown in Section 4.5 and 4.6. The

critical stretch parameter for PD bonds was obtained based on the expression given in (Madenci & Oterkus 2014):

$$s_0 = \sqrt{\frac{4\pi G_c}{9E\delta}} \tag{18}$$

where E is the Young's modulus. In case of linear elastic material, the critical energy release rate G_c can be obtained from the fracture toughness, K_{Ic}, for plane stress and plane strain configurations, respectively, as follows [17]:

$$G_c = \frac{K_{Ic}^2}{E} \tag{19}$$

$$G_c = \frac{K_{Ic}^2}{E}\left(1-\nu^2\right) \tag{20}$$

where ν is the Poisson's coefficient. In order to investigate various fracture modes typical of polycrystalline materials, a grain boundary coefficient (GBC) is defined as follows:

$$GBC = \frac{s_{0\,GB}}{s_{0\,GI}} \tag{21}$$

where $s_{0\,GB}$ and $s_{0\,GI}$ represent the critical stretch of the PD bonds that cross the grain boundaries of the material and the critical stretch of the PD bonds that are fully included within the grains, respectively (GB stands for grain boundary, while GI stands for grain interior).

4.4 Materials data

Two materials are employed in the study presented in this chapter. Iron crystals are considered for static analyses (Section 4.5 and Section 4.6), while AISI 4340 steel is

considered for dynamic analyses (Section 5.7). The chemical composition of AISI 4340 steel is summarised in Table 1 (Hirose & Mura 1984b):

Table 1 AISI 4340 steel chemical composition

C	Si	Mn	P	S	Cu	Mo	Ni	Cr
0.39%	0.27%	0.77%	0.018%	0.016%	0.14%	0.23%	1.38%	0.78%

The fracture toughness of AISI 4340 steel is considered to be $K_{Ic} = 58.4\,\mathrm{MPa}\sqrt{\mathrm{m}}$ (Rimoli & Ortiz 2010). The crystals are assumed to have α-ferrite structure with body-centered cubic (BCC) lattice. As described in (Hosford 1993), the local stiffness matrix of each individual crystal can be written as

$$[C] = \begin{bmatrix} c_{11} & c_{12} & c_{12} & 0 & 0 & 0 \\ c_{12} & c_{11} & c_{12} & 0 & 0 & 0 \\ c_{12} & c_{12} & c_{11} & 0 & 0 & 0 \\ 0 & 0 & 0 & c_{44} & 0 & 0 \\ 0 & 0 & 0 & 0 & c_{44} & 0 \\ 0 & 0 & 0 & 0 & 0 & c_{44} \end{bmatrix} \tag{22}$$

To be noted that, if the microstructure of the material at room temperature is not α-ferrite, the stiffness matrix given in Eq. (22) may not be appropriate. For example, in the case of AISI 4340 with martensitic structure at room temperature, the crystal system to be considered should be tetragonal and not cubic. The 3D stiffness matrix for tetragonal crystals is different with respect to that given in Eq. (22). However, in the case of 2D plane strain simplification, the two matrices coincide. Therefore, under certain conditions, the PD model for cubic polycrystals described in Section 4.3, can be used also for the modelling of tetragonal systems like martensite.

In order to take into account the polycrystalline nature of the material, the values of the elastic moduli C_{ij} are found by applying an axial tension to a microscopic AISI 4340 steel specimen and then fitting experimental and numerical results as described in (Rimoli 2009). The resulting microscopic material properties are:

$$c_{11} = 208.9 \quad \text{GPa} \qquad c_{12} = 126.4 \quad \text{GPa} \qquad c_{44} = 97.7 \quad \text{GPa} \tag{23}$$

Concerning iron crystal, the considered microscopic material properties are (Hosford 1993):

$$c_{11} = 231.4 \quad \text{GPa} \qquad c_{12} = 134.7 \quad \text{GPa} \qquad c_{44} = 116.4 \quad \text{GPa} \tag{24}$$

4.5 Numerical results and validation

4.5.1 Static analysis of iron crystals

The cubic crystals considered in this study have a length of 15.24 μm and a width of 7.62 μm (Fig. 12). The number of particles along the horizontal and vertical directions is 240 and 120, respectively. The left edge of the crystal is fully fixed, while the right edge is subjected to a horizontal loading P = 156 MPa.

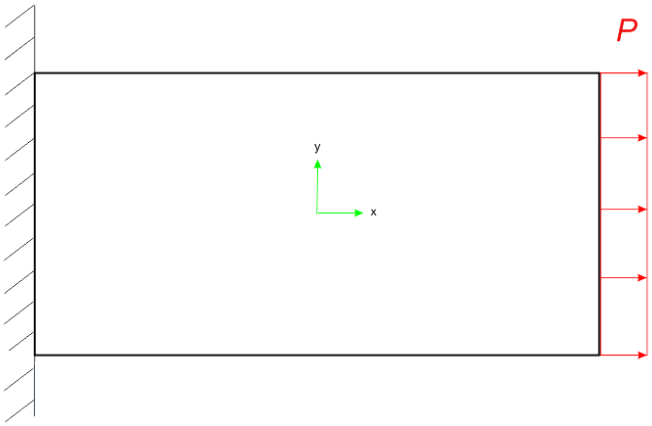

Fig. 12 Iron crystals for static analysis

Three layers of virtual particles are placed along the right edge of the plate to impose the tension loading boundary condition. Three additional layers of virtual particles are also placed along the left edge of the plate with the aim to constrain the model. The values of grid spacing and horizon radius are $\Delta = 6.35 \cdot 10^{-2}$ μm and

$\delta = 19.14 \cdot 10^{-2}$ μm, respectively. Therefore, $\delta/\Delta \approx 3$, which explains why there are three layers of virtual particles.

Similarly, the FEM model implemented in ANSYS is constituted of 240 and 120 plane 182 elements along the x and y direction, respectively. The elastic moduli C_{ij} have been set through the command 'TBDATA', while the grain orientation has been assigned by defining a local coordinate system with respect to the active coordinate system through the command 'CLOCAL'.

Fig. 13 and Fig. 14 show the comparison between the results obtained with FEM and PD concerning the displacement field of the cubic crystal in plane stress configuration with orientation 0° (i.e. the orientation of the crystal coincides with the x-direction) and orientation 45°, respectively.

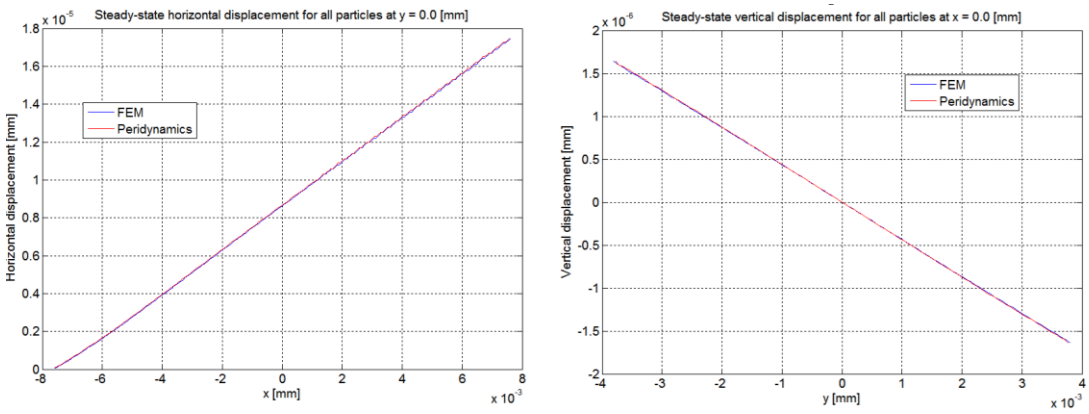

Fig. 13 Displacement field comparison between FEM and PD for the iron crystal in plane stress configuration and 0° orientation

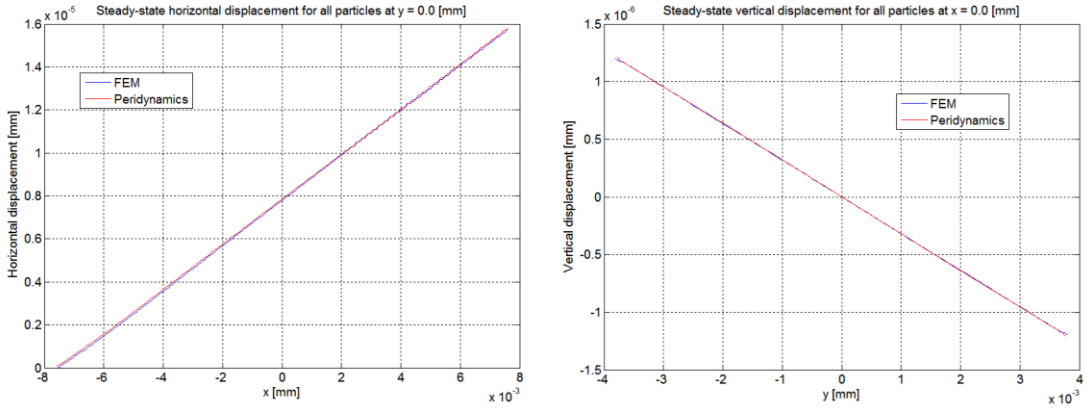

Fig. 14 Displacement field comparison between FEM and PD for the iron crystal in plane stress configuration and 45° orientation

Fig. 15 and Fig. 16 show the comparison between the results obtained with FEM and PD concerning the displacement field of the cubic crystal in plane strain configuration with orientation 0° (i.e. the orientation of the crystal coincides with the x-direction) and orientation 45°, respectively.

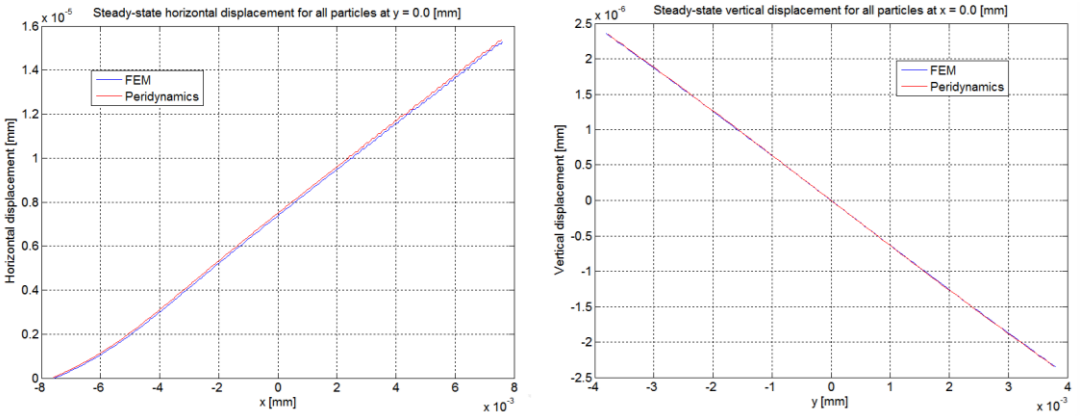

Fig. 15 Displacement field comparison between FEM and PD for the iron crystal in plane strain configuration and 0° orientation

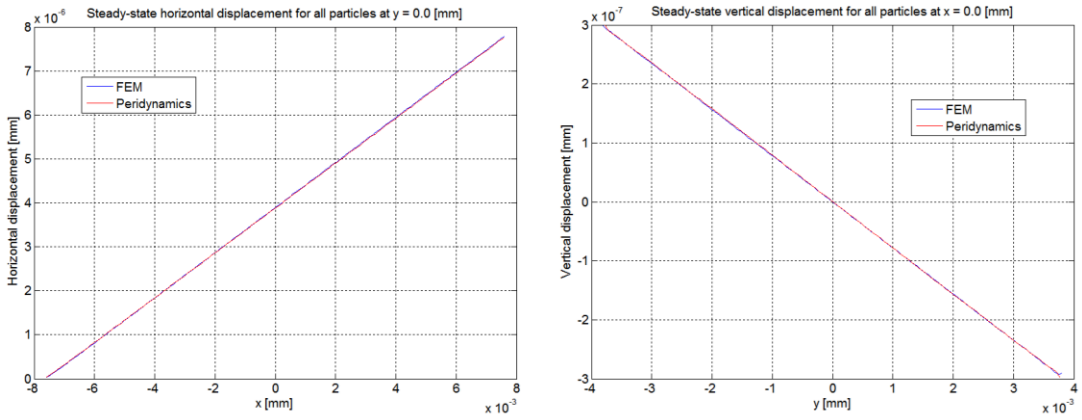

Fig. 16 Displacement field comparison between FEM and PD for the iron crystal in plane strain configuration and 45° orientation

The same simulations have been carried out also considering a vertical load instead of a horizontal one; in all cases, a good agreement was found between FEM and PD results. Therefore, it is possible to conclude that the micro-mechanical PD model of cubic crystals here presented agrees well with the FEM for plane stress configuration, for plane strain configuration, for different grain orientations and for different static loading conditions.

4.5.2 Static analysis of iron polycrystals

The cubic polycrystals considered in this section are constituted of 100 randomly oriented grains and have a length of 5 mm and a width of 2.5 mm (Fig. 17). Similar to the previous analysis (Section 4.5.1), the number of particles along the horizontal and vertical direction is 240 and 120, respectively. The left edge of the polycrystal is fully fixed while the right edge is subjected to a horizontal loading P = 150 MPa. Three layers of virtual particles are placed along the right edge of the plate to impose the tension loading boundary condition. Three additional layers of virtual particles are also placed along the left edge of the plate with the aim to constrain the model. The values of grid spacing and horizon radius are $\Delta = 2.083 \cdot 10^{-5}$ m and $\delta = 6.281 \cdot 10^{-5}$ m, respectively.

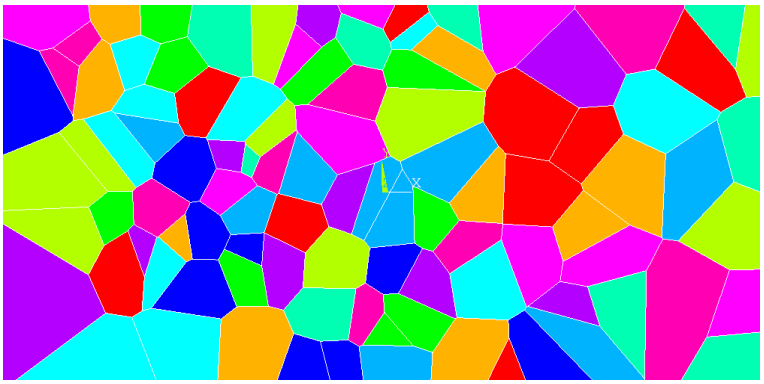

Fig. 17 Iron polycrystals considered for static analysis

As shown in Fig. 18 and Fig.19, a good agreement between FEM (implemented in ANSYS) and PD was found concerning the final displacement field of the cubic polycrystal in plane stress (Fig.18) and plane strain configurations (Fig.19).

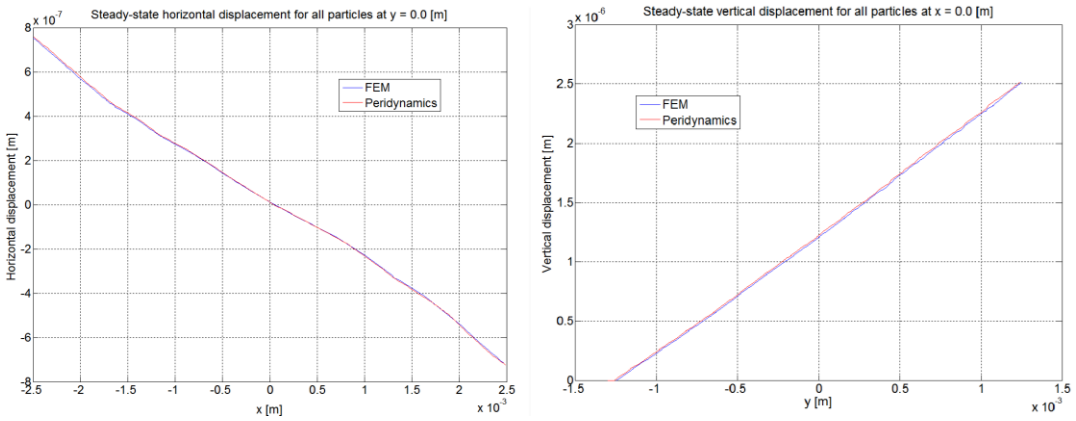

Fig. 18 Displacement field comparison between FEM and PD for the iron polycrystal in plane stress configuration

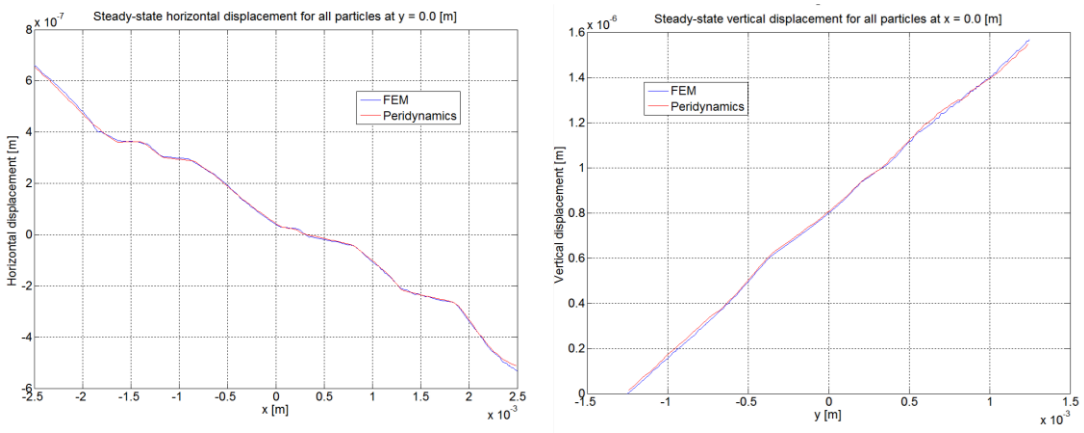

Fig. 19 Displacement field comparison between FEM and PD for the iron polycrystal in plane strain configuration

4.5.3 Dynamic analysis of AISI 4340 polycrystals

4.5.3.1 Selection of the horizon size

The aim of this analysis is to investigate the effect of the horizon size and peridynamic discretisation on the fracture pattern predicted by our PD model. For this purpose, an AISI 4340 polycrystal in plane strain condition with dimensions of 5 mm by 5 mm is considered as shown in Fig. 20. Both left and right edges of the polycrystal are subjected to a horizontal velocity boundary condition V = 25 m/s. Three layers of virtual particles are placed along the left and right edges of the plate to impose the velocity boundary condition. Moreover, in order to ensure that the external load is properly transferred to the internal part of the plate, a no-fail zone is imposed on the virtual particles and their neighbours. The length of the two initial cracks at the bottom and top edges of the polycrystal is 0.4 mm (vid. Fig. 20). An explicit central difference scheme is used for the time integration with a time step size $dt = 2$ ns. The total simulation time is 2.4 μs corresponding to 1200 time steps. This study considers three different GBC values (0.5, 1.0 and 2.0), three different values of average grain size (333 μm, 416 μm and 714 μm) and five different values of horizon size δ (202.7 μm, 100 μm, 50 μm, 37.5 μm and 30 μm) for a total of 45 simulations (vid. Figs. 21-23). The horizon size is calculated as $\delta = 3.015 \cdot \Delta$.

Therefore, its value is controlled indirectly by changing the PD discretization, i.e. 74 x 74 particles, 150 x 150 particles, 300 x 300 particles, 400 x 400 particles and 500 x 500 particles, respectively.

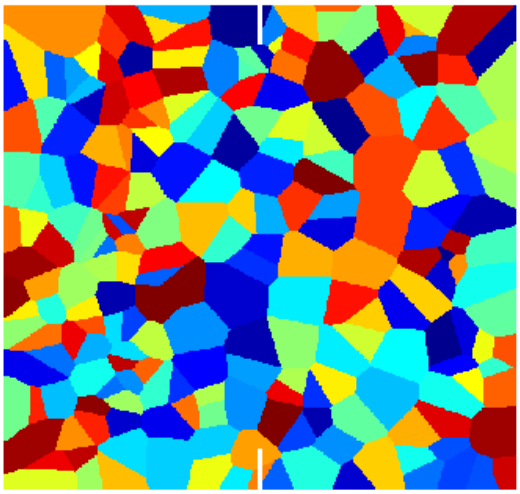

Fig. 20 AISI 4340 polycrystal for convergence analysis

As depicted in Fig. 21, for the polycrystal with average grain size of 333 μm, a horizon size of 202.7 μm (top red square with arrow) is sufficient to reproduce the main features of the fracture pattern. Indeed, in all five simulations, the major cracks propagate from the initial notch and the fragmentation of the central part of the plate is similar despite the poor resolution of the results obtained with higher horizon sizes and lower number of particles. In other words, the horizon size and the PD discretisation affect the resolution of the results, but not the overall fracture pattern. This is not true for higher values of average grain size. Indeed, as shown in Fig. 21, for the simulations with average grain size of 416 μm and 714 μm, the convergent horizon values are 100 μm (middle red square with arrow) and 50 μm (bottom red square with arrow), respectively. This can be explained by noting that, if the dimensions of the plate are kept constant as in this case, the smaller the grain size the higher the possibility that a grain boundary exists in proximity of the initial crack tip. If the grain boundary is weak with respect to the bulk of the crystal (like in this case since GBC = 0.5), the initial notch is further encouraged to propagate and form a major crack despite the coarse mesh.

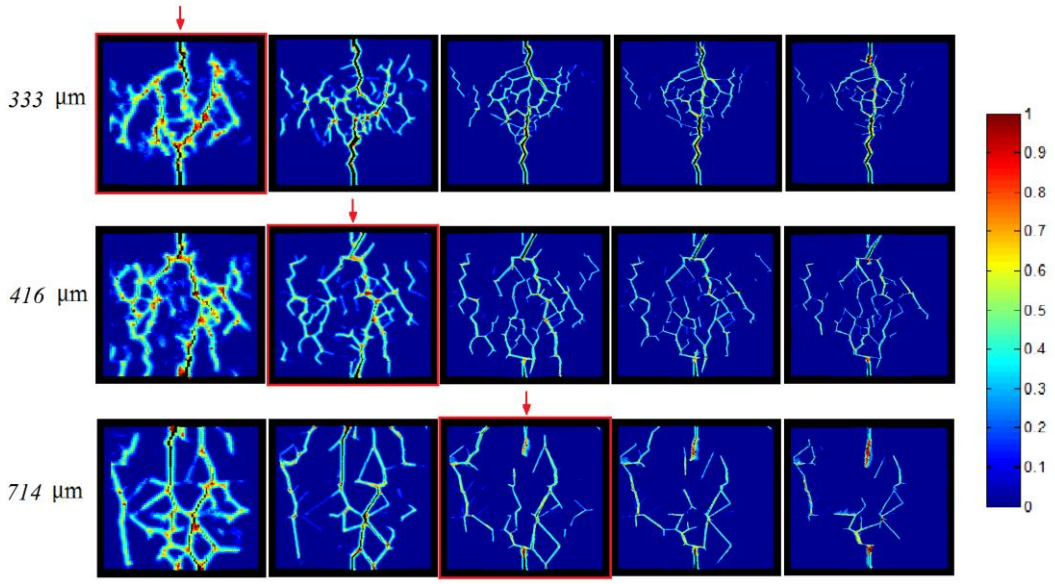

Fig. 21 GBC = 0.5, time = 2.4 µs. Fracture pattern comparison of three polycrystals with different average grain size (333 µm, 416 µm and 714 µm) and five different horizon values: from left to right, 202.7 µm (74 x 74 particles), 100 µm (150 x 150 particles), 50 µm (300 x300 particles), 37.5 µm (400 x 400 particles) and 30 µm (500 x 500 particles)

The simulations that considered higher horizon values and lower number of particles than the convergent ones failed to capture the right location of the major cracks. Therefore, when GBC = 0.5, the value of the convergent horizon size is dependent on the grain size. As it can be seen in Figs. 22-23, this is not true for GBC = 1.0 and GBC = 2.0. Indeed, in these cases, the grain boundaries do not play the part of weak points anymore and, as a result, in both cases, the grain size does not influence the value of the convergent horizon (red squares with arrow), which can be considered to be 50 µm (300 x 300 particles) for all values of grain size considered. Moreover, the fracture patterns in Figs. 22-23 are very similar and the failure mode is transgranular. This is in contrast with the results for GBC = 0.5 (Fig. 21), where the fracture patterns are different with respect to Figs. 22-23 and the failure mode is intergranular. A more detailed analysis of the effect of GBC is provided in Section 4.7.3 and Section 4.7.4.

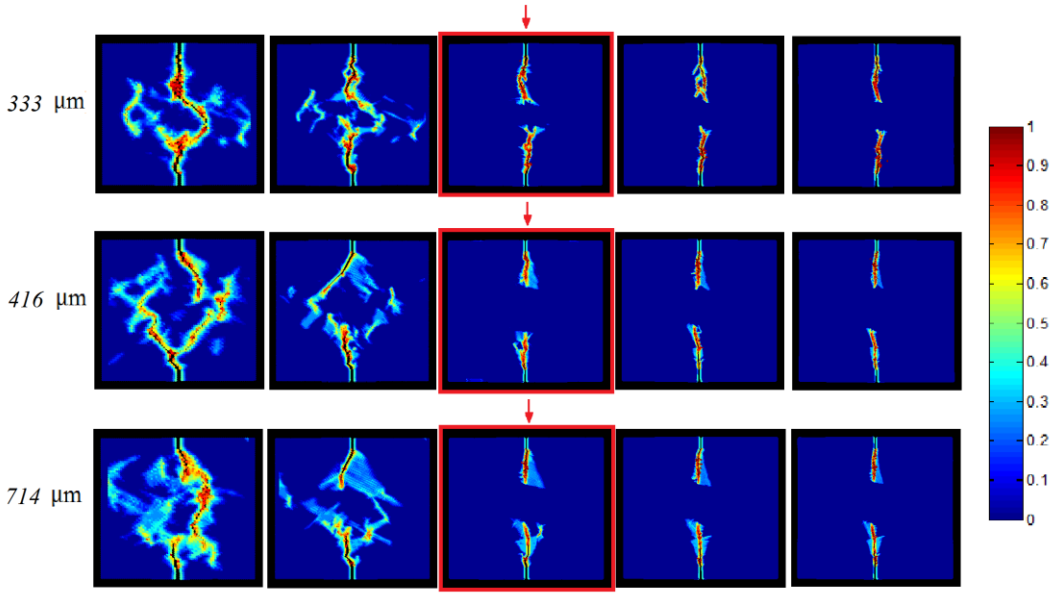

Fig. 22 GBC = 1, time = 2.4 µs. Fracture pattern comparison of three polycrystals with different average grain size (333 µm, 416 µm and 714 µm) and five different horizon values: from left to right, 202.7 µm (74 x 74 particles), 100 µm (150 x 150 particles), 50 µm (300 x 300 particles), 37.5 µm (400 x 400 particles) and 30 µm (500 x 500 particles)

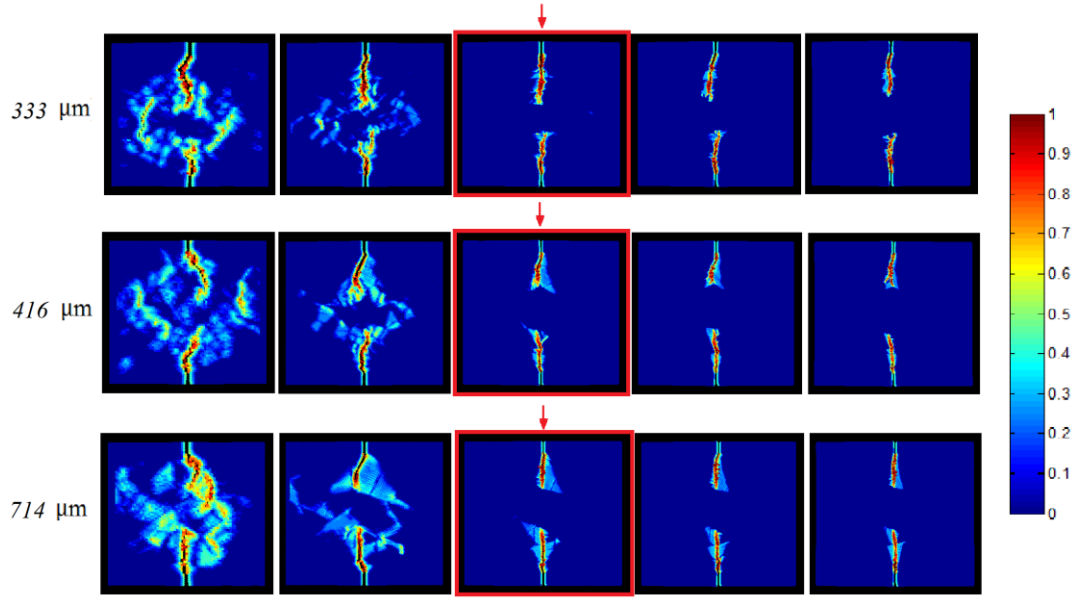

Fig. 23 GBC = 2, time = 2.4 µs. Fracture pattern comparison of three polycrystals with different average grain size (333 µm, 416 µm and 714 µm) and five different horizon values: from left to right, 202.7 µm (74 x 74 particles), 100 µm (150 x 150 particles), 50 µm (300 x 300 particles), 37.5 µm (400 x 400 particles) and 30 µm (500 x 500 particles)

4.5.3.2 Grain size effect on time-to-failure and fracture behaviour

The aim of this section is to investigate the effect of the grain size on the time-to-failure, i.e. the time-lapse between the application of the load and the first incremental extension of the initial notch, and fracture behaviour. For this purpose, a double-edge notched plate, shown in Fig. 20, with 300 x 300 particles and GBC = 0.5 is considered. Same boundary conditions, time step size, time integration scheme and values of grain size are used as in Section 4.5.3.1. For each of the three values of grain size, ten simulations are performed (each one with random grain orientation) for a total of twenty data points (also called “repetitions”) for each grain size, i.e. two data points for each simulation since the plate has two notches. This is done to purify our conclusions on the effect of the grain size from the effect of the grain orientation.

As already mentioned in Section 4.5.3.1, if the dimensions of the plate remain the same, the smaller the grain size the higher the volume fraction of grain boundaries

and the higher the probability that a grain boundary exists in proximity of the initial crack tip. Therefore, if we define the "occurrence" as the event in which the initial notch propagates to form a major crack (vid. Fig. 24), it is expected that the smaller the grain size the higher the number of occurrences.

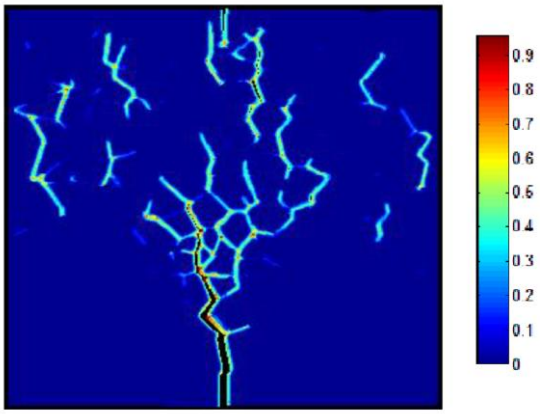

Fig. 24 Meaning of occurrence: occurrence (bottom notch), non-occurrence (top notch)

However, PD results contradict this expectation. As shown in Fig. 25, the percentage of occurrences (i.e. the number of occurrences divided by 20) is approximately the same for all values of grain size considered in this study. More precisely, it has a slight tendency to increase as the grain size increases. The video of the simulations have also helped in shedding some light on this unexpected result. According to the author, there are two competing mechanisms at play. The first one is the mechanism mentioned earlier that was understood and expected even before running the simulations, i.e. the smaller the grain size the higher the probability that a grain boundary exists in proximity of the initial crack tip, which encourages the propagation of the initial notch (vid. bottom notch in Fig. 24) and raises the number of occurrences. The second mechanism can be described as follows: the smaller the grain size, the higher the volume fraction of grain boundaries, the higher the number of weak points within the material and, as a result, the higher the probability of new cracks nucleating, propagating and protecting and shielding the initial notch from the external load. This second mechanism can be visualized in Fig. 24, where the top notch is clearly shielded by the nucleation and propagation of two adjacent cracks.

In contrast, no crack nucleates in proximity of the bottom notch, which, therefore, propagates and leads to the formation of a major crack.

This finding reminds the author of a particular toughening mechanism called "microcrack cloud". As described in (Lawn 1993), this is a mechanism induced by the occurrence of microcracks in proximity to the crack tip (vid. Fig. 26), which act as stress relievers and impose a dilatant closure field on the crack. This phenomenon is an open research topic in the field of fracture of polycrystalline materials and quantitative prediction techniques are not well-established due to the extremely complex nature of the phenomenon (Shum & Hutchinson 1990), (W.Hutchinson 1989). As argued in (Ruhle et al. 1987), experimental techniques such as TEM are affected by detectability limitations, while theoretical models cannot fully clarify the mechanical degradation produced by the formation and interaction of microcraks. Analytical, semi-analytical and numerical studies are available, e.g. (Toi & Atluri 1990), (Johnson 2001), (Wang et al. 2014), but they always require artificial conditions (Wang et al. 2014). As mentioned in (Johnson 2001), they often assume fixed and already nucleated microcrack configurations and do not consider the polycrystalline nature of the material. The following statement can be found at page 216 in (Lawn 1993): …*The issue of microcrack toughening raises two fundamental questions: what are the condition that a microcrack cloud should initiate in the field of a primary crack?; given that these conditions are met, what is the toughness increment?*... Returning to our PD results, it would be interesting to understand why only the top notch in Fig. 24 benefits from the shielding effect. According to the author, several factors could be responsible for this situation, e.g. the grain orientation, the value of GBC, the grain size, the magnitude of the load, the type of load and the morphology of the crystals. In this study, the author limits himself to report this finding and a detailed investigation of these effects will be considered as future work.

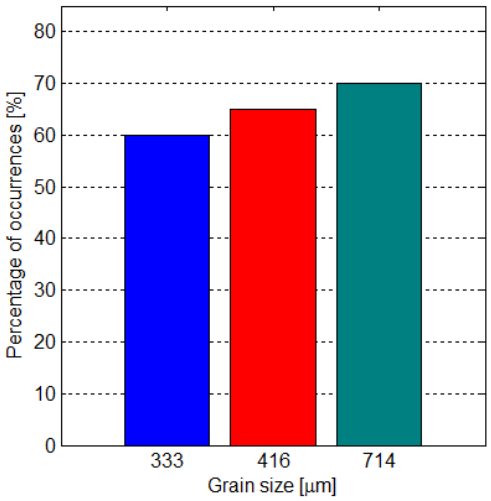

Fig. 25 Grain size effect on the number of occurrences

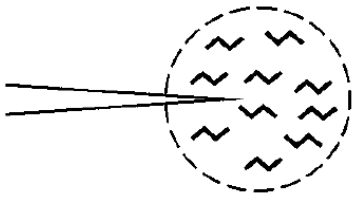

Fig. 26 Microcrack cloud mechanism (Lawn 1993)

The results concerning the effect of the grain size on the time-to-failure is presented in Fig. 27. As already mentioned, ten simulations are performed (each simulation has a random grain orientation) for each grain size. Moreover, the damage index in proximity to the crack tip is monitored and 20 data points (i.e. the time-to-failure) for each grain size are collected, for a total of 60 data points. Fig. 27 is constructed by considering only the time-to-failure of occurrences, i.e. the value of the time-to-failure is only determined if the initial notch propagates and forms a major crack such as the bottom notch in Fig. 24. Since the number of occurrences depends on the grain size, the curves in Fig. 27 are constituted of a different number of data points. By observing Fig. 27, it can be concluded that the average time-to-failure is influenced by the grain size. More precisely, the higher the grain size the higher the

average time-to-failure. The first mechanism mentioned above, i.e. the smaller the grain size the higher the probability that a grain boundary exists in proximity to the initial crack tip, is probably responsible for this effect. In contrast, the second mechanism, i.e. microcrack shielding, is excluded here since only the time-to-failure data of occurrences is considered. Another important point is the amplitude of fluctuation of the curves in Fig. 27. It is observed that the lower the grain size the lower the amplitude. This behaviour is reasonable since a smaller grain size generally means a more homogeneous polycrystal, which is also supported by the findings reported in (Sfantos & Aliabadi 2007a), where the mechanical behaviour of a SiC polycrystal in tension is analysed by using a boundary cohesive grain element formulation. The reason for the fluctuations in Fig. 27 can be found by observing the microstructure of the polycrystal. For example, let's consider the lowest point of the blue curve. As can be seen in Fig. 28, the crack tip of the initial notch is located in proximity to one of the grain boundaries of the polycrystal. Hence, the value of the time-to-failure is lower than the average time-to-failure. In other words, the initial notch starts to propagate earlier. In contrast, if the peak value of the blue curve is considered and the final fracture pattern of the polycrystal shown in Fig. 29 is analysed, it can be seen that the initial notch is farther from the nearest grain boundary, leading to a delay in the onset of the propagation of the initial notch.

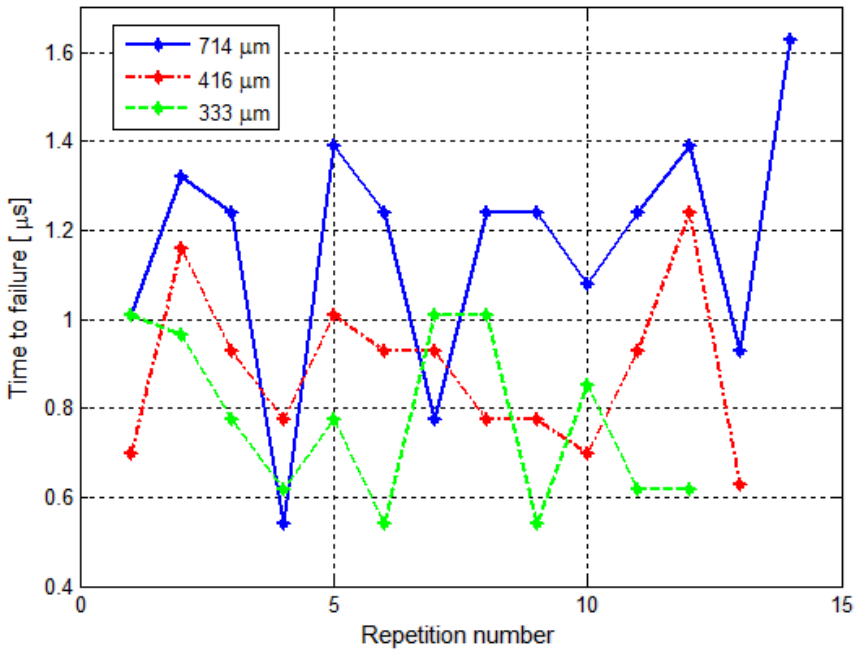

Fig. 27 Grain size effect on time-to-failure

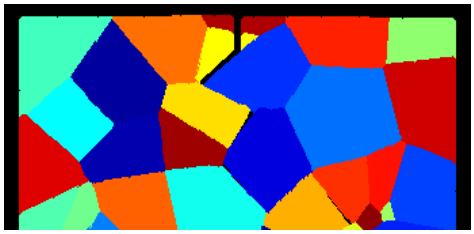

Fig. 28 Top half of the polycrystal: crack tip in proximity to the grain boundary (lowest point of the blue curve in Fig. 27)

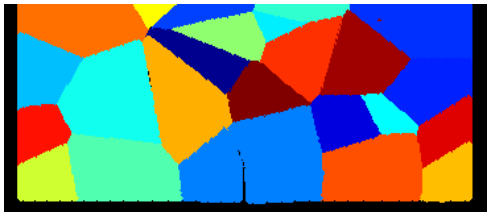

Fig. 29 Bottom half of the polycrystal: crack tip embedded inside the grain boundary (peak of the blue curve in Fig. 27)

4.5.3.3 GBC effect on crack propagation speed

The scope of this analysis is to investigate the effect of GBC on the crack propagation speed. For this purpose, the same configuration is considered as in Section 4.5.3.2 with the following three modifications: 1) the bottom notch is removed from the model, 2) the length of the initial notch is increased from 0.4 mm to 1.4 mm and 3) the velocity boundary condition is substituted by an opening load applied instantaneously at the flanks of the initial notch as in the experimental study reported in (Chandar & Knauss 1982) and in the numerical study reported in (Bobaru & Hu 2012) and kept constant throughout the simulation. The reason for these modifications is that the author wants to reproduce a situation where a single crack propagates from the initial notch without any new crack nucleating in other parts of the plate, which would make more difficult the tracking of the crack tip and more ambiguous the calculation of the crack speed. Four different simulations are carried out by considering the following values of GBC: 0.7, 1, 5 and 10. The value of the applied load is 1500 MPa, the total simulation time is 3.2 μs, the average grain size is 333 μm and the grain orientation is always the same in all four simulations. The position of the crack tip is identified by a damage index value of 0.35 as in (Ha & Bobaru 2010). In the case of crack branching as seen in the first picture in Fig. 31, the longest branch is followed and considered for the calculation of the crack speed.

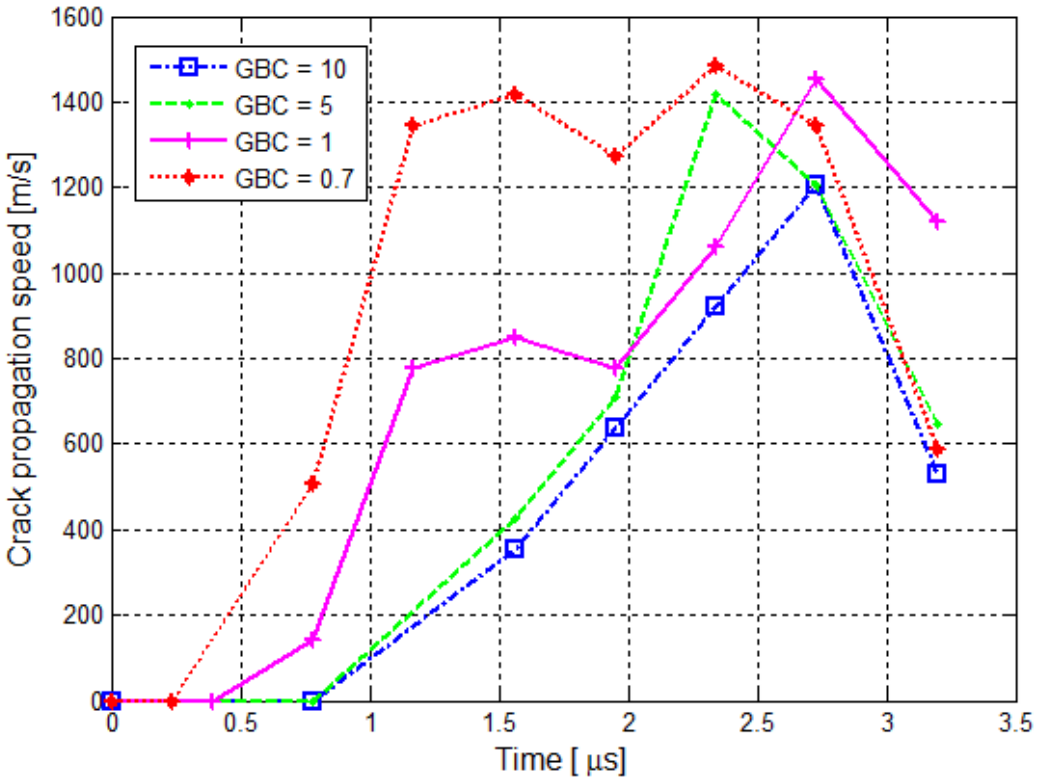

Fig. 30 Effect of GBC on crack propagation speed

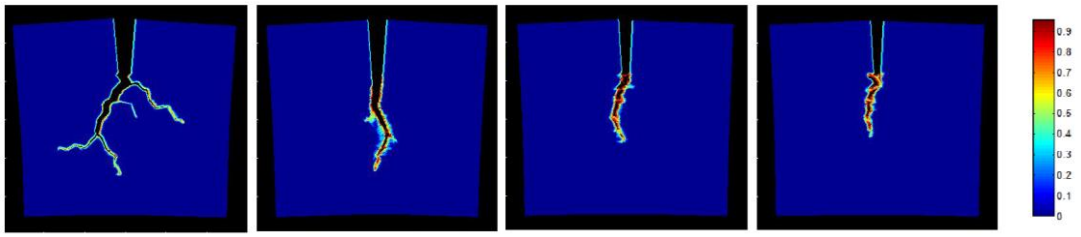

Fig. 31 Effect of GBC on damage map at time = 3.2 µs. From left to right: GBC = 0.7, GBC = 1, GBC = 5, GBC = 10

As can be seen in Fig. 30, the lower the GBC the lower the time-to-failure, i.e. the initial notch starts to propagate earlier, which is in agreement with the expectations of the author. However, the time-to-failure of the simulations with GBC = 5 and GBC = 10 is about the same, meaning that the effect above mentioned may be active only in a limited range of GBC; further investigation concerning this range is part of

the future work. After fracture initiation, the crack speed increases very quickly in all four cases and, after having reached a peak value, it decreases sharply. The overall trend of the crack speed is in good qualitative agreement with the numerical results reported in (Bobaru & Hu 2012), (Ha & Bobaru 2010), (Ha & Bobaru 2011), where PD is used to predict the failure of a single-edge notched specimen subjected to an impulsive opening load. Another important point is related with the peak value of the crack speed. As shown in Fig. 30, the lower the GBC the greater the peak value of the crack speed, which is logical since the weak grain boundaries are a path of preferential failure. The final important point is related with the significant difference in final crack speed between the simulation with GBC = 1 and the other three simulations (vid. Fig. 30). This result can be explained as follows: when GBC = 0.7, the crack is further slowed down by branching which allows the energy to be dissipated in multiple directions. The branching behaviour does not occur in the other three simulations. In contrast, for the cases GBC = 5 and GBC = 10, the crack is further slowed down by the augmented resistance of the grain boundaries, which hinder the crack propagation. For the case with GBC = 1, none of the previous two phenomena occur and this is the reason for the higher value of final crack speed.

4.5.3.4 The effect of fracture toughness on fracture morphology

The aim of this section is to investigate the effect of K_{IC} on fracture morphology. For this purpose, the same configuration analysed in Section 4.5.3.3 is considered with the only difference being the average grain size, which changes from 333 μm to 416 μm. Five different simulations are carried out by considering the same polycrystal with GBC = 1 and the following values of χ: 0.2, 0.35, 0.5, 1 and 2, where χ is defined as

$$\chi = \frac{K_{IC}^{*}}{K_{IC}} \tag{25}$$

In Eq. (25), K_{IC}^{*} is the effective value of fracture toughness used for the simulations, whereas K_{IC} is the nominal fracture toughness of the material, i.e. 58.4 MPa$\sqrt{\text{m}}$. It is worth noting that, as given in Eqs. 17-19, there is a relationship between the fracture toughness and the critical stretch s_0. Therefore, as the fracture toughness, K_{IC}^{*}, changes, the critical stretch, s_0^{*}, used in our simulations changes as well. As shown in Fig. 32, for the values of $\chi \leq 0.5$, crack branching appears to be significant. Moreover, in this range of values of χ, it is observed that the lower the value of χ the higher the number of branches. This is in qualitative agreement with the findings reported in (Espinosa & Zavattieri 2002b), where a similar analysis is carried out for a polycrystalline material subjected to impact load by using FEM and cohesive elements.

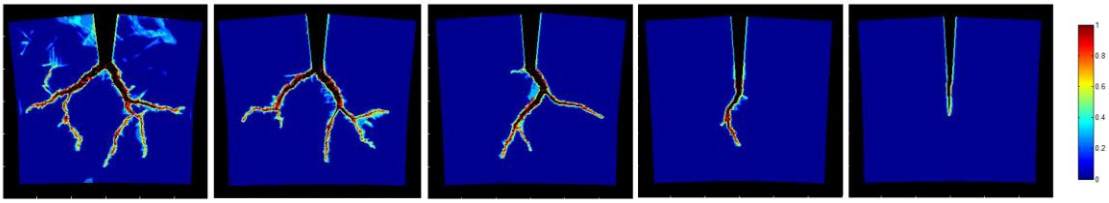

Fig. 32 Effect of K_{IC} on the morphology of damage (time = 3.2 μs). From left to right: $\chi = 0.2$, $\chi = 0.35$, $\chi = 0.5$, $\chi = 1$, $\chi = 2$

4.5.3.5 Plane stress vs. plane strain and intergranular/transgranular fracture

The aims of this section are: 1) to understand how the morphology of fracture changes when plane stress condition is considered rather than the plane strain condition and 2) to capture the intergranular/transgranular failure modes when the value of GBC is varied. For this purpose, a 5 mm x 5 mm double-edge notched polycrystal constituted of 150 randomly oriented grains is considered. The peridynamic discretisation is created with 150 x 150 particles. An explicit central difference scheme is used for the time integration with the total simulation time of 4 μs and the time step size $dt = 2$ ns. Both left and right edges of the polycrystal are subjected to a horizontal velocity boundary condition V = 50 m/s. Three layers of

virtual particles are placed along the left and right edges of the plate to impose the velocity boundary condition. Moreover, in order to allow the external load to be transferred to the inside of the plate, a no-fail zone is imposed on the virtual particles and their neighbours. The values of grid spacing and horizon's radius are $\Delta = 3.33 \cdot 10^{-5}$ m and $\delta = 1.005 \cdot 10^{-4}$ m, respectively. The length of the two initial cracks at the bottom and top edge of the polycrystal is 0.4 mm (Fig. 20). Three different values of GBC are considered to investigate the intergranular and transgranular fracture modes of the polycrystal.

According to Eqs. 19-20, the only difference between plane stress and plane strain configurations in our PD model is the value of the critical stretch, which is lower in the case of plane strain configuration. Figs. 33-35 show the dynamic response of the polycrystal in plane stress condition at four different times for GBC = 0.5, GBC = 1.0 and GBC = 2.0, respectively.

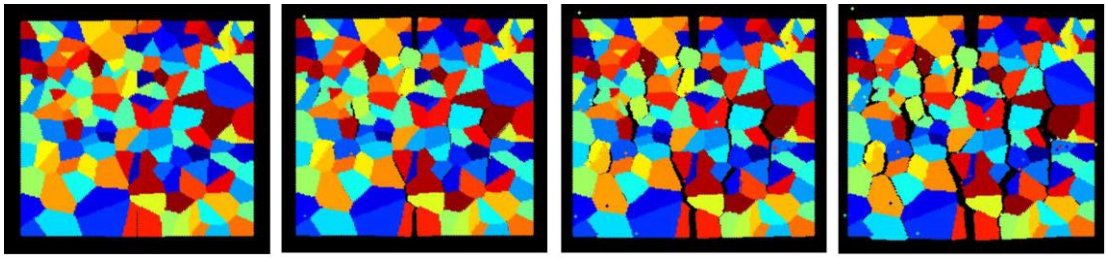

Fig. 33 Time evolution of damage in an initially-damaged polycrystal in plane stress configuration when GBC = 0.5. From left to right: time = 1 μs, time = 2 μs, time = 3 μs and time = 4 μs

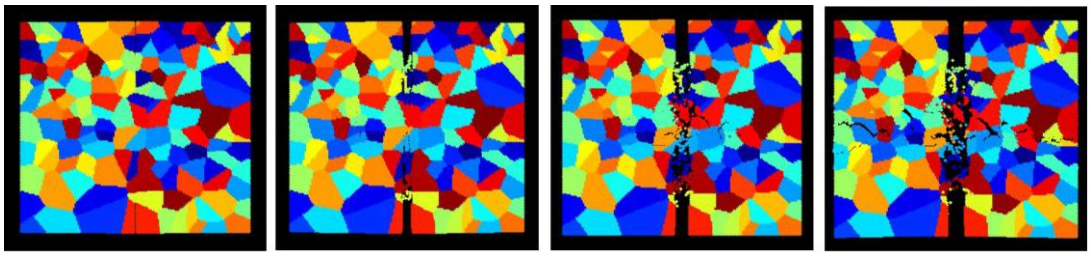

Fig. 34 Time evolution of damage in an initially-damaged polycrystal in plane stress configuration when GBC = 1.0. From left to right: time = 1 μs, time = 2 μs, time = 3 μs and time = 4 μs

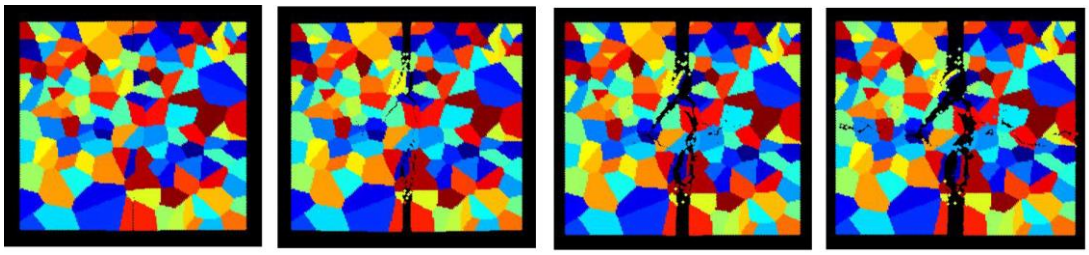

Fig. 35 Time evolution of damage in an initially-damaged polycrystal in plane stress configuration when GBC = 2.0. From left to right: time = 1 μs, time = 2 μs, time = 3 μs and time = 4 μs

In contrast, Fig. 36-38 show the dynamic response of the polycrystal in plane strain condition at four different times for GBC = 0.5, GBC = 1.0 and GBC = 2.0, respectively.

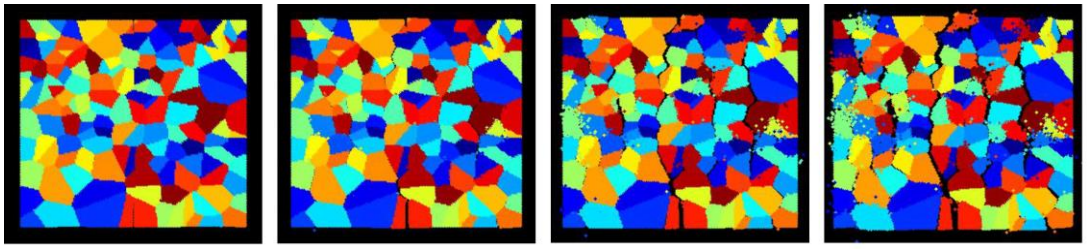

Fig. 36 Time evolution of damage in an initially-damaged polycrystal in plane strain configuration when GBC = 0.5. From left to right: time = 1 μs, time = 2 μs, time = 3 μs and time = 4 μs

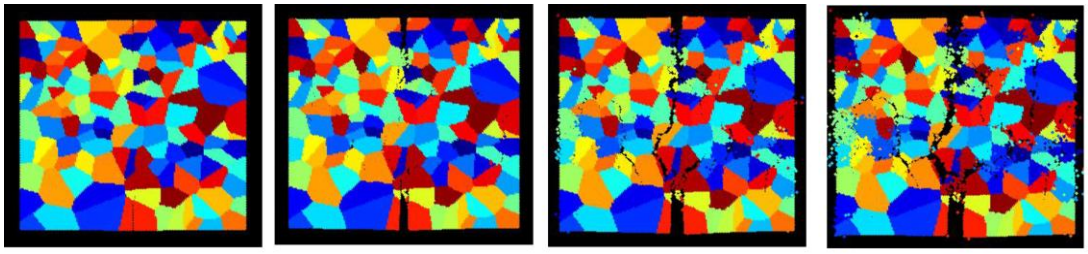

Fig. 37 Time evolution of damage in an initially-damaged polycrystal in plane strain configuration when GBC = 1.0. From left to right: time = 1 μs, time = 2 μs, time = 3 μs and time = 4 μs

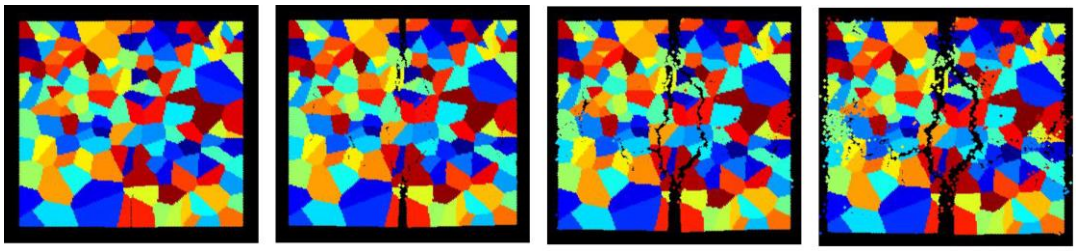

Fig. 38 Time evolution of damage in an initially-damaged polycrystal in plane strain configuration when GBC = 2.0. From left to right: time = 1 μs, time = 2 μs, time = 3 μs and time = 4 μs

The time-to-failure and the overall level of final damage of the structures in plane stress configuration and plane strain configuration with different values of GBC are comparable whereas the aspect of damage is different. Indeed, when GBC = 0.5, the fracture mode appears to be intergranular. On the other hand, when GBC = 1.0 and GBC = 2.0, the fracture mode is similar and prevalently transgranular, which is in qualitative agreement with (Askari et al. 2008), where PD is used to study the transition intergranular/transgranular failure mode in polycrystalline materials. Moreover, two major differences can be noticed when comparing the results of plane stress and plane strain configurations. Firstly, the gap between the flanks of the initial notch appears to be wider in case of plane stress configuration. Secondly, a greater level of fragmentation can be noticed in the case of plane strain configuration. Despite the fact that the material employed in these simulations is the same, both the two previously mentioned features make the aspect of damage qualitatively more brittle in the case of plane strain configuration, since the value of the critical stretch is lower in this case. This is in agreement with the findings reported in Section 4.5.3.4.

4.6 Gaps and future work

Firstly, further improvements to the present study can be made by coupling the microstructural peridynamic model with methods such as electron backscatter

diffraction (Pouillier et al. 2012) to measure crystal orientation with the aim to reproduce an equivalent polycrystalline model instead of producing a random texture. Secondly, experimental studies can be used to validate and refine the damage predictions of the PD model. Thirdly, an extension of the present 2D model to 3D can be considered as future work. Fourthly, as already mentioned, ad-hoc studies are necessary to better understand the shielding effect captured by our PD model (Section 4.5.3.2) and the GBC range where the time-to-failure is effectively influenced by the value of GBC (Section 4.5.3.3). Fiftly, it would be interesting to investigate the effect of the grain size on the crack propagation speed. Lastly, structures of greater dimension could be modelled by coupling the microscopic and macroscopic PD frameworks (i.e. multiscale analysis) and by taking advantage of parallel computing, which can lead to a drastic reduction of the computational time.

4.7 Summary

Polycrystalline materials are among the most common materials used in practical engineering applications. Owing to the high number of variables (e.g. grain size, differences in physical properties between grain and its boundaries, crystallographic orientation, the presence of flaws of different size, shape and orientation) affecting the fracture behaviour of this class of materials, the task of designing safe structures without abusing the use of safety factors is often challenging. Despite the resulting valuable information provided by experimental approaches, these techniques are not always viable. Therefore, computational approaches represent a precious complement for understanding the fracturing of polycrystalline materials. However, the mathematical modelling of the transition from microscopic defects to macroscopic cracks is not entirely understood at present.

In this chapter, a novel peridynamic formulation for studying the fracture behaviour of cubic polycrystalline materials has been introduced, while all the relevant mathematical derivations have been included in Appendix A. Static analyses have been carried out by considering different grain orientations, different loading

conditions and different configurations (plane stress and plane strain). In all cases, a good quantitative agreement has been found between PD and FEM results. Dynamic analyses have also been carried out for different specimen configurations and loading conditions with the aim to investigate the effect of grain size, grain orientation, grain boundary strength, plane stress/strain configuration and fracture toughness on crack speed, time-to-failure, fracture behaviour and fracture morphology. Complex fracture phenomena such as crack nucleation and crack branching have been modelled without using any external fracture criterion and qualitative comparison with other numerical results has been provided. The computational cost of the simulations is of the order of half-hour, which is generally lower with respect to the computational time required by other numerical approaches, such as XFEM. Future work should focus on: 1) modelling realistic microstructures, 2) reducing the computational time by employing multiscale approaches, 3) investigating the shielding and GBC effect on the time-to-failure observed in this study, 4) investigating the effect of the grain size on the crack propagation speed, and 5) 3D modelling. The results of this study have been published in (De Meo, Zhu, et al. 2016) and the main findings can be summarised as follow:

- For the configuration, specimen and conditions considered in Section 4.5.3.2, our PD model predicts lower values of time-to-failure and greater homogenization (lower variance) as the grain size decreases, which is in qualitative agreement with other numerical results. In contrast, the fracture behaviour (i.e. the number of occurrences) is less affected by the grain size and this is explained by the activation of a competing toughening mechanism called microcrack cloud, which is widely reported in the literature.

- The analysis described in Section 4.5.3.3 led to the conclusion that the GBC can affect both the time-to-failure and the peak value of crack propagation speed, which increases as the GBC decreases. In contrast, the time-to-failure increases as the GBC increases, but this is only true in a limited GBC range.

Finally, GBC also affects fracture morphology with crack branching encouraged at lower values of GBC.

- In Section 4.5.3.4, it is observed that crack branching in polycrystalline materials is favoured at lower values of fracture toughness. Moreover, the number of branched cracks increases as the fracture toughness decreases, which is in qualitative agreement with other numerical results.

- The conclusions of Section 4.5.3.5 are such that the fracture morphology in plane strain configuration appears to be more brittle than that in plane stress configuration, which is in qualitative agreement with experimental evidence.

5 Stress-corrosion cracking

5.1 Introduction

In this chapter, a novel numerical multiphysics PD framework for the modelling of adsorbed-hydrogen SCC, based on the adsorption-induced decohesion (AIDEC) mechanism, is presented. The material is modelled at the microscopic scale using microstructural data. First-principle studies available in the literature are used for characterising the process of intergranular material strength degradation. The model consists of a polycrystalline AISI 4340 high-strength low-alloy (HSLA) thin, pre-cracked steel plate subjected to a constant displacement controlled loading and exposed to an aqueous solution of sulfuric acid. Different values of stress intensity factor (SIF) are considered, and the resulting crack propagation speed and branching behaviour are found to be in good quantitative agreement with experimental data available in the literature. The novelty of this work is threefold: (1) the application of PD for the modelling of SCC, (2) the introduction of a novel peridynamic hydrogen grain boundary diffusion model and (3) the prediction of detailed and realistic geometrical features concerning SCC damage in polycrystalline materials (i.e. stable crack propagation, micro-branching and the resulting penetration of the corrosive solution within the structure) that facilitates hydrogen diffusion and accelerates the degradation of the material, which is a salient aspect in real cases.

This chapter is organised as follows: Section 5.2 provides the background and motivation for this study. The PD model of hydrogen grain boundary diffusion and the hydrogen concentration boundary condition are explained in Section 5.3 and Section 5.4, respectively. The coupling between mechanical and diffusion fields is described in Section 5.5, while problem setup, simulation parameters and solution procedure are given in Section 5.6, Section 5.7 and Section 5.8, respectively. Numerical results of fracture initiation, crack speed and crack branching are presented in Section 5.9. Finally, validation of the model against experimental data,

gaps and future work, and summary are provided in Section 5.10, Section 5.11, and Section 5.12, respectively.

5.2 Background and motivation for research

SCC can be defined as the progressive fracturing of the material due to the presence of non-cyclic tensile stress and the exposure to some gaseous and/or liquid environments. SCC can develop in brittle and non-brittle materials, metals and non-metals and can have different morphologies such as intergranular SCC (I-SCC) and transgranular SCC (T-SCC). Crack branching is common in SCC-damaged materials and, in certain cases, the tensile stress necessary to trigger the phenomenon can be as low as 5% of the yield stress (Lynch 2011b). Due to the substantial number of SCC critical environment-material combinations, a wide range of systems related to different industries are affected by this phenomenon such as pipelines, nuclear power systems, aerospace vehicles, boilers, cooling water systems and oil and gas drilling and production systems (Raja & Shoji 2011).

The first catastrophic failures due to SCC occurred in the first years of the 19th century: boiler explosions cost the loss of a large number of human lives. The phenomenon was first recognized in 1873 by W. H. Johnson in a laboratory experiment (Lynch 2011a). Despite the resources and efforts dedicated to the study of this problem, catastrophic failures due to SCC still occur. Moreover, hydrogen is deemed one of the potential candidates to replace fossil fuels. SCC remains, thus, the object of continuous study by academic, industry and other institutions, aimed at, for instance, SCC prediction, SCC monitoring, designing of SCC environmental control procedures and designing of improved SCC-resistant materials.

As comprehensively described in (Lynch 2011b), various theoretical models are available in the literature for explaining the mechanisms that lead or just contribute to SCC. However, there is not much agreement about which mechanisms are more appropriate for particular material-environment combinations. The published literature abounds with SCC experimental data such as those reported in (Han et al.

1998), (Thomas & Bruemmer 2000), (Oriani & Josephic 1974), (Bechtle et al. 2009), (Mine & Kimoto 2011), (Hirose & Mura 1984a), (Hirose & Mura 1984b) and (Yagodzinskyy et al. 2010), but their usefulness is limited by the large amount of parameters contributing to the phenomenon. Moreover, as described in Section 2.4, the number of SCC numerical models is increasing in the scientific literature. However, despite the worthy prediction capabilities and the resulting important insights provided by the use of these numerical techniques, there are various limiting factors and the approach considered in this study (i.e. PD) aims to overcome some of these limitations (vid. Chapter 2).

The material considered in this study is a HSLA steel. Due to their better strength-to-weight ratio as compared to carbon steels, and despite their sensibility to SCC in certain environments such as moist air and water, HSLA steels are broadly used in different industries and systems. As argued in (Lynch 2011b), hydrogen-based SCC mechanisms are widely recognized in high-strength steels, often leading to intergranular brittle fracture where little plasticity can be observed, supporting the idea of a decohesion type of cracking caused by the local hydrogen weakening of interatomic bonds. Moreover, in the case of non-charged hydrogen material exposed to a hydrogen-bearing environment, the predominant SCC mechanism is expected to be hydrogen AIDEC (Lynch 2011b). Therefore, in the present study, hydrogen AIDEC is considered for the modelling of SCC damage in HSLA steels exposed to an aqueous solution of sulfuric acid.

5.3 Peridynamic grain boundary hydrogen diffusion model

Similar to the approach adopted in (Rimoli & Ortiz 2010), in this study, hydrogen grain boundary diffusion is described by considering type C kinetic regime (Harrison 1961) using the widely accepted Fisher model (Fisher 1951). In fact, according to (Mishin & Herzig 1999), the Fisher model is still the foundation of grain boundary diffusion theory. As described in (Harrison 1961), in the case of type C grain boundary diffusion kinetic regime, the bulk diffusion of impurities is

negligible with respect to the diffusion occurring along the grain boundaries. As explained in (Rimoli 2009), this behaviour can be mathematically described by the following reduced version of the Fisher diffusion equation:

$$\frac{\partial C_H}{\partial t} = D_{GB} \nabla^2 C_H \tag{26}$$

where D_{GB} is the grain boundary diffusion coefficient, t is time, C_H refers to the hydrogen concentration at the grain boundaries and ∇ is the Nabla operator. In this study, $D_{GB} = 0.84 \cdot 10^{-9}\ m^2 / s$ is consistent with (Rimoli & Ortiz 2010) and (Serebrinsky et al. 2004).

As mentioned earlier, a novel peridynamic grain boundary hydrogen diffusion formulation, based on the Fisher model, is introduced. By making an analogy with the peridynamic heat conduction equation given in (Oterkus et al. 2014), the peridynamic governing equation for hydrogen grain boundary diffusion can be written as

$$\dot{C}_H(\mathbf{x},t) = \int_{H_\mathbf{x}} f_H\left(C_H(\mathbf{x},t), C_H(\mathbf{x}',t), \mathbf{x}', \mathbf{x}, t\right) \mathrm{d}V_{\mathbf{x}'} \tag{27}$$

where $\dot{C}_H(\mathbf{x},t)$ is the time derivative of hydrogen concentration associated with the generic material point $\mathbf{x}$. In Eq. (27), the peridynamic function $f_H\left(C_H(\mathbf{x},t), C_H(\mathbf{x}',t), \mathbf{x}', \mathbf{x}, t\right)$ is called hydrogen diffusion response function and is defined as

$$f_H = d_{GB} \frac{C_H(\mathbf{x}',t) - C_H(\mathbf{x},t)}{|\mathbf{x}' - \mathbf{x}|} \tag{28}$$

in which the peridynamic grain boundary diffusion bond constant d_{GB} can be expressed in terms of the grain boundary diffusion coefficient as

$$d_{GB} = \frac{6 \cdot D_{GB}}{\pi \cdot h \cdot \delta^3} \tag{29}$$

where *h* refers to the thickness of the plate. As mentioned earlier, the type C grain boundary diffusion kinetic regime means pure grain boundary diffusion, with negligible leakage and diffusion in the bulk. As a consequence, the peridynamic hydrogen diffusion model is constituted by only those bonds that cross the grain boundaries of the material (vid. Fig. 47).

5.4 Hydrogen boundary condition

According to (Hirose & Mura 1984a) and (Hirose & Mura 1984b), hydrogen atoms are generated by the corrosion process at the notch root and are adsorbed by the material. The chemical and physical interactions between material and corrosive solution are complex and particularly challenging to model. According to (Rimoli & Ortiz 2010), it is widely reckoned that these interactions are not entirely understood at present, and, as argued in (Scheider et al. 2008), it is not currently possible to obtain a direct measure of hydrogen concentration in the region adjacent to the crack tip. As described in (Serebrinsky et al. 2004) and in (Sofronis & McMeeking 1989), an alternative approach, adopted in different studies, such as (Scheider et al. 2008), (Raykar et al. 2011), (Alvaro et al. 2014) and (Olden et al. 2014), consists in assuming that hydrogen adsorption can be represented via appropriate boundary conditions. For this purpose, the concept of hydrogen coverage ψ is introduced and defined as

$$\psi = \frac{C_{SH}}{C_{SH}^*} \tag{30}$$

where C_{SH} and C_{SH}^* refer to the surface hydrogen concentration at the crack tip and the surface hydrogen concentration saturation value, respectively.

The numerical results produced by the present study are compared against the experimental data reported in (Hirose & Mura 1984a), where all the surfaces but the crack tip region of a compact tension specimen were painted before the exposure to the aqueous solution of sulfuric acid and to the action of the mechanical load (vid. Section 5.6). As shown in (Rimoli & Ortiz 2010), in order to model this condition, a unit value hydrogen coverage along the crack flanks in the region adjacent to the initial crack tip and a zero value hydrogen coverage on all the remaining surfaces of the specimen can be applied to the model.

5.5 Coupling of mechanical and diffusion field

The coupling of diffusion field and mechanical field is necessary to quantify the material strength degradation due to the local presence of hydrogen and the resulting fracture behaviour. In other words, the adsorption and flow of hydrogen along the grain boundaries of the material is expected to generate a phenomenon of local embrittlement that will change the material response to the applied loading condition. In fact, as described in (Lynch 2011a), the hydrogen AIDEC mechanism is expected to weaken the interatomic bonds leading to local decohesion. The approach adopted in this study builds on earlier work reported in (Serebrinsky et al. 2004), where an impurity-dependent cohesive model informed by first-principle calculations was presented. For this purpose, DFT (i.e. density functional theory) investigations on the decohesion of BCC Fe surfaces exposed to different levels of hydrogen coverage carried out in (Jiang & Carter 2004) were considered and coupled with a UBER (i.e. universal binding energy relation) form interplanar traction-separation relation (Rose et al. 1984) and a renormalisation procedure (Serebrinsky et al. 2004) to address the lengthscale gap between the engineering and the atomistic scale associated with the first-principle calculations. The resulting impurity-dependent model is described by the following equation (Serebrinsky et al. 2004):

$$\sigma_c(\psi) = \sigma_c(0)\left(1 - 1.0467\psi + 0.1687\psi^2\right) \tag{31}$$

where $\sigma_c(\psi)$ represents the peak or critical stress associated with a generic level of hydrogen coverage ψ and $\sigma_c(0)$ refers to the peak stress associated with a zero value of hydrogen coverage. As argued in (Anderson 2005), the mechanical behaviour of HSLA steel can be represented by a linear elastic model. Moreover, considering direct proportionality between $\sigma_c(\psi)$ and the critical stretch $s_0(\psi)$, the variation of the critical stretch as a function of ψ can be written in the same form of Eq. (31) as

$$s_0(\psi) = s_0(0)(1 - 1.0467\psi + 0.1687\psi^2) \tag{32}$$

In other words, the original critical stretch $s_0(0)$ decreases as the local hydrogen concentration increases. In qualitative terms only, Fig. 39 shows the constant mechanical stretch to which a generic PD mechanical bond could be subjected (red line) and the decrement of critical stretch with increasing hydrogen coverage (blue line).

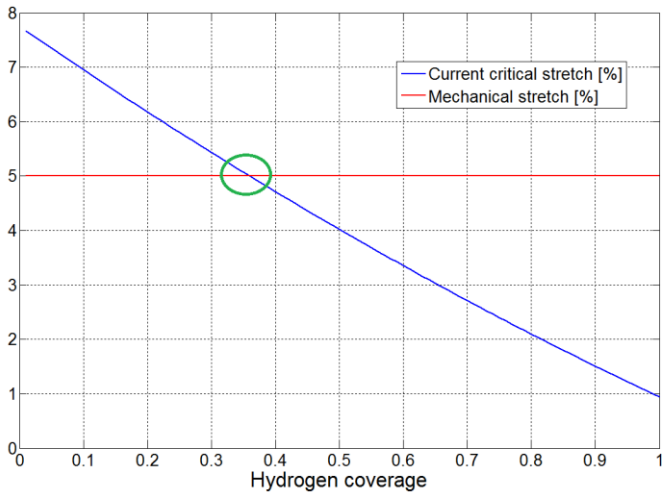

Fig. 39 Break-even point (green circle) for the rupture of a generic PD mechanical bond

5.6 Problem setup

Similar to the case described in the experimental studies (Hirose & Mura 1984a) and (Hirose & Mura 1984b), a pre-cracked AISI 4340 thin steel plate exposed to 0.1N H_2SO_4 aqueous solution is considered and subjected to constant displacement-controlled load applied at the bottom and top edge of the plate (Fig. 40). The material data can be found in Section 4.4. The load is applied statically as a boundary condition and is kept constant throughout the simulation. The plate has length $L = 2.0$ mm, width $W = 0.63$ mm and thickness $h = 5.95 \cdot 10^{-3}$ mm. The length of the initial crack is 1.25 mm.

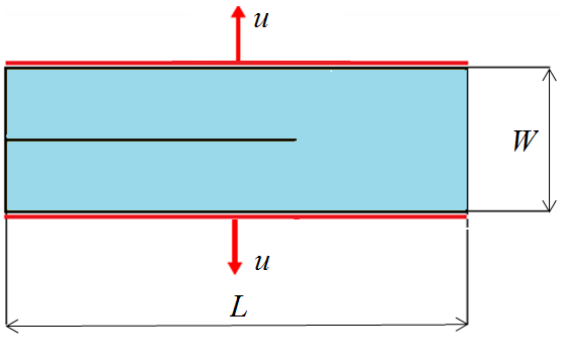

Fig. 40 Mechanical load "*u*"

The magnitude of the vertical displacement-controlled load *u* is specified as to generate a certain constant desired value of stress intensity factor at the crack tip, which is initially lower than the fracture toughness of the material. In other words, the initial load deforms the structure, but not at the point to generate fracture initiation. The five considered SIF values and the respective *u* values are listed Table 2. The displacement values were determined by performing finite element analysis and using special crack tip elements to calculate the stress intensity factors at the crack tip as described in Appendix B.

Table 2 Loading conditions: SIF [MPa$\sqrt{\text{m}}$] vs. *u* [μm]

SIF	13.7	20.6	30.1	40.3	48.55
u	1.157	1.7399	2.5422	3.4	4.1

In order to avoid rigid body motion, the horizontal displacement of two nodes at the centre of the right edge of the plate was constrained. In addition, a constant unit hydrogen coverage is applied at the crack tip as described in Section 5.4.

5.7 Simulation parameters

The plate is constituted of 1407 crystals with an approximate size of about 18 μm as shown in Fig. 41.

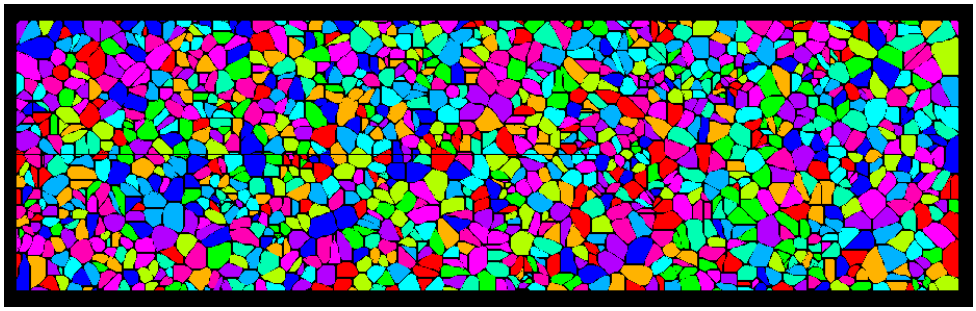

Fig 41 Polycrystal model

The number of real particles along the horizontal, vertical and thickness directions is 336, 106 and 1, respectively. Three layers of virtual particles are placed along the bottom and top edges of the plate to impose the tension-loading boundary condition. The values of grid spacing and horizon radius are $\Delta = 5.95\,\mu\text{m}$ and $\delta = 17.94\,\mu\text{m}$, respectively. The time step size is *dt* = 1 s until fracture initiation. After fracture initiation, the time step size becomes adaptive in order to keep the number of broken bonds sufficiently low in each time step, which is important to allow correct redistribution of the load among the remaining bonds.

5.8 Solution procedure

The present approach can be represented by the diagram in Fig. 42 and described by the following steps:

1) Mechanical step: a displacement-controlled load is applied at the bottom and top surfaces of the specimen until the desired stress intensity factor is reached, and it is kept constant throughout the simulation until fracture initiation. After each increment of crack length, the mechanical step is reconsidered and the load is redistributed among the remaining mechanical bonds.

2) Hydrogen coverage step: a unit value and a zero value of hydrogen coverage are imposed at the crack tip and over all the remaining surfaces of the specimen, respectively.

3) Diffusion step: the peridynamic diffusion model is used to predict the diffusion of hydrogen along the grain boundaries of the material at each time step.

4) Embrittlement step: the relation given in Eq. (32) is used to quantify the effect of the local hydrogen concentration on the material strength. The bond under consideration is broken if its current stretch is greater than the current critical stretch.

5) Dynamic coverage step: a special algorithm is in charge of (1) locating the new position of the crack tip and (2) applying a unit value hydrogen coverage along the flanks of the newly generated crack surface. This step aims to mimic the penetration of the acidic aqueous solution within the material as the crack advances.

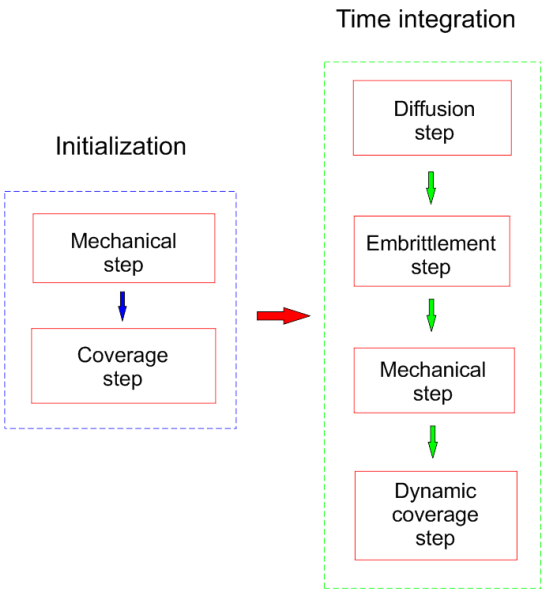

Fig. 42 Solution procedure

5.9 Numerical results

5.9.1 Mechanical step

Fig. 43 and Fig. 44 show the horizontal and vertical displacement fields, respectively, when $u = 3.4$ µm, corresponding to SIF = 40.3 MPa $\sqrt{\text{m}}$.

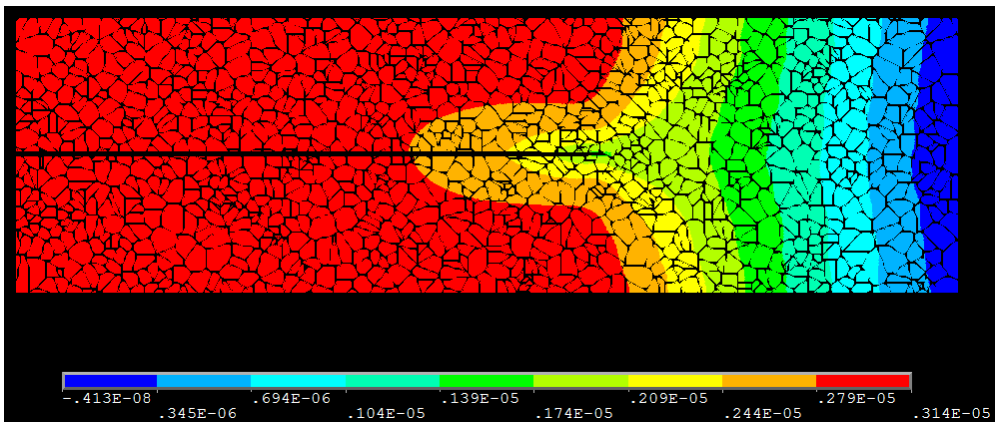

Fig. 43 Horizontal displacement field [m] when SIF = 40.3 MPa $\sqrt{\text{m}}$

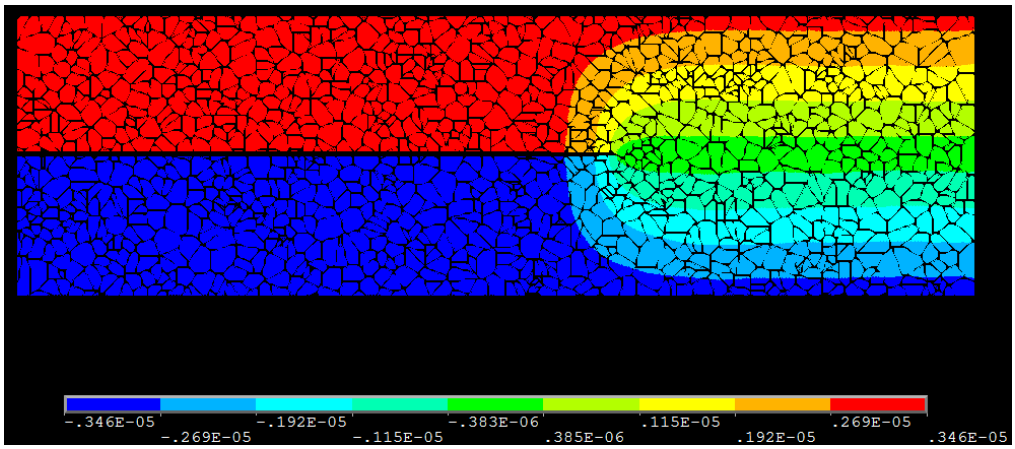

Fig. 44 Vertical displacement field [m] when SIF = 40.3 MPa $\sqrt{\text{m}}$

As expected, due to the displacement constraints described in Section 5.6, the right hand side of the plate experiences the smallest horizontal displacements. In contrast, the opposite side of the plate shows a greater freedom of movement along the x-axis direction. Moreover, the crack front is the region with the smallest vertical displacement, while the crack surfaces allow greater freedom of movement along the y-axis direction. As expected, the maximum stretch occurs at the crack tip (Fig. 45), and its magnitude, for all five loading conditions, is given in Fig. 46.

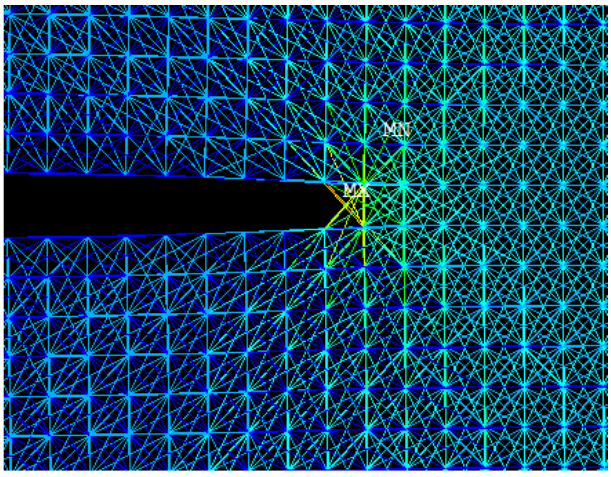

Fig. 45 PD mechanical bonds around the crack tip and crack tip stretch when SIF = 40.3 MPa $\sqrt{\text{m}}$

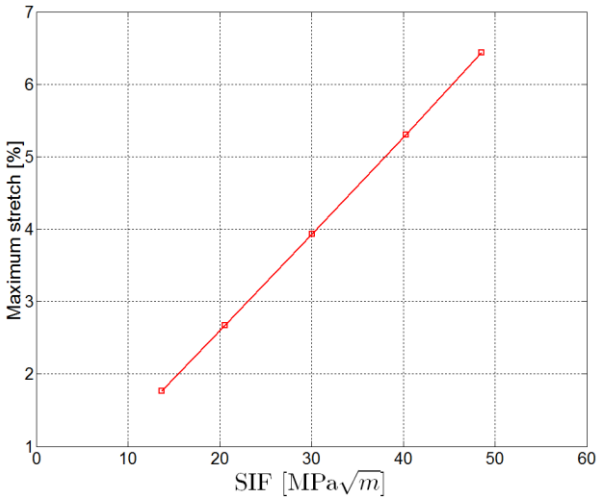

Fig. 46 Maximum stretch [%] vs. SIF [MPa $\sqrt{\text{m}}$]

As expected, the maximum mechanical stretch increases with increasing SIF. In all five loading conditions, the mechanical stretch is inferior to the critical stretch, meaning that no crack propagation occurs at the beginning of the simulation and, as explained in Section 5.5, a reduction in critical stretch is required to obtain crack extension.

5.9.2 Hydrogen diffusion step and fracture initiation

Fig. 47 shows the final hydrogen grain boundary coverage plots for all five loading conditions when fracture initiation occurs. The red colour refers to a unit value hydrogen coverage that corresponds to saturated hydrogen surface concentration.

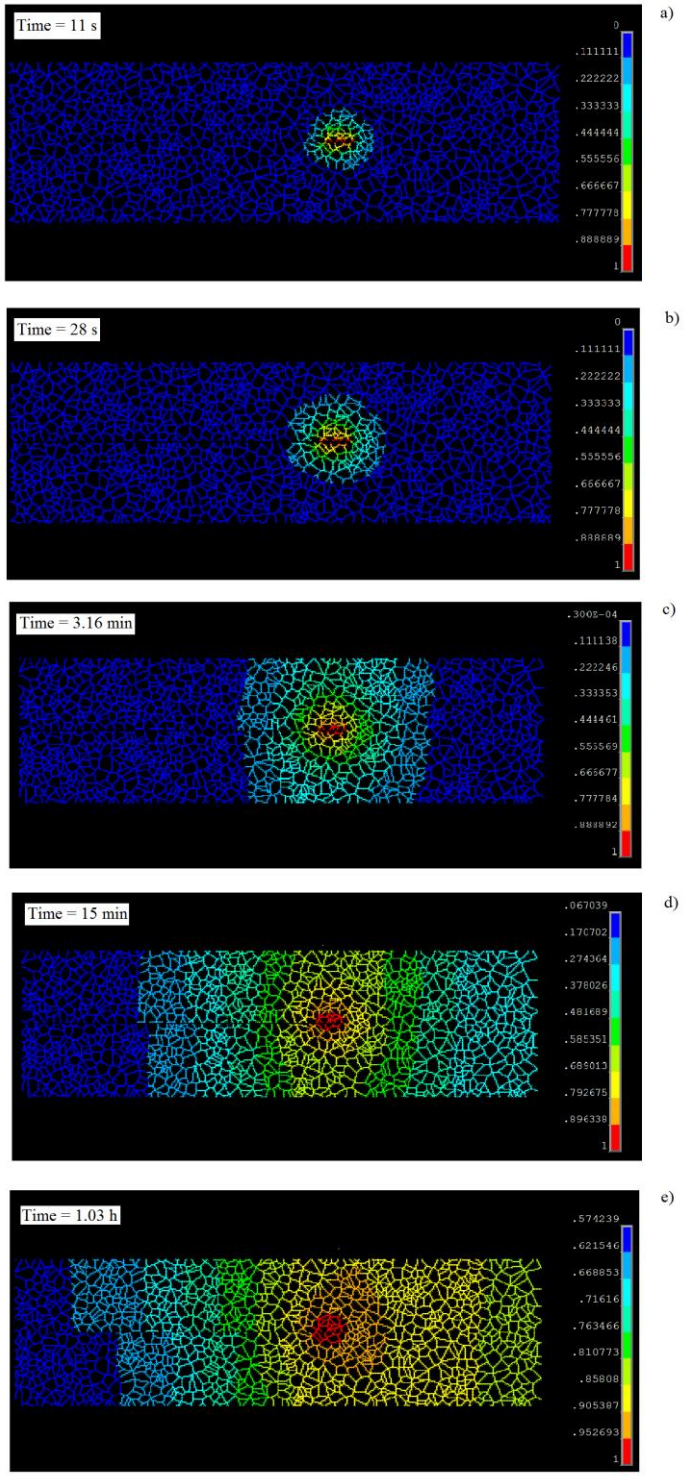

Fig. 47 Hydrogen coverage field at crack propagation initiation times for all five loading conditions: SIF = 48.55 MPa $\sqrt{m}$ (a), SIF = 40.3 MPa $\sqrt{m}$ (b), SIF = 30.1 MPa $\sqrt{m}$ (c), SIF = 20.6 MPa $\sqrt{m}$ (d) and SIF = 13.7 MPa $\sqrt{m}$ (e)

As time progresses, hydrogen diffuses along the grain boundaries of the material, starting from the crack tip region and leading to a local reduction in critical stretch as described in Section 5.5. As shown in Fig. 48 (a), the higher the applied SIF, the lower the hydrogen diffusion time necessary to induce fracture initiation. A detailed view of the appearance of grain boundaries is given in Fig. 48 (b).

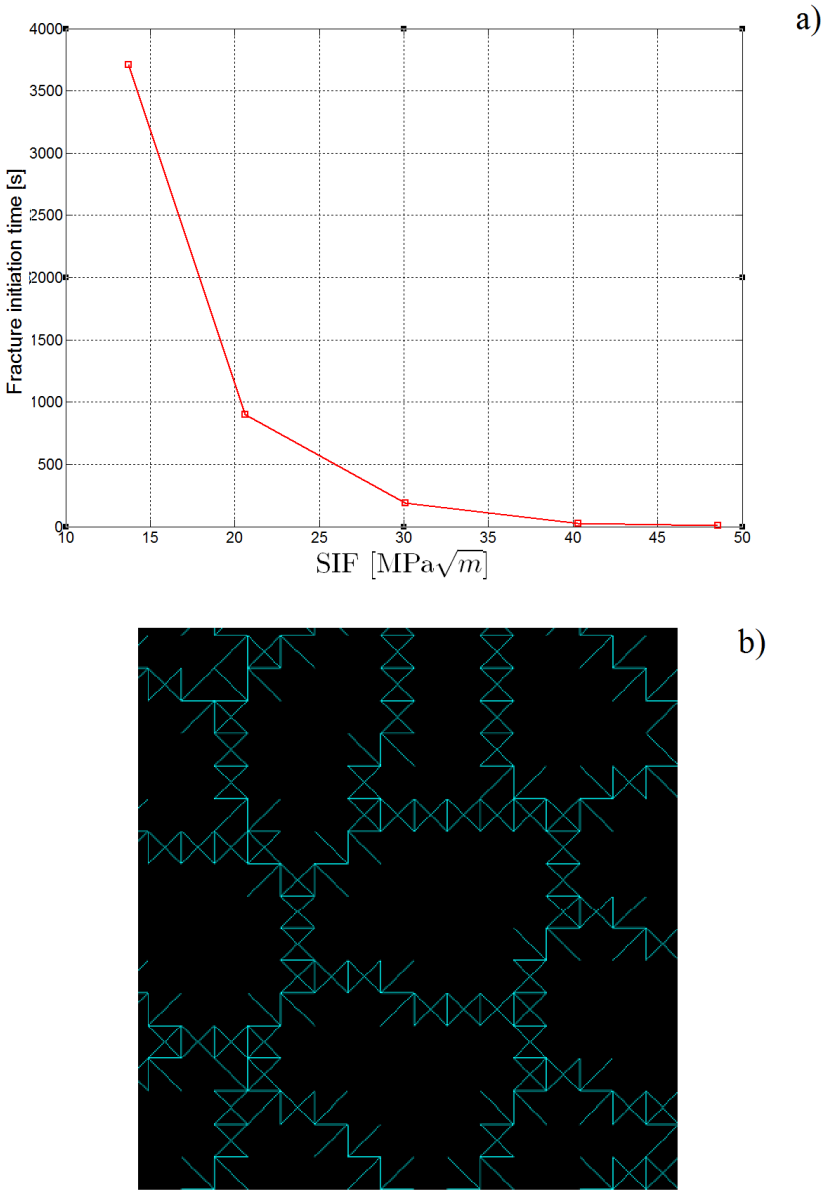

Fig. 48 Fracture initiation time [s] vs. SIF [MPa $\sqrt{\text{m}}$] (a), detailed view of grain boundaries (b)

5.9.3 Crack propagation

Fig. 49 shows the crack propagation path at three different temporal instants when SIF = 48.55 MPa$\sqrt{\text{m}}$. The crack propagates from the crack tip and moves forward along the grain boundaries of the material, showing crack branching in the initial phase of the propagation.

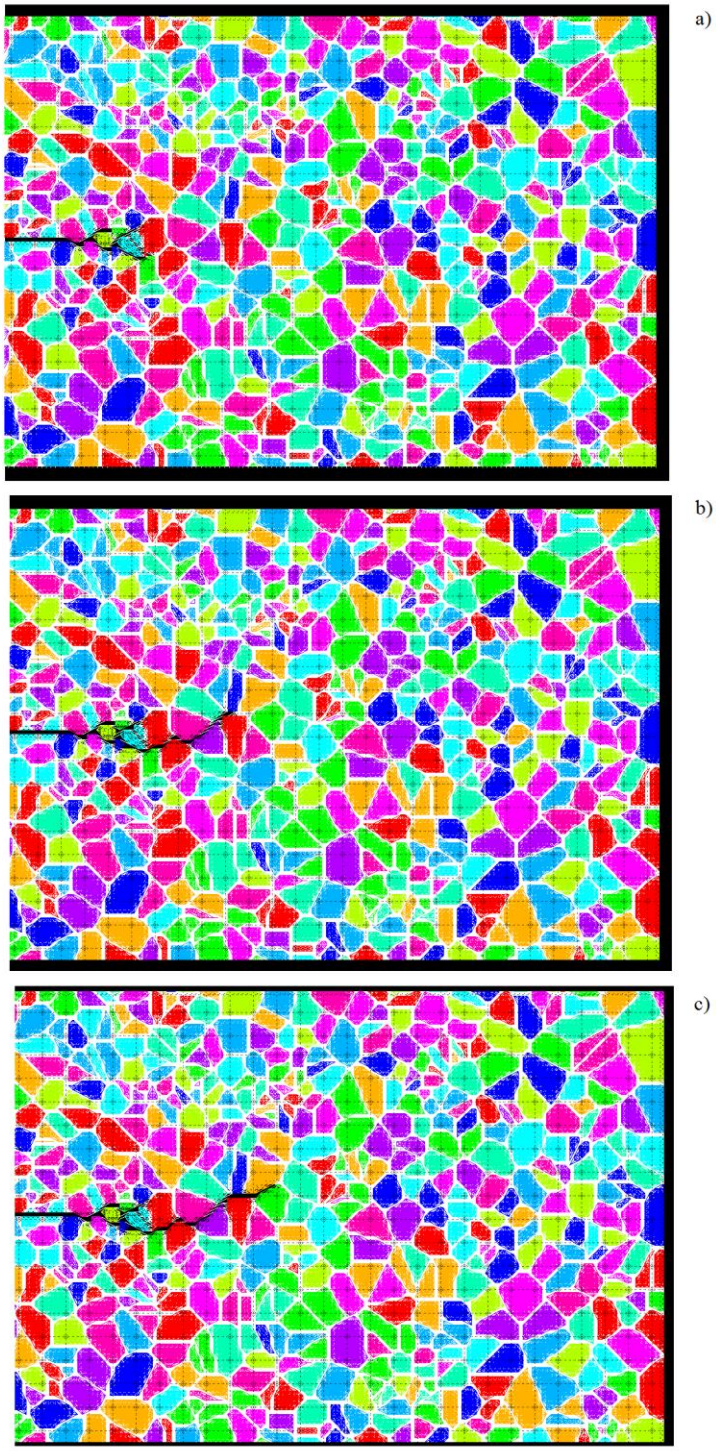

Fig. 49 Crack propagation path when SIF = 48.55 MPa $\sqrt{m}$: time = 13.2 s (a), time = 16.5 s (b), time = 18.1 s (c)

As already mentioned in Section 5.8, in order to simulate the penetration of the corrosive solution within the material as the crack advances, a dynamic hydrogen boundary condition is implemented. In other words, the constant unit value hydrogen coverage, initially applied to the crack tip of the initial crack, is then applied to the newly created crack surfaces as the crack extends (Fig. 50).

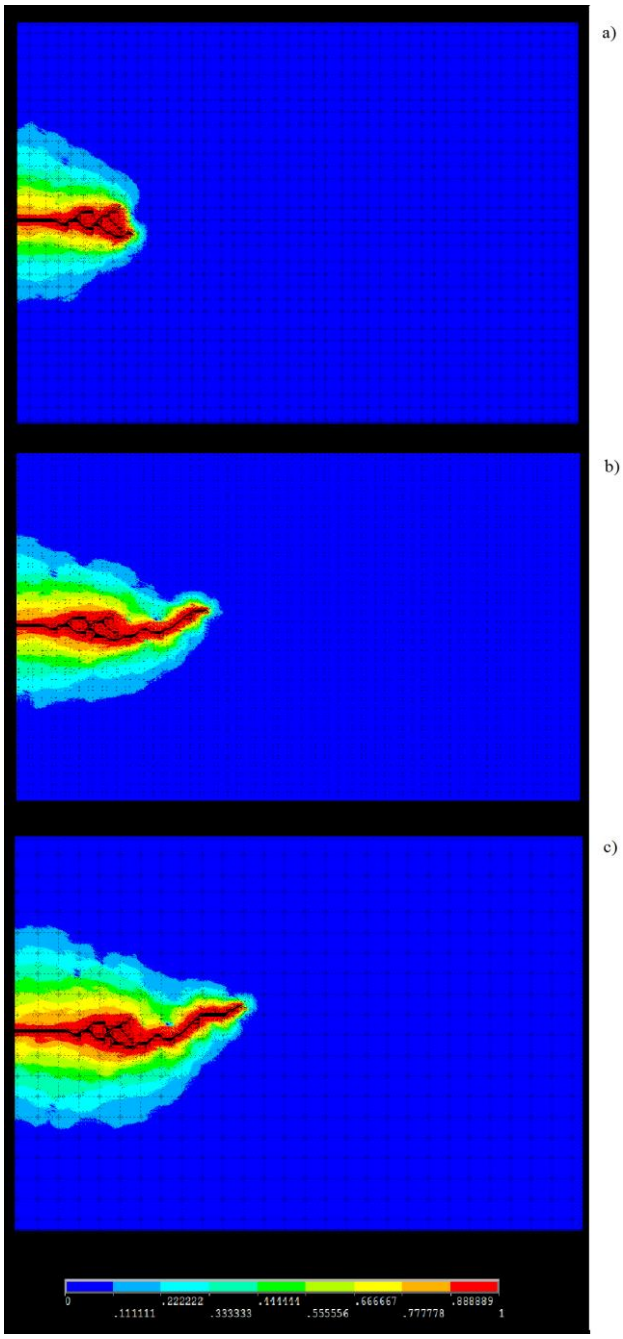

Fig. 50 Hydrogen coverage field when SIF = 48.55 MPa $\sqrt{\text{m}}$: time = 13.2 s (a), time = 16.5 s (b), time = 18.1 s (c)

For the same loading condition, i.e. SIF = 48.55 MPa $\sqrt{\text{m}}$, Fig. 51 shows the vertical displacement field at three different temporal instants as the crack advances.

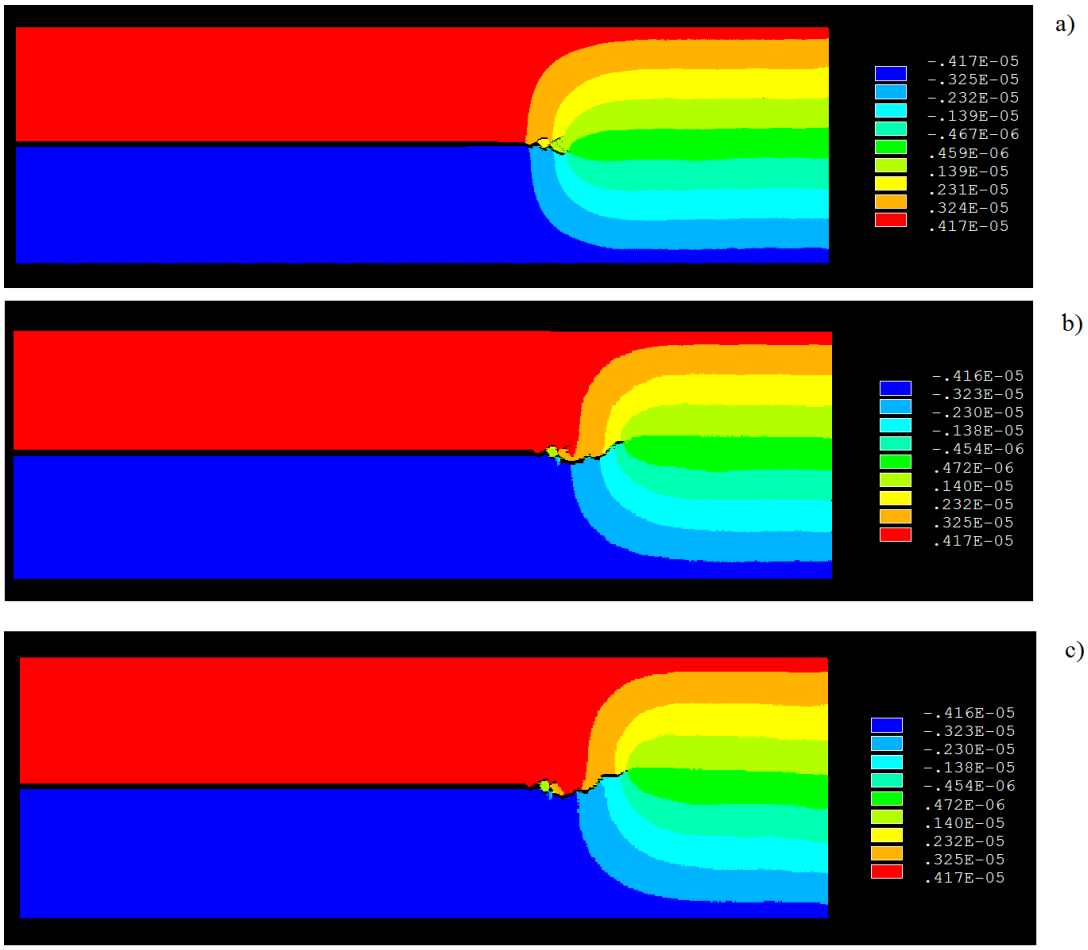

Fig. 51 Vertical displacement field when SIF = 48.55 MPa $\sqrt{m}$: time = 13.2 s (a), time = 16.5 s (b), time = 18.1 s (c)

Fig. 52 compares the crack path predicted for all five loading conditions considered in this study. A micro-branching behaviour is observed at higher values of SIF. The average micro-branching width predicted by the numerical model is in the order of 60 μm.

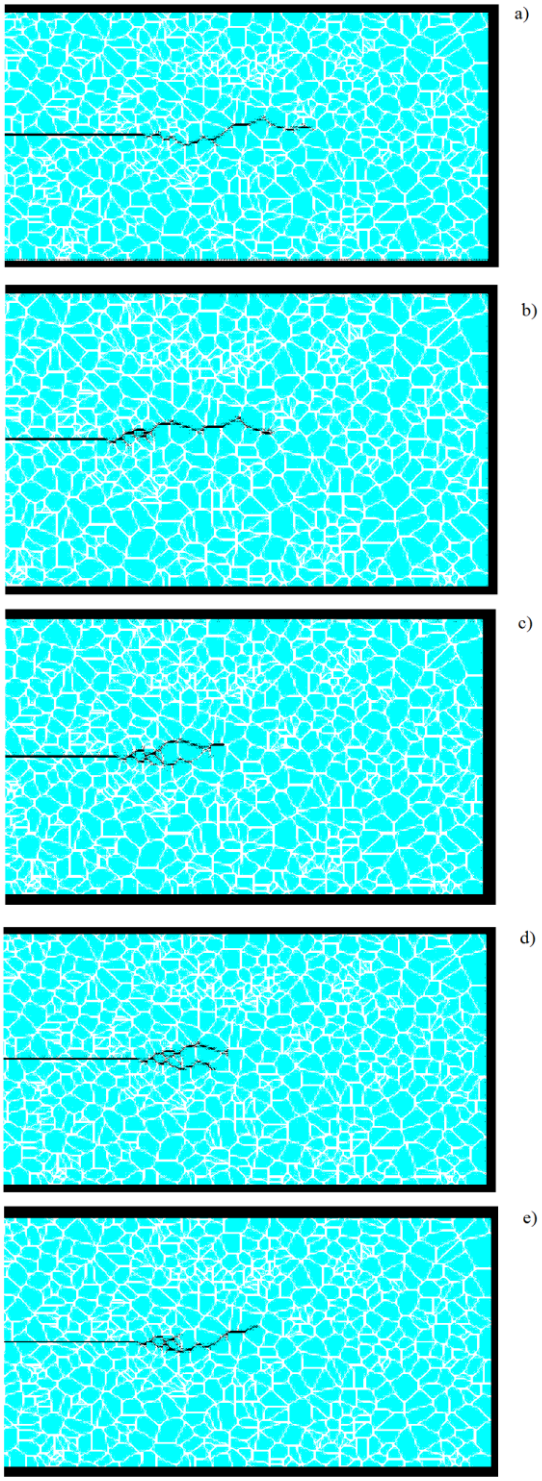

Fig. 52 Crack path: SIF = 13.7 MPa $\sqrt{m}$ (a), SIF = 20.6 MPa $\sqrt{m}$ (b), SIF = 30.1 MPa $\sqrt{m}$ (c), SIF = 40.3 MPa $\sqrt{m}$ (d), SIF = 48.55 MPa $\sqrt{m}$ (e)

5.10 Validation

Concerning the hydrogen plot shown in Fig. 50, the algorithm is clearly able (1) to track the current position of the crack tip as the crack advances and (2) to update the hydrogen boundary condition accordingly. The vertical displacement plot shown in Fig. 51 is also in agreement with the expected behaviour of the structure: a symmetric field is found with respect to the horizontal direction, and the maximum and minimum values of the vertical displacement field are consistent with the applied mechanical load (vid. Table 2 in Section 5.6).

The validation of the current approach is done against experimental data available in (Hirose & Mura 1984a) for the AISI 4340 tempered at 200°C.

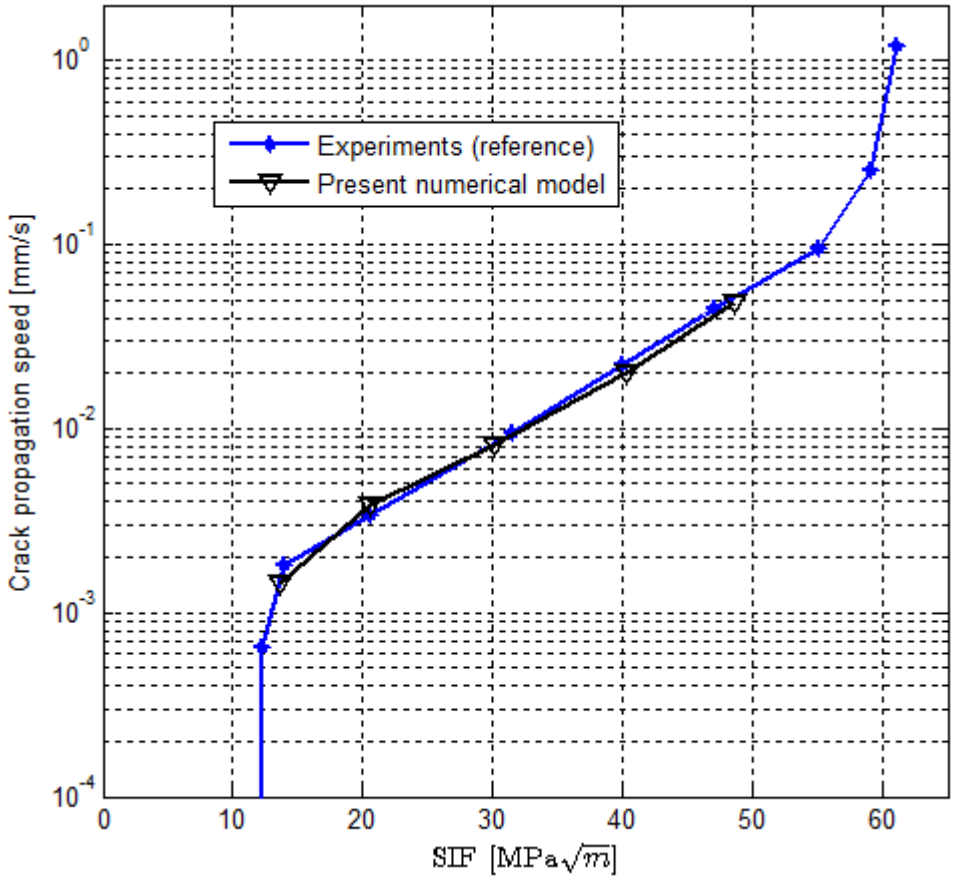

Fig. 53 Crack propagation speed [mm/s] vs. SIF [MPa $\sqrt{\text{m}}$]: present numerical model (black triangles) and experiments (blue diamonds)

Fig. 53 shows the comparison between the present study and experiments in (Hirose & Mura 1984a) concerning the relation between the crack propagation speed (logarithmic scale) and the stress intensity factor for all five loading conditions. The crack speed is calculated for each simulation by dividing the total crack propagation length by the crack propagation time. A satisfactory agreement is observed suggesting that the present peridynamic model is able to capture the main features of the complex interaction between material, environment and mechanical load.

A further agreement between numerical and experimental results is represented by the fact that an appreciable crack micro-branching behaviour is found at higher values of SIF, while for lower values of SIF the crack path is intergranular without any appreciable sign of branching behaviour (cf. Fig. 52 and (Hirose & Mura 1984a)). Moreover, the present peridynamic model is also capable of capturing the width of micro-branching observed during the experiments (vid. Section 5.9), i.e. an average experimental micro-branching width of 20 μm (Hirose & Mura 1984a).

5.11 Gaps and future work

Further improvements to the present study can be made by coupling the microstructural peridynamic model with methods such as electron backscatter diffraction (Pouillier et al., 2012) to measure crystal orientation with the aim to reproduce an equivalent polycrystalline model instead of producing a random texture. Moreover, a reduction in computational time can be obtained by coupling the microscopic and macroscopic mechanical model in the same peridynamic framework. Lastly, the present study can serve as a starting point for more detailed SCC investigations: more complex geometries and loading conditions, 3D models and multiple cracks.

5.12 Summary

SCC can be defined as the progressive fracturing of the material due to the presence of non-cyclic tensile stress and the exposure to some gaseous and/or liquid

environments. Due to the substantial number of SCC critical environment-material combinations, a wide range of systems related to different industries are affected by this phenomenon.

The published literature abounds with SCC experimental data, but their usefulness is limited by the large amount of parameters contributing to the phenomenon. Moreover, the numerical techniques currently available suffer from various limiting factors and the approach considered in this study (i.e. PD) aims to overcome some of these limitations (vid. Chapter 2).

The material considered in this study is a HSLA steel. Hydrogen-based SCC mechanisms are widely recognized in high-strength steels, often leading to intergranular brittle fracture where little plasticity can be observed, supporting the idea of a decohesion type of cracking caused by the local hydrogen weakening of interatomic bonds. Moreover, in the case of non-charged hydrogen material exposed to a hydrogen-bearing environment, the predominant SCC mechanism is expected to be hydrogen AIDEC. Therefore, in this study, a novel numerical multiphysics peridynamic framework for modelling adsorbed-hydrogen SCC in HSLA polycrystalline steel based on the AIDEC mechanism is presented. Microstructural data are used to model the mechanical behaviour of the material and a novel peridynamic hydrogen grain boundary diffusion model is introduced.

Crack propagation speeds calculated for five different loading conditions are found in good quantitative agreement with the experimental data available in the literature. Remarkably, the peridynamic model presented here is also capable of capturing the fracture behaviour of the structure and different micro-branching behaviours and associated geometrical features (micro-branching width) observed in experiments. Future work should focus on: 1) modelling more complex geometries, 2) reducing the computational time by employing a multiscale approach and 3) analysing realistic microstructures. The results of this study have been published in (De Meo, Diyaroglu, et al. 2016).

6 Pitting corrosion

6.1 Introduction

In this chapter, a PD framework for the modelling of pitting corrosion is presented. The couple material/environment considered in this study is austenitic stainless steel grade 304 exposed to 1M NaCl aqueous solution. Metal dissolution is predicted by using a modified Nerst-Planck equation where the coupled effect of diffusion and electromigration is taken into account through an effective diffusion coefficient. Different values of overpotential are applied to the metal and corrosion rate and current density in both activation-controlled and diffusion-controlled corrosion regimes are predicted and compared against experimental data and other numerical results. The advantage of this approach is the possibility to predict subsurface damage. This study extends the work presented in (Chen & Bobaru 2015) and its novelty is fourfold: 1) the present model is implemented via ANSYS in order to take advantage of its implicit solver and, thus, reducing the computational cost of the simulation, 2) a novel procedure is introduced, which allows to reproduce realistic pit morphologies, 3) metal dissolution in a cluster of intermetallic particles (IMPs) and 4) pit-to-crack transition (described in Chapter 7). This chapter is organised as follows: Section 6.2 provides the background and motivation for this study. The PD model of pitting corrosion is explained in Section 6.3, while its implementation in ANSYS is described in Section 6.4. Numerical results and validation can be found in Section 6.5, which consists of the following four different case studies: pitting corrosion in a stainless steel bar (Section 6.5.1), pitting corrosion in a stainless steel plate (Section 6.5.2), reproduction of realistic pit morphologies (Section 6.5.3) and pitting corrosion in a cluster of intermetallic particles (Section 6.5.4). Gap and future work are discussed in Section 6.6, while the summary of Chapter 6 is provided in Section 6.7.

6.2 Background and motivation for research

Pitting is a localised form of corrosion that leads to the formation of corrosion cavities or pits (Fig. 54) due to the breakage of the material's passive film. Therefore, pitting typically occurs in materials such as stainless steel, aluminium, titanium, copper, magnesium and nickel alloys.

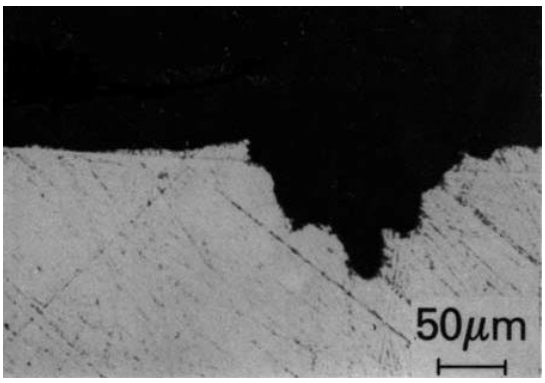

Fig. 54 Cross-sectional view of a corrosion pit in Al 6061 (McCafferty 2010)

Pitting corrosion negatively affects several industries and structures, e.g. gas turbine blades, pipelines, tubes, ships, tanks, offshore platforms, nuclear containers, orthodontic wires, bridges and tunnels (Scheiner & Hellmich 2009). Moreover, as mentioned in (Bhandari et al. 2015), pitting corrosion is the most common, dangerous and destructive type of corrosion in marine and offshore structures. A list of the major catastrophic failures occurred in the oil & gas industry due to pitting corrosion can be found in (Bhandari et al. 2015).

Due to material inhomogeneities, pits can evolve in very different shapes as shown in Fig. 55:

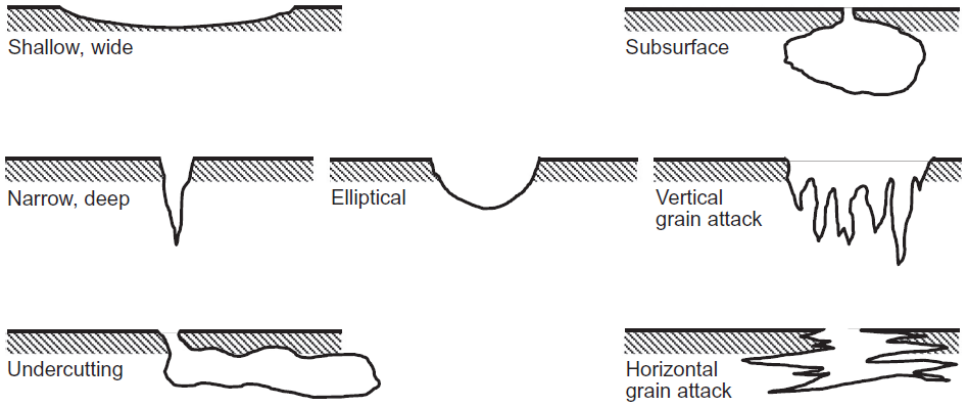

Fig. 55 Possible pit morphologies (Popov 2015)

Apart from the high unpredictability, rapid growth and difficulty of detection that features all localised forms of corrosion, pitting is also dangerous because corrosion pits can act as precursor of SCC and fatigue cracks (McCafferty 2010). As argued in (Van der Weeën et al. 2014), the existence in the structure of just one undetected corrosion pit can compromise the integrity of the entire engineering system, no matter how small and negligible the metal loss could appear.

As described in (McCafferty 2010), the breakage of the material's passive film can occur according to different mechanisms and for different reasons: penetration mechanism (i.e. aggressive ions penetrate the passive film), thinning mechanism (i.e. aggressive ions are adsorbed and interact with the material forming chemical complexes that promote dissolution and thinning of the passive film) and film rupture mechanism (i.e. aggressive ions penetrates through flaws or mechanically damaged areas in the passive film) are the most recognised. These three processes are not mutually exclusive and occur locally due to factors such as compositional heterogeneity (e.g. inclusions, segregates, precipitates), differential aeration (i.e. difference in oxygen concentration between two different regions of the solution), non-uniform acid condensation and salt deposition, and the presence of emerging dislocations and grain boundaries. Due to its high tendency to interact with metal cations, the small dimension and high diffusivity, chloride, Cl^-, is one of the most aggressive ions towards the passive film and is present in many different industries

and environments, e.g. seawater, drinking water, cooling water, salt on roads, food, human body, electronic systems and chemical industry (McCafferty 2010). Some other aggressive ions are fluoride F^-, bromide Br^- and iodide I^- (Groysman 2010). Once the passive film has been broken, the underlying material is exposed to the environment. This small region of the material becomes anodic and undergoes oxidation reaction, whereas the remaining part of the material surface becomes cathodic and undergoes reduction reaction. For a generic metal "Me", the oxidation reduction that occurs at the anode (i.e. the pit surface) can be written as:

$$Me \rightarrow Me^{n+} + ne^- \tag{33}$$

where 'e' stands for electron and '*n*' is the valence number of the metal. In other words, the oxidation reaction consists in 1) the dissolution of the metal into the electrolyte solution in the form of metal cations Me^{n+} and 2) the release of electrons, which flows to the cathodic region through the metallic path. In contrast, the cathodic reaction involves the acquisition of electrons emitted from the anodic area (Fig. 56).

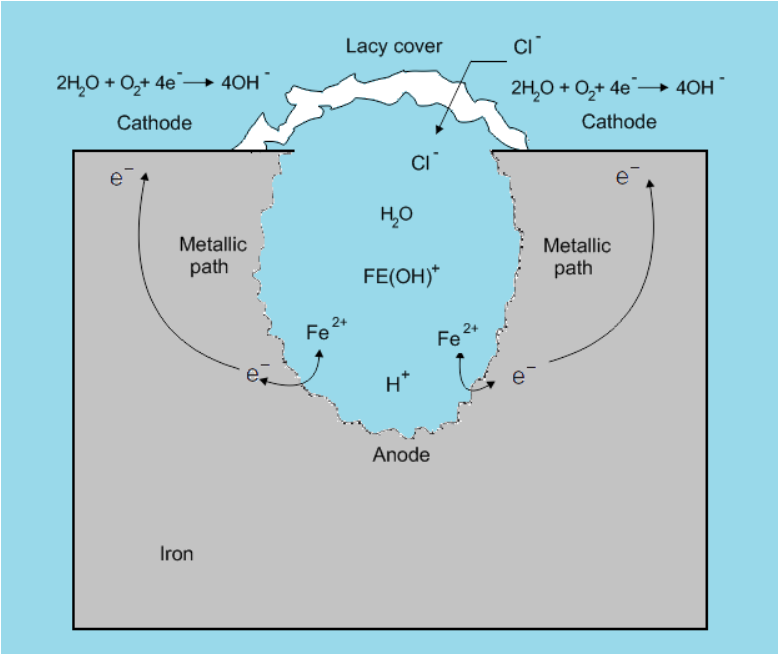

Fig. 56 Pitting corrosion in iron

Depending on the environment, several different cathodic reactions can occur. In the case of low concentration of oxygen dissolved in the electrolyte solution, hydrogen production cathodic reactions tend to dominate, as shown in Eq. (34) and Eq. (35) for acidic solutions and neutral/alkaline solutions, respectively.

$$2H^+ + 2e^- \rightarrow H_2 \tag{34}$$

$$2H_2O + 2e^- \rightarrow H_2 + 2OH^- \tag{35}$$

In contrast, in the case of solutions with high concentration of dissolved oxygen, oxygen absorption cathodic reactions tend to dominate, as shown in Eq. (36) and Eq. (37) for acidic solutions and neutral/alkaline solutions, respectively.

$$4H^+ + O_2 + 4e^- \rightarrow 2H_2O \tag{36}$$

$$2H_2O + O_2 + 4e^- \rightarrow 4OH^- \tag{37}$$

The produced metal cations Me^{n+} diffuse toward the pit's mouth, where they react with hydroxyl anions OH^- produced by the cathodic reaction, leading to the formation of hydroxide white deposits, which form a porous cap often called lacy cover (Fig. 56). This cap hinders the detectability of pitting damage and prevents metal cations to diffuse into the bulk solution. As a result, Me^{n+} accumulate inside the pit cavity reducing the pH of the pit solution via a process of hydrolysis which leads to the production of hydrogen cations H^+ as shown in Eq. (38).

$$Me^{2+} + H_2O \rightarrow MeOH^+ + H^+ \tag{38}$$

As a result of the accumulation inside the pit cavity of positive charged ions, i.e. Me^{n+} and H^+, Cl^- have to migrate inside the pit cavity in order to maintain charge neutrality. In this stage, Me^{n+} and Cl^- interact leading to the formation of metal chloride salts.

Pitting corrosion is usually characterised by two regimes: activation-controlled regime and diffusion-controlled regime. Initially, the dominant regime is activation-controlled, which is the faster of the two and is characterised by the out-diffusion of metal cations Me^{n+} from the solid into the electrolyte solution. In this regime, the driving force of the process is the concentration gradient of metal cations (diffusion) and the potential gradient (migration) at the solid/liquid interface. In time, chloride salts accumulate at the solid/liquid interface and, when their concentration reaches the saturated value in the solution, the pitting corrosion regime changes from activation-controlled to diffusion controlled (also called polished state). In this regime, the out-diffusion of metal cations from the solid metal to the salt layer can occur only when metal cations in the salt layer diffuse into the electrolyte solution. Moreover, due to the high electrical resistance of the salt layer, the migration contribution can be neglected during the diffusion-controlled regime (Scheiner & Hellmich 2007).

Other important concepts in pitting corrosion are chemical potential, electric potential ϕ, electrical double layer (EDL), exchange current density i_0, polarisation and overpotential η (also called overvoltage). Potential energy is the capacity of a system to perform work. As explained in (Groysman 2010), there are several forms of potential energy in nature, e.g. gravitational, nuclear, electrical (e.g. the energy stored between the plates of a charged capacitor) and chemical. The latter can be defined as the capacity of a substance to produce work when it undergoes a change in composition. Therefore, every substance has a chemical potential, which is also called Gibbs energy. Any spontaneous reaction (e.g. corrosion) occurs with a decrease of the Gibbs energy (G), which is used in the study of corrosion thermodynamics. In simple terms, if we consider any of the anodic and cathodic reactions previously described, if the summation of the chemical potential of the products is smaller than that of the reactants (i.e. negative ΔG), then the reaction can occur. The more negative ΔG, the greater the tendency of the reaction to occur. However, it is worth noting that, since corrosion thermodynamics deals only with

processes in equilibrium, it can give information only on the possibility that a reaction will occur (Groysman 2010). Thus, if ΔG is negative, the reaction may or may not occur and, if it occurs, no information is given on the speed of the reaction. As explained in (Trethewey & Chamberlain 1995), this is due to the fact that metal atoms have to overcome a certain energy barrier called "free energy of activation", ΔG^*, which is a fundamental parameter in the determination of the corrosion rate. The field that deals with the influence of various environmental and metallurgical factors on the occurrence and rate of corrosion reactions is called corrosion kinetics.

As a result of the metal dissolution described in Eq. (33), metal atoms will move from the solid to the electrolyte solution in the form of metal cations, while electrons will accumulate at the solid/liquid interface. The so formed capacitor is called electric double layer (EDL) and it is the reason for the presence of an electric potential at the solid/liquid interface. Something similar occurs at the cathodic region. As comprehensively explained in (Groysman 2010), when the electrode potential of anodic and cathodic reactions equals the respective equilibrium electrode potential, anodic and cathodic reactions are said to be at equilibrium, which means that the rate of the forward reaction is the same as that of the reverse reaction. In this case, anodic and cathodic reactions are characterised by the same current density, which is called exchange current density i_0, and no corrosion occurs. As explained in (Trethewey & Chamberlain 1995), the exchange current density can be expressed as

$$i_0 = A_0 \, \mathrm{e}^{\frac{-\Delta G^*}{\mathrm{R}T}} \tag{39}$$

where A_0 is a proportionality constant that include also the effect of the reactants' concentration of the corrosion reaction, T is the temperature and R is the universal gas constant.

Another important concept is that of polarisation, which is defined as a process that causes any change in the electrode potential of a metal. Therefore, if we consider the equilibrium electrode potential as reference, the overpotential (also called overvoltage) can be expressed as

$$\eta = E - E_0 \tag{40}$$

where E is the current electrode potential of the metal and E_0 is the equilibrium electrode potential. There are different forms of polarisation and they can occur both at the anode and at the cathode. The total polarisation is the summation of the anodic and cathodic polarisation contributions, as shown in Eq. (41).

$$\eta = \alpha\eta + (1-\alpha)\eta \tag{41}$$

In Eq. (41), α is called the transfer coefficient and can assume values in the range [0,1]. Corrosion kinetics is based on polarization curves, which describe the relationship between electric current and potential E for both anodic and cathodic reactions. In the case of anodic polarisation, the anodic current density will be greater than the exchange current density. In practical terms, the polarisation effect reduces the energy barrier that metal atoms have to overcome in order to start the corrosion reaction (Trethewey & Chamberlain 1995), i.e.

$$i_a = A_0 \, \mathrm{e}^{\frac{-\Delta G^* + \alpha\eta n\mathrm{F}}{\mathrm{R}T}} = i_0 \, \mathrm{e}^{\frac{\alpha\eta n\mathrm{F}}{\mathrm{R}T}} \tag{42}$$

In Eq. (42), i_a is the anodic current density and F is the Faraday's constant; moreover, it is evident that, when the overpotential is null, exchange current density and anodic current density are the same. As described in (Trethewey & Chamberlain 1995), Eq. (42) can be rewritten in logarithmic form as

$$\eta = \frac{2.303\mathrm{R}T}{\alpha n\mathrm{F}} \lg\left(\frac{i_a}{i_0}\right) = \beta_a \lg\left(\frac{i_a}{i_0}\right) \tag{43}$$

where β_a is the Tafel constant.

For a corrosion reaction to occur, the anodic potential has to be more positive than the anodic equilibrium potential, while the cathodic potential has to be more negative than the cathodic equilibrium potential.

Despite the significant improvements in the understanding of pitting corrosion, many aspects of this phenomenon remain unclear and corrosion rate prediction based on experimental data remains difficult (Onishi et al. 2012). As argued in (Van der Weeën et al. 2014), experimental measurements of corrosion rates under different electrochemical conditions can be complex and time consuming, and the conclusions are limited to the timescale and the conditions in which experiments have been carried out. Moreover, distinguishing the effect of each individual variable becomes extremely difficult (Xiao & Chaudhuri 2011). In order to overcome these limitations, numerical approaches can be a valuable complement (vid. Section 2.5).

6.3 PD model of pitting corrosion

As previously mentioned, the PD framework for pitting corrosion here described builds on the PD model presented in (Chen & Bobaru 2015), whose mathematical formulation is based on a modified version of the Nernst-Planck equation (NPE). The NPE is a mass conservation equation that describes the motion of charged chemical species in a fluid under the effect of concentration gradients (diffusion), electric field (migration) and fluid velocity (convection). In this regard, the flux $\mathbf{N}_i$ in [mol/(m^2/s)] of the generic species '*i*' can be written as (Gavrilov et al. 2007) (Chen & Bobaru 2015)

$$\mathbf{N}_i = \underbrace{-D_i \nabla C_i}_{diffusion} - \underbrace{\frac{\mathrm{F}}{\mathrm{R}T} n_i D_i C_i \nabla \phi}_{electro-migration} + \underbrace{C_i \mathbf{U}}_{convection} \tag{44}$$

where D_i in [m^2/s] is the diffusion coefficient, C_i is the concentration in [mol/m^3] of the species "*i*", F in [C/mol] is the Faraday constant, R in [J/(mol K)] is the universal gas constant, n_i is the valence number, ϕ in [V] or [J/C] is the electric potential and **U** in [m/s] is the flow velocity. The conservation of mass can be written as (Gavrilov et al. 2007)

$$\frac{\partial C_i}{\partial t} = -\nabla \cdot \mathbf{N}_i \tag{45}$$

where *t* in [s] is time and $\nabla\cdot$ is the divergence operator. As already mentioned in Section 2.5, the majority of pitting corrosion models available in the literature focuses on the motion of chemical species inside the electrolyte solution. However, recent experimental studies have revealed the existence of a 'wet region' at the solid/liquid interface of the corrosion pit, where the motion of chemical species can occur (Fig. 57). In other words, the electrolyte solution penetrates the subsurface region of the pit filling the pores of the material, allowing metal dissolution to occur not only at the solid/liquid interface, but also in a subsurface region of the pit.

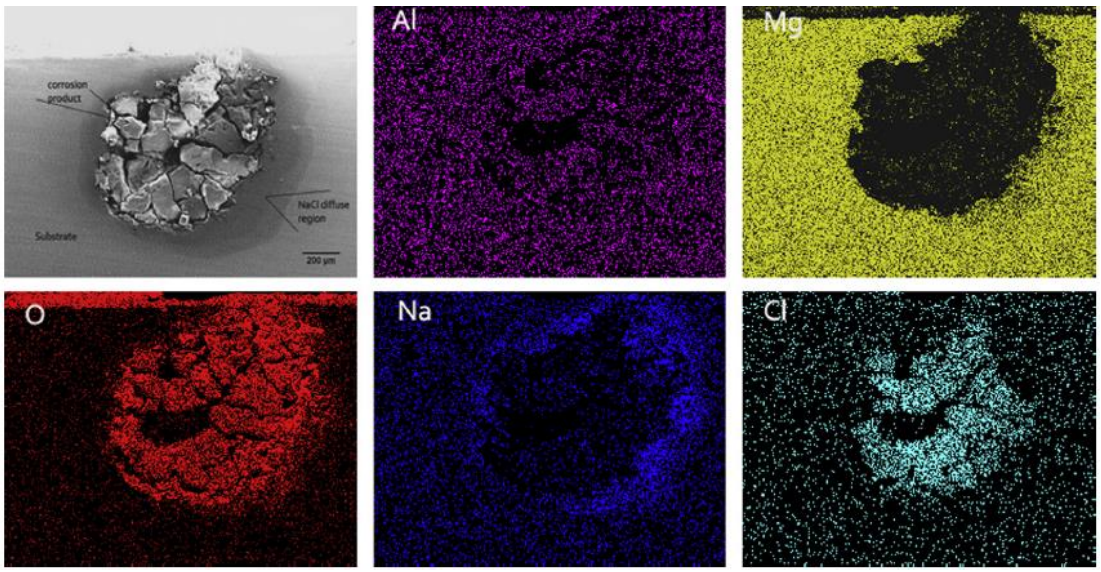

Fig. 57 SEM (top-left picture) of the cross-section of a corrosion pit on a Mg-Al alloy sample immersed in a NaCl aqueous solution after 60 h. X-ray mapping (all other pictures) of the distribution of Al, Mg, O, Na and Cl in the pit region (Song et al. 2014)

In order to capture this process, Eq. (45) is used to predict the motion of metal cations Me^{n+} in both the electrolyte solution and the solid with the following simplifications and assumptions:

Motion within the solution

- The electromigration and convective terms in Eq. (44) are included inside the diffusion coefficient, which is now called effective diffusion coefficient in the liquid D_{ld} .

Therefore, the governing equation used to predict the motion of metal cations within the electrolyte solution is given by the following modified version of the Nernst-Planck equation (vid. Eq. (44-45)):

$$\frac{\partial C_{MI}}{\partial t} = -\nabla \cdot \left(-D_{ld} \nabla C_{MI} \right) = D_{ld} \nabla^2 C_{MI} \tag{46}$$

where, in this case, C_{MI} refers to the metal concentration inside the electrolyte solution, which in this study is considered to be 1M NaCl. The effective diffusion coefficient in the liquid can be obtained from the study reported in (Kuo & Landolt 1975), where rotating disk electrode experiments of iron dissolution in chloride solutions are described and the electromigration effect is taken in consideration empirically:

$$D_{ld} = 8.5 \cdot 10^{-10} \; m^2 / s \tag{47}$$

Motion within the solid

- The velocity of the fluid diffusing inside the pores of the metal is neglected and, therefore, the convection term in Eq. (44) is not considered.

- The effect of the electromigration term in Eq. (44) is included inside the diffusion coefficient, which is now called effective diffusion coefficient in the solid D_{sd} .

Therefore, the governing equation used to describe the motion of metal cations within the solid is given by the following modified version of the Nernst-Planck equation (vid. Eq. (44-45)):

$$\frac{\partial C_{MI}}{\partial t} = -\nabla \cdot \left(-D_{sd} \nabla C_{MI}\right) = D_{sd} \nabla^2 C_{MI} \tag{48}$$

Where, in this case, C_{MI} refers to the metal concentration inside the solid.

As shown in Eq. (48), the flux of metal cations is linearly proportional to the effective diffusivity. According to Faraday's laws of electrolysis, the amount of metal dissolution $\mathbf{N}_a$ in [mol/s] is linearly proportional to the anodic current density, which can be expressed as

$$i_a = n\mathrm{F}\mathbf{N}_a = n\mathrm{F}\frac{dM_{ol}}{dt} \tag{49}$$

where M_{ol} expressed in [mol] is the number of moles of the material. Therefore, in order to obey Faraday's laws of electrolysis, the effective diffusion coefficient in the solid is expressed as a function of the overpotential η as (Chen & Bobaru 2015)

$$D_{sd} = D_{sd}(\eta) = D_{sd}(0) e^{\frac{\alpha n \mathrm{F} \eta}{\mathrm{RT}}} \tag{50}$$

which resembles the expression of the anodic current density given in Eq. (42). In Eq. (50), the term $D_{sd}(0)$ represents the value of the diffusion coefficient in the solid when the overpotential is null, which is found through calibration against experimental polarisation data (the calibration procedure is explained later in this section). Eq. (50) can also be written as (Chen & Bobaru 2015)

$$\eta = \beta_a \cdot \log\left(\frac{D_{sd}(\eta)}{D_{sd}(0)}\right) \tag{51}$$

Moreover, the anodic current density in Eq. (49) can also be expressed as a function of the moving speed of the solid/liquid interface (i.e. the pit base) v_{int} [m/s] as

$$i_a = n\text{F}\mathbf{N}_a = n\text{F}C_{solid}v_{\text{int}} \tag{52}$$

where $\text{F} = 9.64859 \cdot 10^4\ \text{C/mol}$ and C_{solid} in [mol/m^3] is the concentration of metal cations in the solid. As described in (Scheiner & Hellmich 2009), in the case of stainless steel grade 304 (304 SS), i.e. the material considered in this study, C_{solid} can be calculated by considering the mass density of 304 SS and the molar masses of its main components Fe, Ni and Cr, which lead to:

$$C_{solid} = 143{,}000\ \text{mol/m}^3 \tag{53}$$

A similar approach can be used for the calculation of the valence number of 304 SS:

$$n = 2.19 \tag{54}$$

The corrosive solution considered in this study is 1M NaCl at temperature $T = 298.15\ \text{K}$ and the related saturation concentration value of dissolved stainless steel metal cations, C_{sat}, can be inferred from X-ray analysis (Isaacs et al. 1995):

$$C_{sat} = 5{,}100\ \text{mol/m}^3 \tag{55}$$

As described in (Chen & Bobaru 2015), the calibration procedure for the calculation of $D_{sd}(0)$ consists of the following steps:

1. A small initial value is chosen for the diffusion coefficient in the solid $D_{sd}(\eta)$ to make sure that corrosion will be in activation-controlled regime.

2. The simulation is launched and the velocity v_{int} of the solid/liquid interface (i.e. metal dissolution front) is recorded.

3. Eq. (52) is used to calculate the current density i_a.

4. Once i_a is known, it is possible to calculate the corresponding overpotential value by using the experimental polarization diagram reported in (Chen & Bobaru 2015).

5. Eq. (51) can now be used to calculate $D_{sd}(0)$ considering the following value of the Tafel constant: $\beta_a = 45.1\,\text{mV}$ (Chen & Bobaru 2015).

$D_{sd}(0) = 7.352 \cdot 10^{-17}\,\text{m}^2/\text{s}$ is the outcome of this calibration procedure, which is in agreement with (Chen & Bobaru 2015).

When the concentration of metal ions in the liquid reaches the saturation value C_{sat}, a salt film precipitates at the liquid/solid interface, which means that the concentration of metal ions in the liquid cannot be greater than the saturation value. Therefore, when the concentration value of the generic node is greater than C_{sat}, then the node is considered to be in solid phase. On the contrary, when the concentration value is smaller than C_{sat}, then the node is considered to be in liquid phase.

The peridynamic governing equation for metal dissolution can be written as

$$\dot{C}_{MI}(\mathbf{x},t) = \int_{H_{\mathbf{x}}} f_{\text{d}}\left(C_{MI}(\mathbf{x},t), C_{MI}(\mathbf{x}',t), \mathbf{x}', \mathbf{x}, t\right) \text{d}V_{\mathbf{x}'} \tag{56}$$

where $\dot{C}_{MI}(\mathbf{x},t)$ is the time derivative of metal ions concentration associated with the generic material point $\mathbf{x}$. In Eq. (56), the peridynamic function

$f_{\mathrm{d}}\left(C_{MI}\left(\mathbf{x},t\right),C_{MI}\left(\mathbf{x}',t\right),\mathbf{x}',\mathbf{x},t\right)$ is called metal dissolution response function and is defined as

$$f_{\mathrm{d}} = d_{MI}\,\frac{C_{MI}(\mathbf{x}',t)-C_{MI}(\mathbf{x},t)}{\left|\mathbf{x}'-\mathbf{x}\right|} \tag{57}$$

in which the peridynamic metal ions diffusion bond constant d_{MI} can be expressed in terms of the effective diffusion coefficient as (Chen & Bobaru 2015)

$$(1D)\quad d_{MI}=\frac{2\cdot D_{eff}}{A\cdot\delta^{2}} \qquad\qquad (2D)\quad d_{MI}=\frac{4\cdot D_{eff}}{\pi\cdot\delta^{2}\cdot h} \tag{58}$$

where h in [m] refers to the thickness of the body, A in [m^2] is the area of the 1D body and D_{eff} in [m^2/s] is the effective diffusion coefficient, which, for the 1D analysis, is calculated according to the concentration value of node "i", C_i, and node "j", C_j, (vid. Fig. 58) as

$$D_{eff}=\begin{cases} D_{sd} & \text{if } C_i > C_{sat} \text{ and } C_j > C_{sat} \\ D_{ld} & \text{if } C_i < C_{sat} \text{ and } C_j < C_{sat} \\ \dfrac{l_{ij}}{\dfrac{l_i}{D_{ld}}+\dfrac{l_j}{D_{sd}}} & \text{if } C_i \le C_{sat} \text{ and } C_j \ge C_{sat} \\ \dfrac{l_{ij}}{\dfrac{l_i}{D_{sd}}+\dfrac{l_j}{D_{ld}}} & \text{if } C_i \ge C_{sat} \text{ and } C_j \le C_{sat} \end{cases} \tag{59}$$

where l_i and l_j, both measured in [m], are the respective contributions of node "i" and node "j" to the total length of the bond l_{ij}.

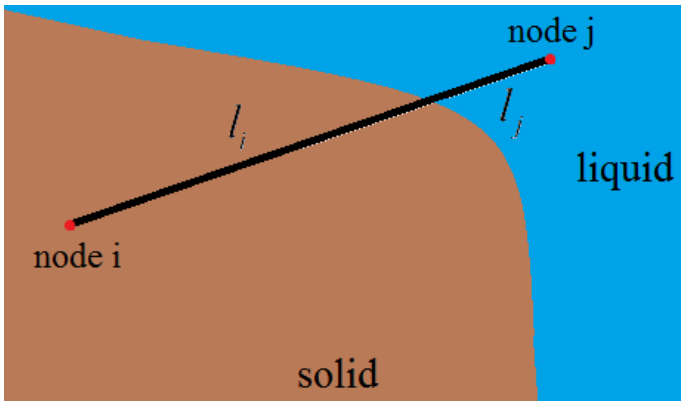

Fig. 58 PD bond connecting two generic nodes across the liquid/solid interface

In contrast, for the 2D analysis, since the evaluation of l_i and l_j can be computationally more expensive, the effective diffusion coefficient is calculated as suggested in (Chen & Bobaru 2015):

$$D_{eff} = \begin{cases} D_{sd} & \text{if } C_i > C_{sat} \text{ and } C_j > C_{sat} \\ D_{ld} & \text{if } C_i < C_{sat} \text{ and } C_j < C_{sat} \\ \dfrac{2 \cdot D_{sd} \cdot D_{ld}}{D_{sd} + D_{ld}} & \text{if } C_i \le C_{sat} \text{ and } C_j \ge C_{sat} \\ \dfrac{2 \cdot D_{sd} \cdot D_{ld}}{D_{sd} + D_{ld}} & \text{if } C_i \ge C_{sat} \text{ and } C_j \le C_{sat} \end{cases} \tag{60}$$

Similar to the PD model of SCC described in Chapter 5, the PD model of pitting corrosion consists of mechanical bonds overlapped by diffusion bonds. The former bonds are aimed to capture the subsurface mechanical damage reported in recent experimental studies (vid. Fig. 57). For this purpose, a damage index, $d(\mathbf{x},t)$, is defined for each node as

$$d(\mathbf{x},t) = \frac{N_f}{N_{tot}} \tag{61}$$

where N_f and N_{tot} are the number of failed bonds and the total number of bonds attached to the node at $\mathbf{x}$, respectively**.** At the beginning of the simulation, all the

nodes belonging to the solid body have a concentration value $C_{MI}(\mathbf{x},t)$ equal to C_{solid}, which means no corrosion. Therefore, in this condition, all the mechanical bonds connected to $\mathbf{x}$ are intact and its damage $d(\mathbf{x},t)$ index is null. On the contrary, when $C_{MI}(\mathbf{x},t)$ becomes smaller than C_{liquid}, the node at $\mathbf{x}$ changes its phase from solid to liquid, which means complete metal dissolution. Therefore, in this condition, all the mechanical bonds connected to $\mathbf{x}$ are broken and the damage index has a unit value. As suggested in (Chen & Bobaru 2015), the damage index $d(\mathbf{x},t)$ can therefore be written as a function of the nodal concentration $C_{MI}(\mathbf{x},t)$ as

$$d(\mathbf{x},t) = \frac{C_{solid} - C_{MI}(\mathbf{x},t)}{C_{solid} - C_{sat}} \tag{62}$$

Each bond has a certain probability P_r to be broken in the current time step. In each time step, P_r can be calculated as (Chen & Bobaru 2015)

$$P_r = \frac{1}{1-d_{t-1}} \cdot \left(\frac{\Delta C_i}{C_{solid} - C_{sat}} \right) \tag{63}$$

where d_{t-1} represents the value of the damage index at the previous time step, and ΔC_i is the difference in nodal concentration between the previous time step and the current time step. Once P_r is calculated, a random number in the range [0,1] is generated for each bond. If the random number is smaller than P_r, then the mechanical bond is broken and the value of the damage index is updated.

6.4 Implementation via ANSYS

Eqs. (45,47) can be solved by using either explicit or implicit time integration schemes. The advantage of an implicit time integration scheme is the numerical stability of the method regardless of the value of the time step size. This is particularly important when modelling corrosion, since the timescale of the problem can range from seconds to years. In this study, a novel approach, based on the

analogy between heat transfer and metal ions diffusion, is used to exploit the implicit solver implemented in the commercial FEA software ANSYS 14.5.

Thus, the PD model of pitting corrosion described in the previous section is represented by the following thermal finite elements available in ANSYS:

- MASS 71. Thermal mass elements used to represent the PD particles. The only degree of freedom is the temperature, which, in our model, represents the metal ions concentration [mol/m^3].

- COMBIN 14. Thermal spring elements that represent the PD bonds. These elements are used to connect the thermal mass elements to each other. Like for the MASS 71 elements, the only degree of freedom is the temperature.

The expression for the real constant d_{ANSYS} of the generic COMBIN 14 element can be written as

$$(1D)\quad d_{ANSYS} = \frac{d_{MI} \cdot s_{cf} \cdot V \cdot v_c \cdot V}{l} \qquad (2D)\quad d_{ANSYS} = \frac{d_{MI} \cdot s_{cf} \cdot V \cdot v_c \cdot V}{l^2} \qquad (64)$$

where l in [m] represents the length of the bond. This approach, implemented via ANSYS, is used for carrying out all the simulations described in Section 6.5.

6.5 Numerical results and validation

6.5.1 Pitting corrosion in a stainless steel bar

Similar to the case described in the experimental study reported in (Gaudet et al. 1986) and in the numerical study reported in (Chen & Bobaru 2015), a one-dimensional pencil electrode made of austenitic stainless steel grade 304 is considered. The electrode is subjected to different values of overpotential and is coated everywhere except at its left surface, which is exposed to a 1M NaCl aqueous solution (Fig. 59). The material data can be found in Section 6.3. The pencil

electrode is discretised with 8000 PD nodes and the resulting value of grid spacing and horizon's radius are $\Delta = 0.0125\,\mu m$ and $\delta = 0.0502\,\mu m$, respectively. At the beginning of the simulation, all the nodes belonging to the pencil electrode have a concentration of metal ions equal to C_{solid}, the liquid/solid interface is at x = 0 and the concentration of metal ions inside the corrosive solution is assumed to be null. In time, the solid/liquid interface moves from left to right as the pencil electrode dissolves and the concentration of metal ions inside the solution increases from zero up to the value of C_{sat}. The length of the one-dimensional pencil electrode is 100 μm and its surface area is $1.5625 \cdot 10^{-4}\,\mu m^2$. The left extremity of the bar is subjected to the following boundary condition: $C(0,t) = 0$. In contrast, all the other surfaces of the pencil electrode are insulated, i.e. $\frac{\partial C(x,t)}{\partial t} = 0$.

Fig. 59 Pencil electrode configuration

Six different values of overpotential η are considered in this study. The corresponding values of $D_{sd}(\eta)$ are reported in Table 3 and can be found by using Eq. (51).

Table 3 Values of overpotential and corresponding effective diffusion coefficient in the solid

η [V]	$D_{sd}(\eta)$ [m^2/s]
0.065	$2.03087 \cdot 10^{-15}$
0.08	$4.36793 \cdot 10^{-15}$
0.095	$9.39443 \cdot 10^{-15}$
0.137	$8.01926 \cdot 10^{-14}$
0.18	$1.08381 \cdot 10^{-12}$
0.2	$2.0 \cdot 10^{-12}$

The most suitable time step size dt is found performing a convergence analysis for each of the six simulations carried out in this study. As shown in Figs. 60-61, the lower the overpotential, the lesser stringent the requirement on the minimum time step size.

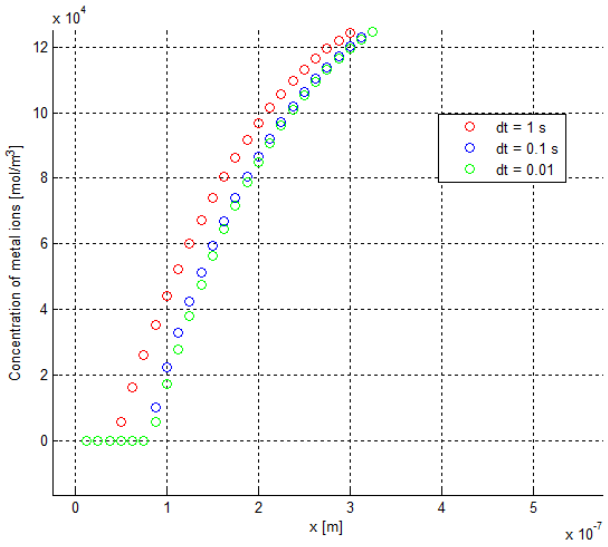

Fig. 60 Time step convergence analysis for the simulation with $\eta = 0.065\ \mathrm{V}$ at time = 10 s

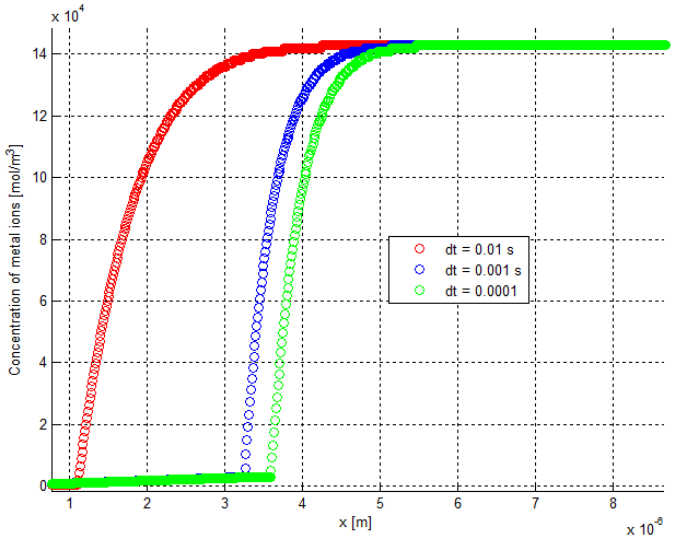

Fig. 61 Time step size convergence analysis for the simulation with $\eta = 0.2\ \mathrm{V}$ at time = 0.5 s

In fact, when $\eta = 0.065\ \mathrm{V}$, $dt = 0.1$ s can be considered a reasonable value for the time step (vid. Fig. 60). In contrast, when $\eta = 0.2\ \mathrm{V}$, a time step size at least 100 times smaller is necessary (vid. Fig. 61). Therefore, the values of time step size used

in this study range from 0.001 s up to 0.1 s depending on the outcome of convergence analysis.

Fig. 62 shows the results of the present numerical model for the simulation with $\eta = 0.2\ \mathrm{V}$. As mentioned before, the location of the liquid/solid interface is x = 0 at the beginning of the simulation. During the simulation, the interface moves from left to right and its location is calculated as the average of the x-coordinate of the two nodes whose concentration value is just above and just below C_{sat}. For example, the position of the interface is x = 15 μm at time = 5 s (yellow curve) (vid. Fig. 62).

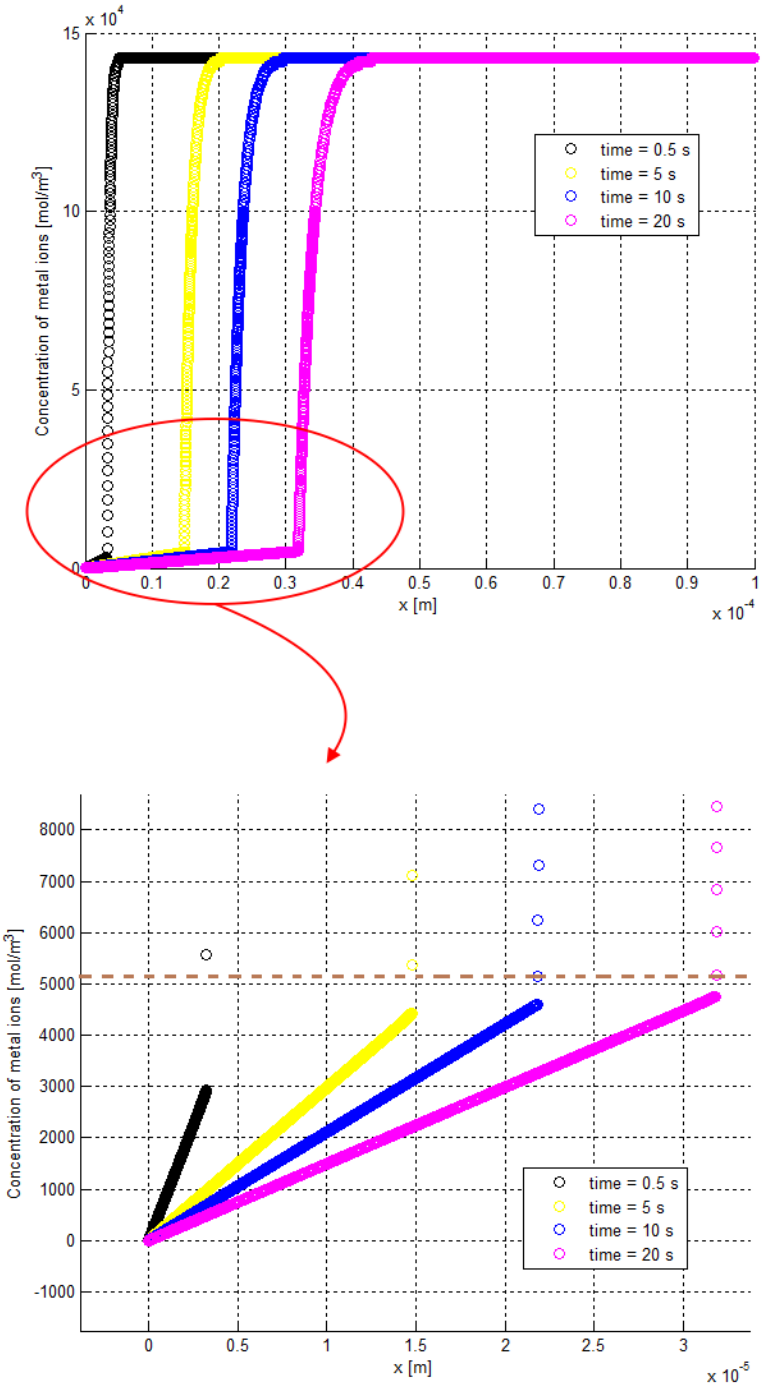

Fig. 62 Concentration field [mol/m^3] within the bar for η = 0.2 V at four different times: time = 0.5 s (black circles), time = 5 s (yellow circles), time = 10 s (blue circles) and time = 20 s (purple circles)

As can be seen in the lower image in Fig. 62, the corrosion regime becomes diffusion-controlled only after time = 20 s, which means that the concentration of metal ions has reached the value of C_{sat} and, as a result, a salt film is expected to precipitate at the liquid/solid interface. The results shown in Fig. 62 are in agreement with the numerical results reported in (Chen & Bobaru 2015) (vid. Fig. 63).

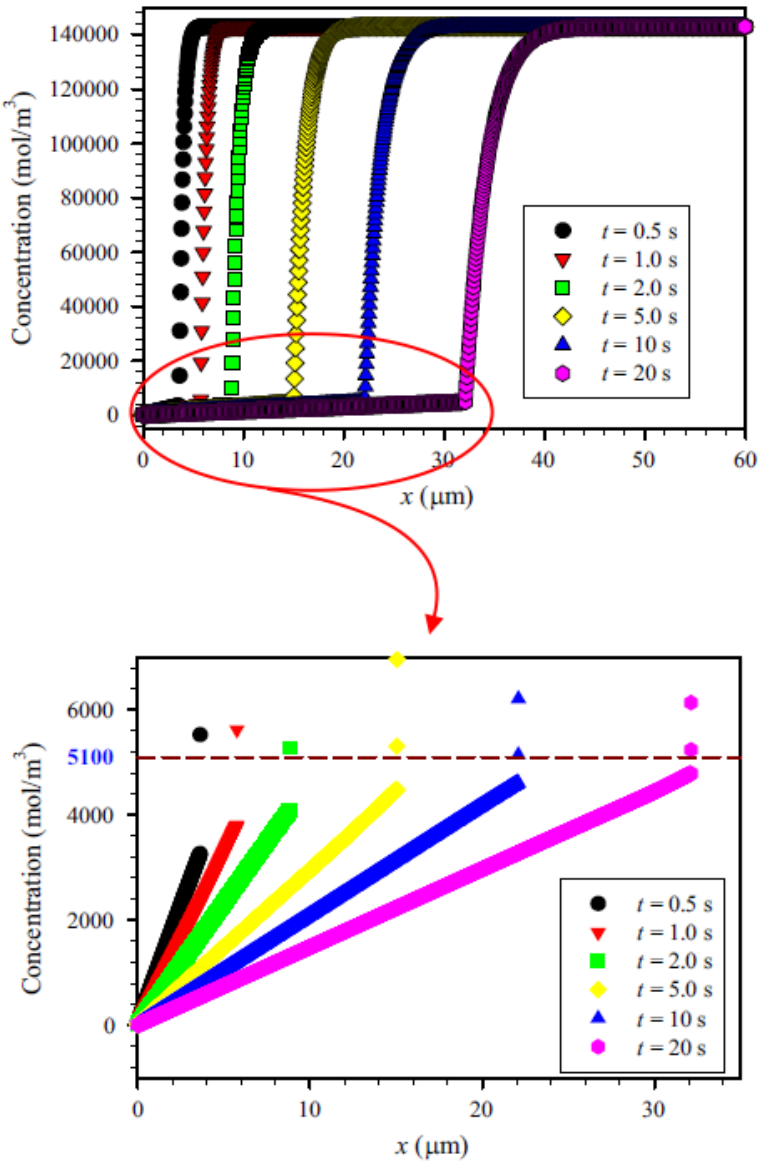

Fig. 63 Numerical results published in (Chen & Bobaru 2015) for the simulation with $\eta = 0.2$ V

As previously mentioned, the lower the value of the applied overpotential, the longer the duration of the activation-controlled regime, which means that the salt film will precipitate later in time. In fact, for instance, if the simulation with $\eta = 0.095\ \text{V}$ is considered, when time = 20 s the metal ions concentration inside the solution is much smaller than C_{sat} (vid Fig. 64), which is in contrast with the simulation where $\eta = 0.2\ \text{V}$ (vid. Fig. 62). This is because a smaller overpotential means a smaller effective diffusive coefficient in the solid D_{sd} (vid. Eq. (51)).

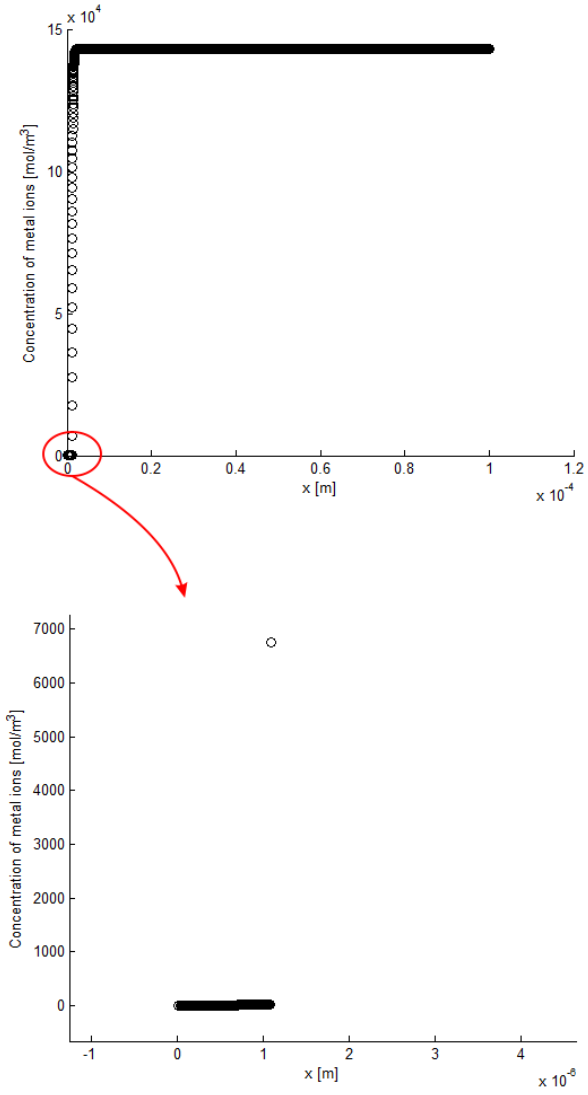

Fig. 64 Concentration field [mol/m^3] within the bar for η = 0.095 V at time = 20 s

As previously mentioned, the current PD model of pitting corrosion is able to capture subsurface damage as well. In this regard, the damage field within the bar, calculated as described in Section 6.3, is found to be in good agreement with the numerical analysis reported in (Chen & Bobaru 2015) (vid. Fig. 65).

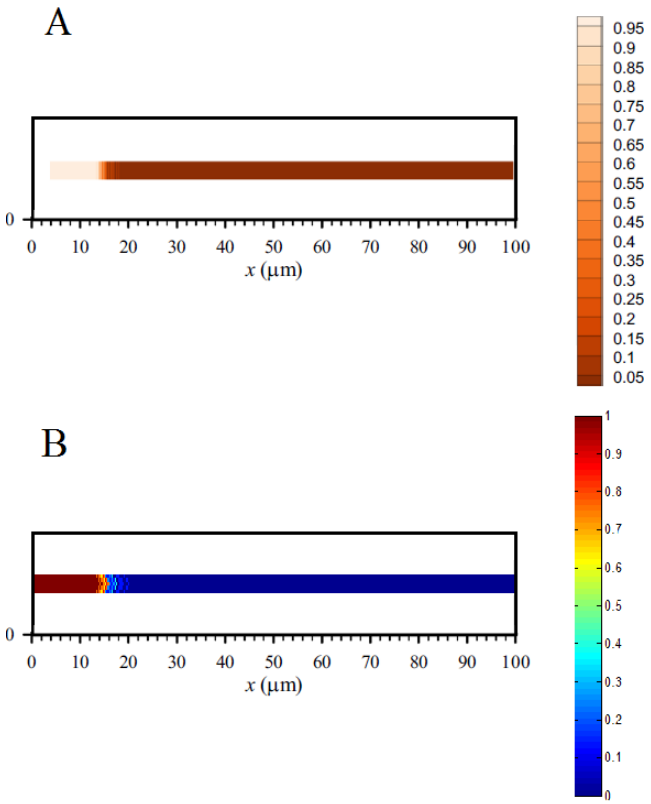

Fig. 65 Value of the damage index within the bar at time = 5 s for the simulation with η = 0.2 V: other numerical model (A) and present numerical model (B)

At the end of each simulation, the position of the liquid/solid interface is used to calculate the velocity v_{int}. Then, the anodic current density is calculated by using Eq. (52). The values of the current density for all six simulations are shown in Fig. 66, along with the comparison against experimental data (Gaudet et al. 1986) and other numerical data (Chen & Bobaru 2015).

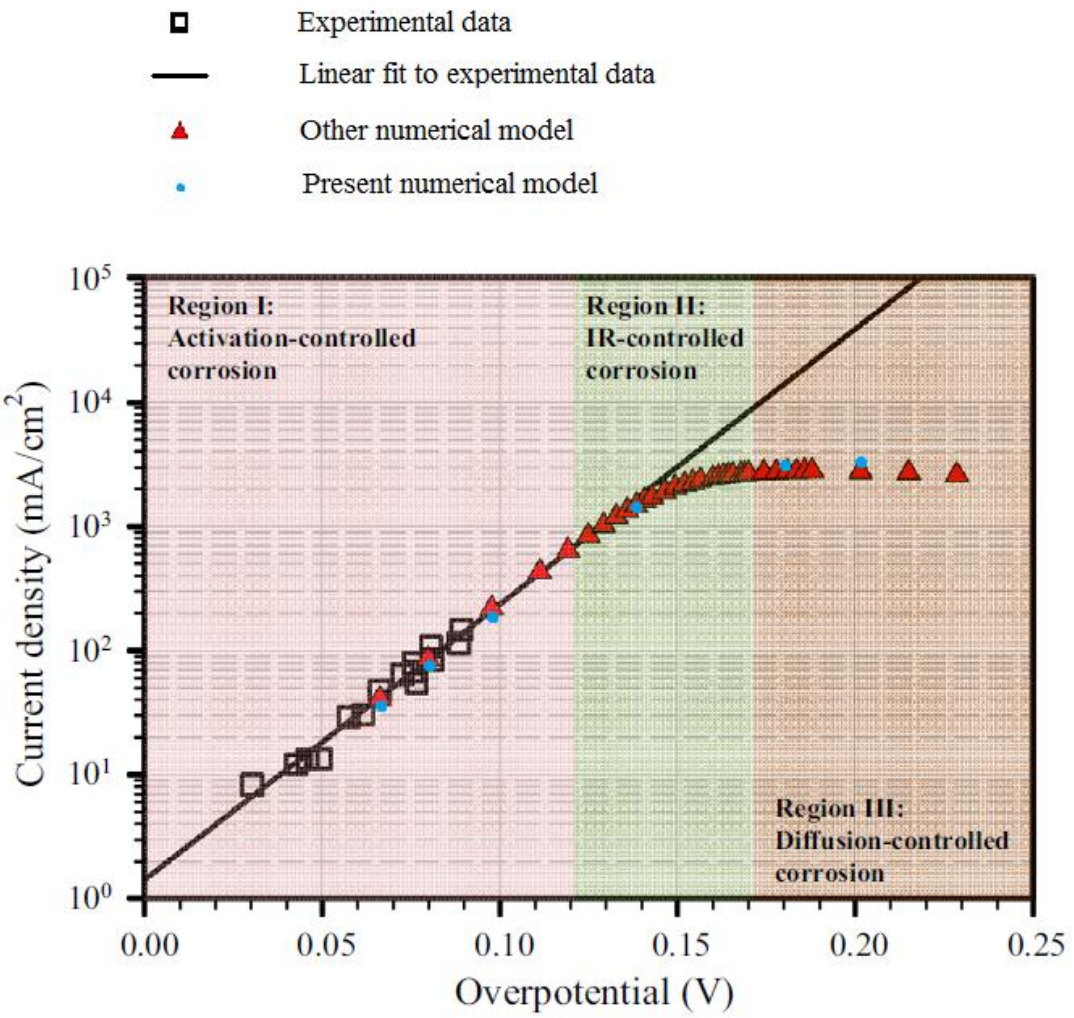

Figure 66 Anodic current density [mA/cm^2] vs. overpotential [V]: experimental data (black squares), linear fit to experimental data (solid line), other numerical model (red triangles) and present numerical model (blue points). Modified from (Chen & Bobaru 2015)

6.5.2 Pitting corrosion in a stainless steel plate

Similar to (Chen & Bobaru 2015), the 2D model of pitting corrosion considered in this study is represented by a plate of dimensions 0.1 mm x 0.1 mm and thickness 1 μm. As shown in Fig. 67, the top edge of the plate is damaged and the initial pit is filled with 1M NaCl aqueous solution, in which the concentration of metal ions is initially null. The volume occupied by the solution is assumed to be much larger than that of the metal, i.e. austenitic stainless steel grade 304. This assumption

allows to represent the bulk of the corrosive solution with a zero-concentration boundary condition throughout the simulation.

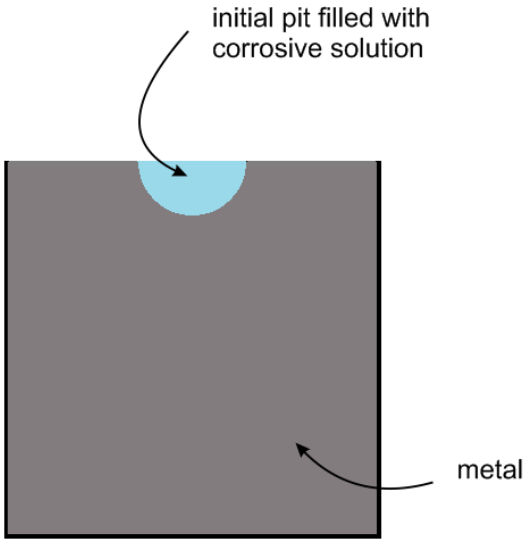

Fig. 67 2D pitting corrosion model: initial pit (blue colour) and metal (grey colour)

The material properties are the same as those used for the 1D analysis (vid. Section 6.3) and the radius of the initial pit is 10 μm. The plate is discretised with 100 x 100 PD nodes and the resulting value of grid spacing and horizon's radius are $\Delta = 1\,\mu\text{m}$ and $\delta = 4\,\mu\text{m}$, respectively. At the beginning of the simulation, all the nodes belonging to the metal have a concentration of metal ions equal to C_{solid}. Similar to the 1D study, the appropriate time step size is found by performing a convergence analysis. As shown in Fig. 68, a time step of 0.5 s can be considered a suitable value. The results obtained by using the present model are in qualitative agreement with the numerical results presented in (Chen & Bobaru 2015), where a time step of 0.05 s is used (vid. Fig. 69).

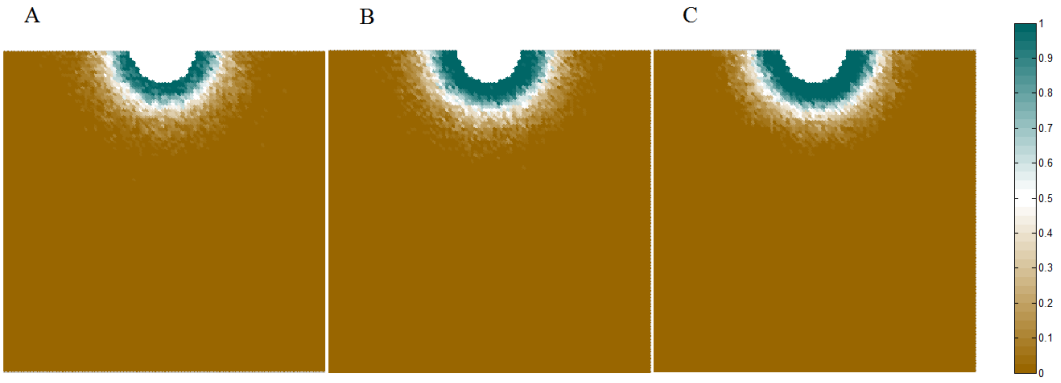

Fig. 68 Time step size convergence analysis for the damage index map at time = 20 s and η = 0.2 V: dt = 5 s (A), dt = 0.5 s (B), dt = 0.05 s (C)

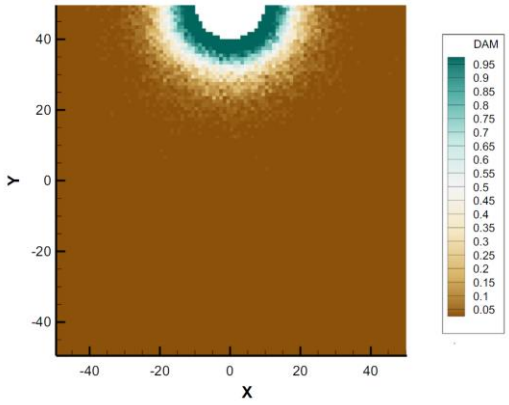

Fig. 69 Damage index map at time = 20 s for the case with η = 0.2 V: results reported in (Chen & Bobaru 2015)

In Figs. 68-69, only the particles in solid phase are showed. The liquid/solid interface does not advance within the first 20 s, but a layer constituted by solid particles with damage index value equal to one is formed at the interface. As explained earlier, if a generic particle has a damage index value equal to one, it means that all its bonds have been broken. Thus, in this case, the particle is totally disconnected from the rest of the body and, therefore, the solution can penetrate underneath. In order to mimic this phenomenon, the approach used in (Chen & Bobaru 2015) is adopted. It consists in adding the following condition to the previous model: the phase of the node is changed from solid to liquid when $d = 1$

even if $C > C_{sat}$. As shown in Fig. 70, the results produced by the present model are in quantitative agreement with the study reported in (Chen & Bobaru 2015).

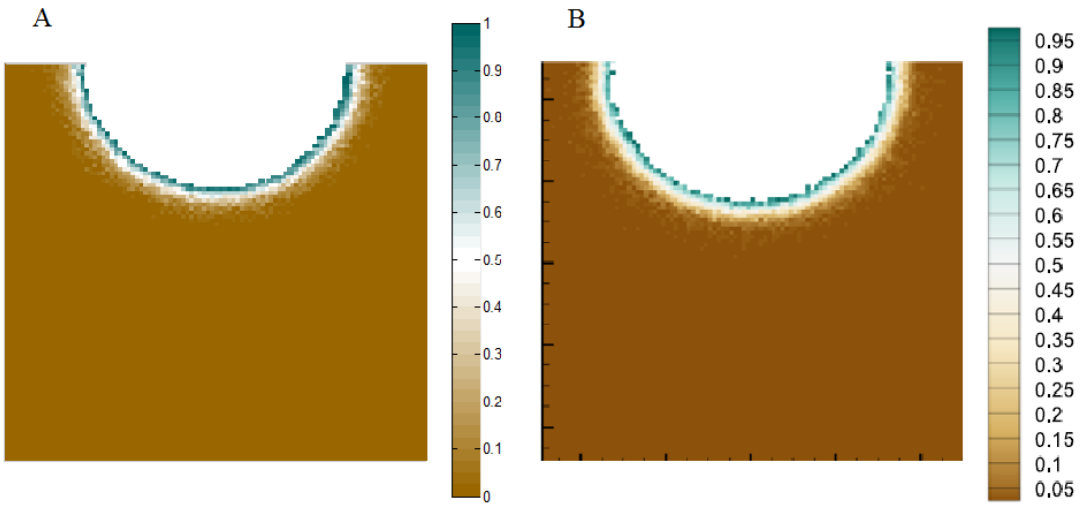

Fig. 70 Damage index map at time = 20 s for the case with η = 0.2 V: present numerical model (A) and other numerical model (B)

6.5.3 Realistic pit morphologies

In reality, corrosion pits can have complex geometries, which are often very different from the simple cases considered so far. Therefore, the aim of this section is to describe how the PD model of pitting corrosion can be extended to model realistic pit morphologies. There may be several different approaches that can be used in this regard. The procedure adopted in this study, which is used during the preparation of the model, consists of the following two steps:

1. Selection of the region of the domain where the pit is expected to propagate.

2. For all the nodes that do not belong to this region, an artificial effective coefficient of diffusion in the metal D_{sd}^{*} is used. The ratio between D_{sd}^{*} and D_{sd} is always smaller than 1 and is called "coefficient of pit morphology" c_{pm}:

$$c_{pm} = \frac{D_{sd}^{*}}{D_{sd}} < 1 \tag{65}$$

The following boundary condition is applied to the blue region of length 6 μm in Fig. 71: $C(x,t) = 0$.

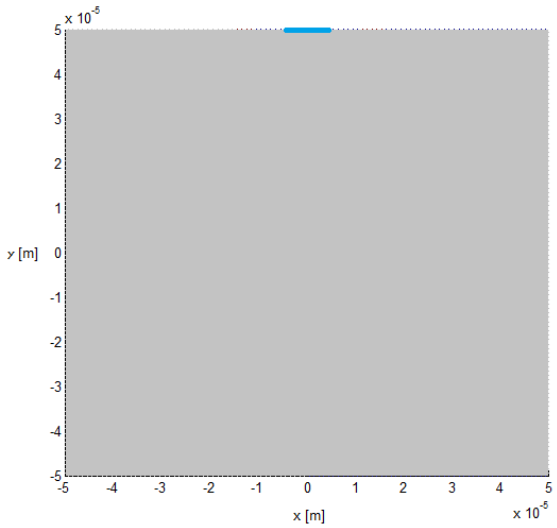

Fig. 71 PD model for the prediction of realistic pit morphologies: metal (grey colour) and initial liquid/solid interface (blue colour)

As shown in Fig. 72, if the morphology of the pit is known a priori, then the PD model is able to reproduce the expected shape of the pit cavity. The material properties and numerical parameters used for the simulations in Fig. 72 are the same as those used in Section 6.5.2. The only difference is the introduction of c_{pm}, which is assumed to be 1%.

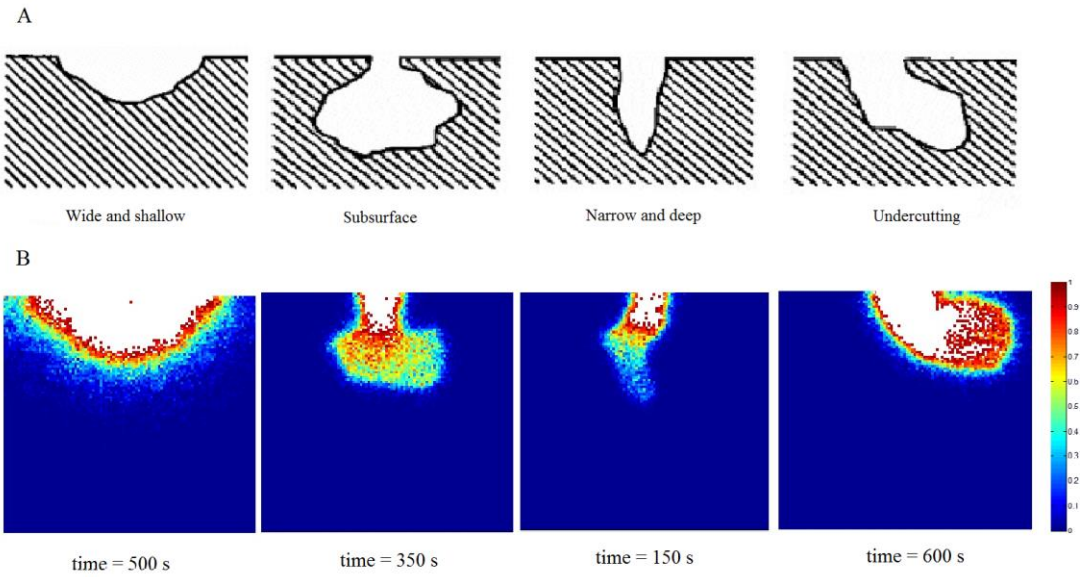

Fig. 72 Realistic pit morphologies (Hoeppner 2011) (A), damage index map obtained with the present numerical model (B)

6.5.4 Pitting corrosion in a cluster of cathodic intermetallic particles

It is well-known that the metallurgical characteristics of the material can affect the evolution of corrosion pits. In this analysis, pitting propagation in a cluster of cathodic intermetallic particles (IMPs) is investigated. The material properties and numerical parameters are the same as those used in Sections 6.5.2 and 6.5.3. IMPs are created through node selection during the generation of the model, and they are represented by the application of the following boundary condition to all those nodes that belong to the IMPs domain: $C(x,t) = C_{solid}$.

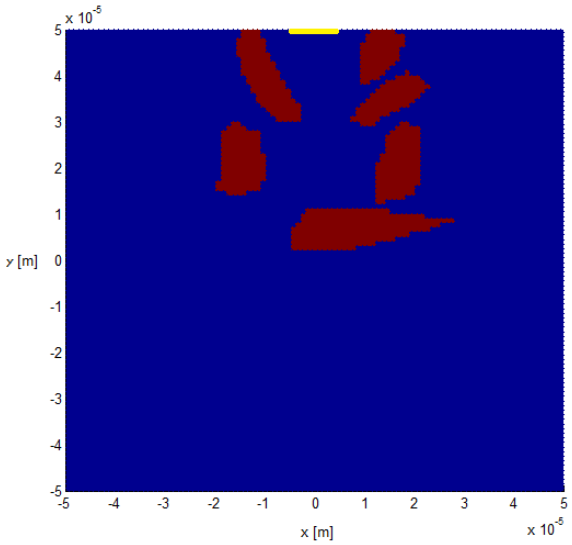

Fig. 73 PD model of pitting corrosion in a cluster of IMPs: metal (blue colour), corrosive solution (yellow colour) and IMPs (red colour)

Like for the analyses described in Sections 6.5.2 and 6.5.3, the following boundary condition is applied to the yellow region of length 6 μm in Fig. 73: $C(x,t)=0$. As shown in Fig. 74, pit damage is channelled by the cluster of IMPs and the lower part of the plate is partially shielded by the IMP at the bottom of the cluster. In order to better visualise the pit cavity, only solid nodes are shown in Fig. 74.

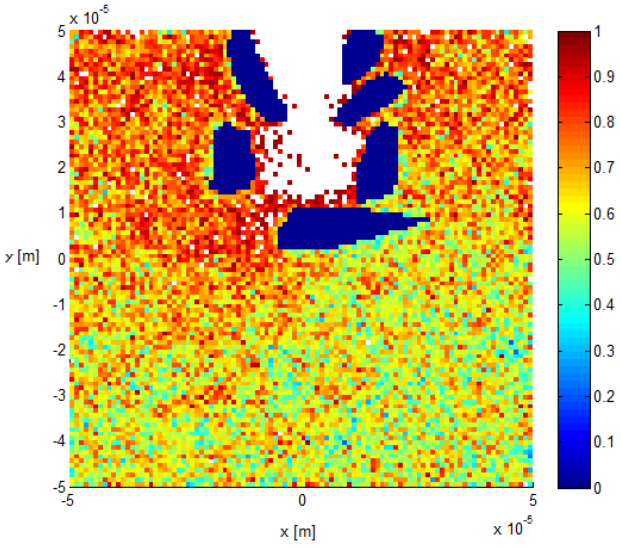

Fig. 74 Pit evolution in a cluster of IMPs. Damage index map at time = 2500 s: no dissolution (blue colour) and close to dissolution (red colour)

6.6 Gap and future work

The list here below summarises the main gaps and limitations of the study described in this chapter:

- The present model considers a metal that, at the beginning of the analysis, is already exposed to a corrosive solution. Therefore mechanisms of passive film degradation and possible repassivation are not considered. This limit the applicability of the model, which, however, can be used to predict corrosion rates once field monitoring techniques and inspections have revealed damage in the coating or passive film, which lead to the exposure of the underneath metal to the corrosive solution.

- The model is validated against experimental data in activation-controlled regime and other numerical results in both activation-controlled and diffusion-controlled regimes. However, it lacks experimental validation in the diffusion-controlled regime. This task could not be achieved due to the lack of experimental data.

- The current PD model for the prediction of realistic pit morphologies requires an artificial procedure of sub-domain selection during the preparation of the model (vid. Section 6.5.3). Therefore, the model is guided to produce the expected pit morphology. This can be good enough for failure analyses and microstructural design of new materials. However, the model has to become fully autonomous before it can be used as an effective predictive tool of pitting corrosion damage.

- The model can be extended to include the effect of other microstructural features of the material apart from IMPs, e.g. the effect of grain boundaries.

- Methods such as electron backscatter diffraction (Pouillier et al., 2012) can be used in conjunction with the present PD model with the aim to reproduce

an equivalent polycrystalline model, e.g. grain boundaries, grain orientation and IMPs, instead of producing a random microstructure.

- The model should be tested with other materials and environments.
- Extension of the 2D model to 3D.
- Optimisation and parallelisation of the existing serial codes in order to reduce the computational cost of the simulations.

6.7 Summary

Pitting is a localised form of corrosion that leads to the formation of corrosion cavities or pits due to the breakage of the material's passive film. Pitting corrosion negatively affects several industries and structures, and is the most common, dangerous and destructive type of corrosion in marine and offshore structures. Due to material inhomogeneities, pits can evolve in very different shapes. Despite the significant improvements in the understanding of pitting corrosion, many aspects of this phenomenon remain unclear, corrosion rate prediction based on experimental data remains difficult and experimental measurements of corrosion rates under different electrochemical conditions can be complex and time consuming. In order to overcome some of these limitations, numerical approaches can be a valuable complement. However, due to the fact that the majority of corrosion deterministic models currently available only consider diffusion within the electrolyte solution, none of these models have been able to predict corrosion subsurface damage, which is a phenomenon documented in the experimental literature.

In this chapter, a PD framework for the modelling of pitting corrosion and subsurface damage in austenitic stainless steel grade 304 exposed to 1M NaCl aqueous solution is described. Metal dissolution is predicted by using a modified Nernst-Planck equation where the coupled effect of diffusion and electromigration is taken into account through an effective diffusion coefficient. Different values of

overpotential are applied to the metal and corrosion rate and current density in both activation-controlled and diffusion-controlled corrosion regimes are predicted. The results of 1D and 2D analyses are found to be in good agreement with experimental data and other numerical results. A procedure for enabling the model to reproduce realistic pit morphologies and metal dissolution in a cluster of IMPs has been described. The use of the implicit time integration scheme implemented in ANSYS has allowed for the use of a greater time step size, which, in turn, led to a significant reduction of the total computational cost of the simulations. The PD model of pitting corrosion here presented can be used for microstructural design of new materials and failure analysis, but significant improvements are needed before it can be used as an effective predictive tool of pitting corrosion damage. This framework is used as a starting point for the creation of the PD model of pit-to-crack transition described in Chapter 7.

7 Pit-to-crack transition

7.1 Introduction

In this chapter, a PD framework for the modelling of pit-to-crack transition is presented. The couple material/environment considered in this study is austenitic stainless steel grade 304 exposed to 1M NaCl aqueous solution. The analysis is constituted by two phases: 1) pitting evolution and 2) crack propagation. In other words, at the beginning of the simulation, no mechanical load is applied to the body, and only metal dissolution is predicted (first phase). Once the corrosion pit has penetrated inside the body of the metal, a tensile load is applied to the structure and the resulting pit-to-crack transition is observed (second phase). Then, the results are compared against those obtained by considering different pit morphologies. Pitting corrosion is predicted by using the PD pitting corrosion model described in Chapter 6, while the PD micro-mechanical model described in Chapter 4 is used to predict intergranular crack propagation. Therefore, the present model is created by coupling the two PD models above mentioned. Apart from the already discussed advantages of these two models, an additional benefit of such an approach is the possibility to remove the assumption that the pit-to-crack transition has to occur at the pit base (vid. Section 7.2). To the best of the author's knowledge, no PD model of pit-to-crack transition is currently available in the literature. Therefore, the numerical model described in this chapter is the first of its kind (De Meo & Oterkus 2016). This chapter is organised as follows: Section 7.2 provides the background and motivation for this study. The PD model of pit-to-crack transition is explained in Section 7.3, while numerical results can be found in Section 7.4. Gap and future work are discussed in Section 7.5, while the summary of Chapter 7 is provided in Section 7.6.

7.2 Background and motivation for research

It is well-known that high stress regions around corrosion pits can lead to crack nucleation and propagation (Pidaparti & Patel 2011). In fact, in many engineering applications, corrosion pits act as precursor to cracking, but prediction of structural damage has been hindered by lack of understanding of the process by which a crack develops from a pit and limitations in visualisation and measurement techniques (Turnbull 2014). As argued in (Pidaparti & Patel 2010), an experimental approach able to accurately quantify the stress and strain field around corrosion pits is still lacking. In all those engineering applications where inspection and maintenance are burdensome, such as in the deep water oil and gas industry, the damage tolerance approach, widely used in the aerospace industry, is not an option. Therefore, understanding the process of pit-to-crack transition and assessing the probability of those pits transforming to cracks is paramount (Turnbull 2014). For long cracks, standards for quantifying environment-assisted crack growth rates can be found. However, in relation to the growth rate of small cracks emerging from corrosion pits, there are no standards to guide the measurement process (Turnbull 2014). In this regard, numerical modelling can be helpful. Several numerical models, usually based on FEM, are available for predicting the evolution of long cracks. However, the methodology for dealing with the nucleation of damage is less well developed (Turnbull et al. 2006a), and, often, numerical instabilities arise during the simulation of crack propagation. Moreover, the popular assumption that the crack has the same depth as the pit at the point of transition and by implication initiates at the pit base, has no intrinsic foundation (Turnbull 2014). In fact, novel observations using X-ray tomography of stress-corrosion cracks emerging from pits (Turnbull et al. 2010), showed that cracks evolved from the pit predominantly at or near the pit mouth and not at the pit base. Moreover, recent FEM analysis of pits in specimens subjected to different static loads revealed that maximum stress and strain can occur at the pit shoulder and in proximity to the pit mouth (Zhu et al. 2013). The numerical approach described in this chapter can model nucleation and propagation of cracks

without being affected by any numerical instability (vid. Chapter 3), and does not need to assume crack initiation from the base of the pit.

7.3 PD model of pit-to-crack transition

As mentioned earlier, the PD analysis for pit-to-crack transition is constituted by two phases: 1) pitting evolution and 2) crack propagation. Concerning the first phase, the PD model of pitting corrosion described in Chapter 6 is used. In contrast, crack propagation is predicted by using the PD micro-mechanical model described in Chapter 4. The analysis can be summarised by the following steps:

1. Metal dissolution is predicted by using the PD model of pitting corrosion implemented in ANSYS. At the end of the simulation, a file is produced with a list of all the bonds that have been broken due to corrosion damage. This is the end of the first phase (Fig. 75 A).

2. At the beginning of the second phase, the PD micro-mechanical model is generated as described in Chapter 4, and the file containing the information of the broken bonds produced during the first phase of the pit-to-crack transition analysis is read by ANSYS.

3. All the bonds listed in the above mentioned file are killed by using the ANSYS command EKILL. Therefore, once the mechanical load is applied to the structure (vid. Fig. 75 B), these bonds will not contribute to the mechanical response of the structure.

4. The mechanical load is applied to the damaged structure as shown in Fig. 75 B, the simulation is launched and the results about the mechanical response of the structure are collected. This is the end of the second phase of the analysis.

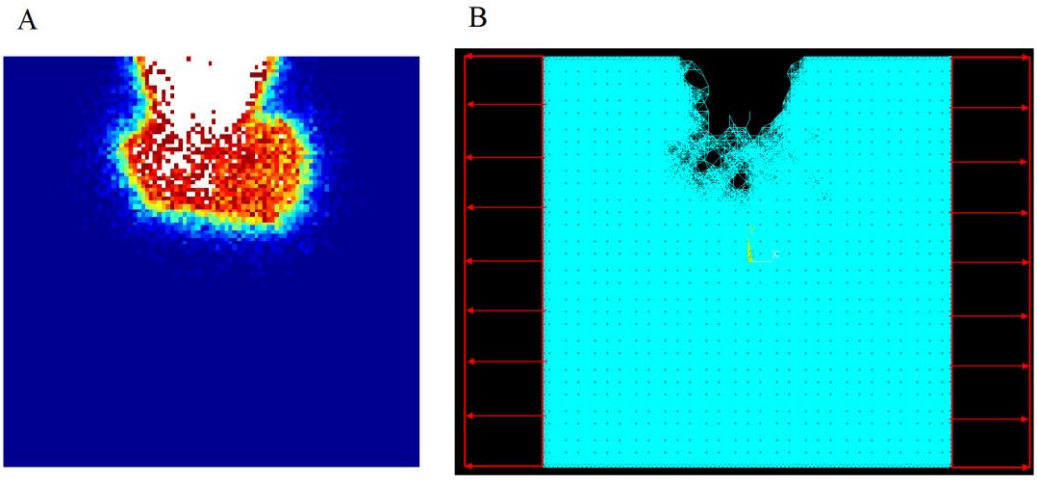

Fig. 75 The two phases of the pit-to-crack transition model for the case of subsurface pit: damage index map produced at the end of the first phase of the analysis (A), corrosion damage and mechanical boundary condition applied to the body at the beginning of the second phase of the analysis (B)

7.4 Numerical results

Similar to the 2D model of pitting corrosion presented in Section 6.5.3 (i.e. realistic pit morphologies), the PD model of pit-to-crack transition considered in this study for the first phase of the analysis (i.e. pitting evolution) is represented by a plate of dimensions 0.1 mm x 0.1 mm and thickness 1 μm. The following boundary condition is applied to the blue region of length 6 μm in Fig. 76: $C(x,t)=0$.

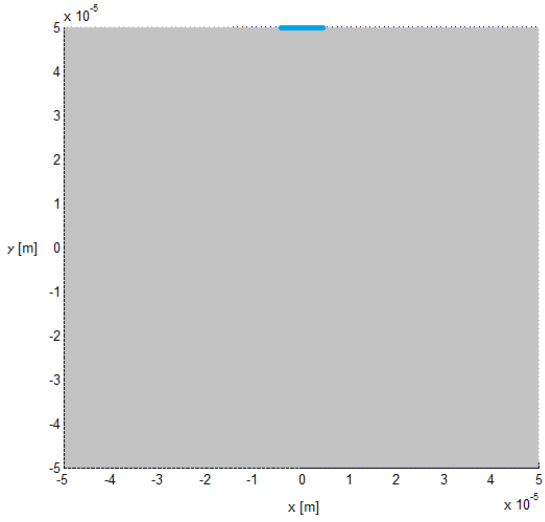

Fig. 76 Model for the first phase of the pit-to-crack transition analysis: metal (grey colour) and corrosive solution (blue colour)

The environment and material properties are the same as those used for the 1D pitting corrosion analysis of austenitic stainless steel grade 304 exposed to 1M NaCl aqueous solution described in Chapter 6 (vid. Section 6.3). The plate is discretised with 100 x 100 PD nodes and the resulting value of grid spacing and horizon radius are $\Delta = 1\,\mu\text{m}$ and $\delta = 3\,\mu\text{m}$, respectively. At the beginning of the simulation, all the nodes belonging to the metal have a concentration of metal ions equal to C_{solid}. Three different pit morphologies, i.e. wide and shallow pit, subsurface pit and undercutting pit, and one value of applied overpotential, i.e. η = 0.2 V, are considered.

Concerning the second phase of the analysis, i.e. crack propagation, the microstructure of the material is constituted of 50 randomly oriented crystals, which are generated as described in Section 4.3, and the following values of Young's modulus, density and fracture toughness of the material are considered: $E = 200\,\text{GPa}$, $\rho = 7880\,\text{Kg}/\text{m}^3$ and $K_{Ic} = 70\,\text{MPa}\sqrt{\text{m}}$, respectively. A horizontal velocity boundary condition of 0.2 m/s is applied along the left and right edges of the plate as shown in Fig. 75. Moreover, the vertical displacement of the nodes in

this region is constrained along the vertical direction. The time step size has to be small enough to capture the full dynamic characteristic of the problem. In this case, a time step $dt = 0.5$ μs seemed appropriate. Similar to the SCC model described in Chapter 5, only the bonds crossing the grain boundary of the material are allowed to break, therefore modelling intergranular fracturing only.

The first pit morphology considered in this study is the wide and shallow pit. As shown in Fig. 77, the grain boundaries of the material are coloured in white. It may appear that the material is internally fractured even at time = 0 s, but this is not true. Fig. 77 is generated at the end of the simulation, when material has already undergone fracturing and some of the bonds have been killed by using the ANSYS command EKILL. In Fig. 77 only the final alive elements are plotted; this is the reason why the plate appears internally fractured at the beginning of the simulation. This is valid also for the result concerning other pit morphologies, i.e. Figs. 78,80. As shown in Fig. 77, pit-to-crack transition occurs around time = 10 μs at approximately the pit base. At this time it is also possible to notice the vertical contraction of the plate caused by horizontal opening load and the Poisson's effect. As time goes by, the crack continues to propagate along the grain boundaries of the material. Around time = 13.5 μs, a secondary crack nucleates in proximity to the lower right edge of the plate, which is probably due to the vertical contraction of the material and the vertical displacement constraint applied along the right edge of the plate. This does not occur at the lower left edge of the plate probably because the closest grain boundary to the lower left edge is farther than that at the lower right edge of the plate.

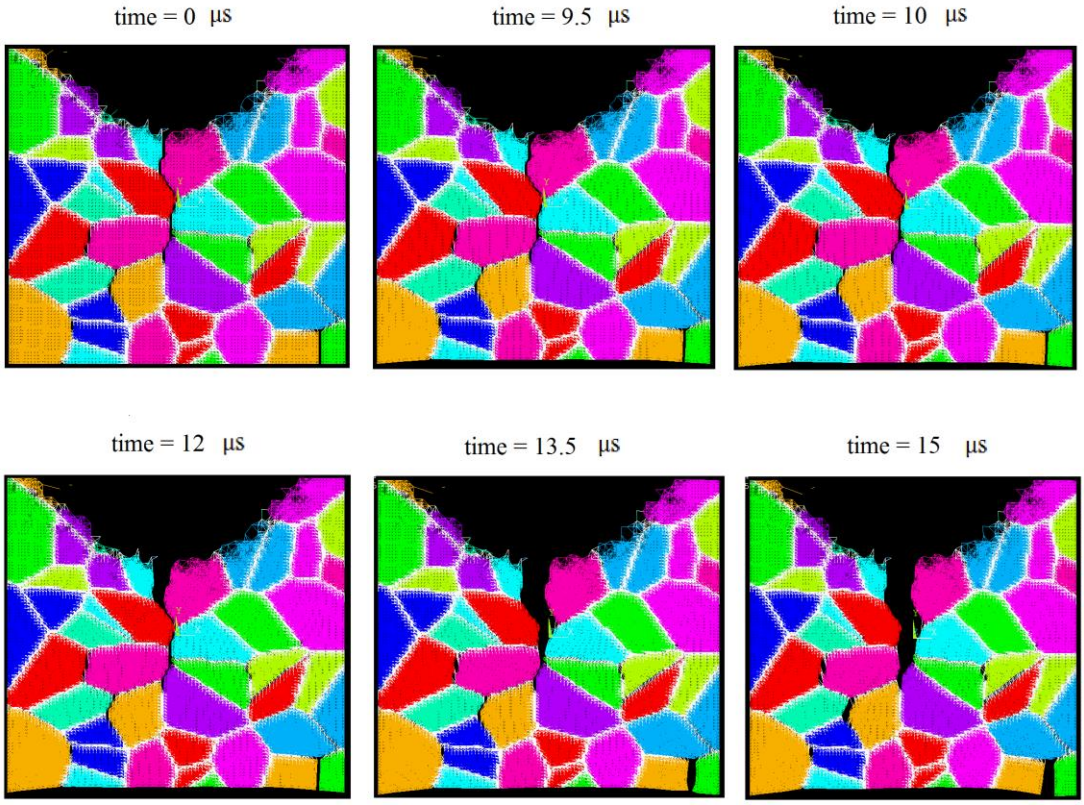

Fig. 77 Pit-to-crack transition for the case of wide and shallow pit

The second pit morphology considered in this study is the subsurface pit. As shown in Fig. 78, pit-to-crack transition occurs around time = 11 μs at approximately the left corner of the pit base (i.e. zone 1 in Fig. 79). At this time it is also possible to notice the vertical contraction of the plate caused by horizontal opening load and the Poisson's effect. As time goes by, the crack continues to propagate along the grain boundaries of the material. Around time = 13 μs, a subsurface crack nucleates in proximity to zone 2 in Fig. 79 (vid. Fig. 78), which remains subsurface probably due to the shielding effect provided by the zone 1 initial corrosion damage shown in Fig. 79. At time = 14 μs, a secondary crack nucleates in proximity to the lower left edge of the plate, which is probably due to the vertical contraction of the material and the vertical displacement constrain applied along the left edge of the plate. This is in contrast to the previous case (vid. Fig. 77), where the closest grain boundary to the lower edge of the plate was at its right edge, and, as a result, the secondary crack propagated in proximity to the right edge of the plate.

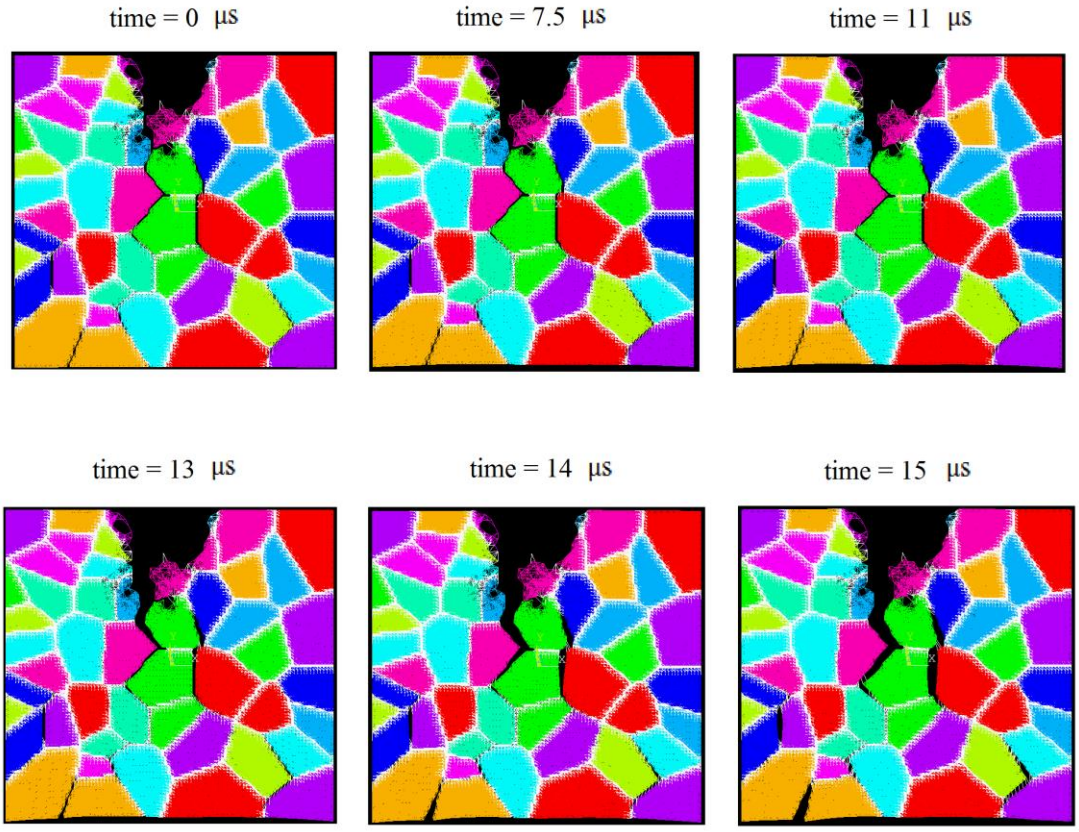

Fig. 78 Pit-to-crack transition for the case of subsurface pit

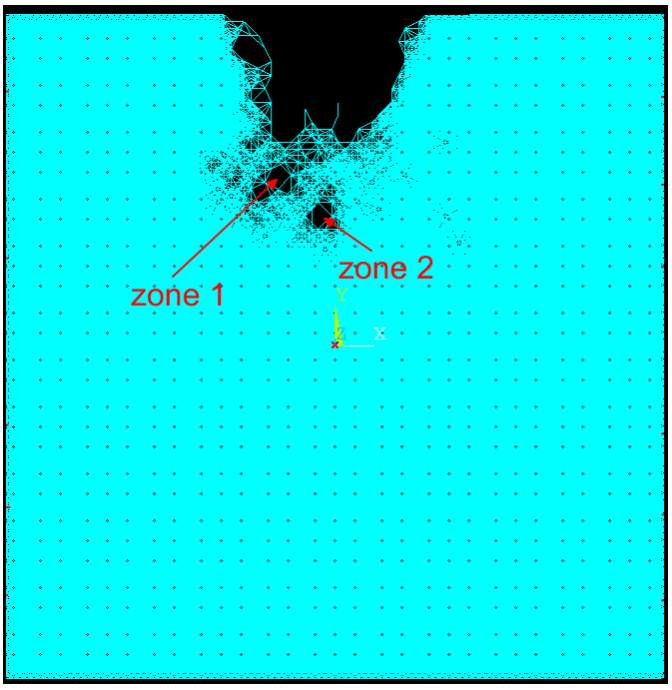

Fig. 79 Corrosion damage before the application of the mechanical load for the subsurface pit

The last pit morphology investigated in this study is the undercutting pit. As shown in Fig. 80, pit-to-crack transition occurs around time = 10 μs at the lower end of the left pit shoulder. At this time it is also possible to notice the vertical contraction of the plate caused by horizontal opening load and the Poisson's effect. As time goes by, the crack continues to propagate along the grain boundaries of the material. Around time = 14 μs, a secondary internal crack nucleates in proximity to the lower right edge of the plate.

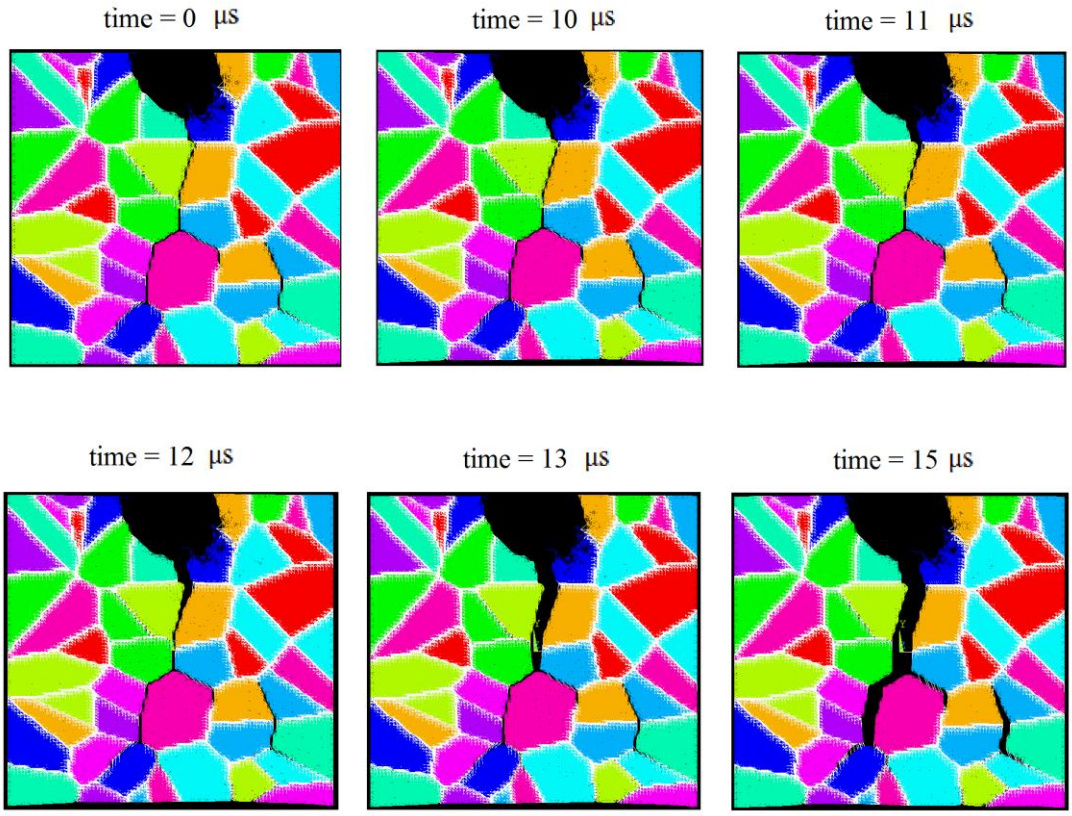

Fig. 80 Pit-to-crack transition for the case of undercutting pit

7.5 Gaps and future work

Since the PD model of pit-to-crack transition described in this chapter is obtained by coupling the PD model of cubic polycrystals (Chapter 4) and the PD model of pitting corrosion (Chapter 6), the future work, gaps and limitations that are applicable to these two PD models also apply to the PD model of pit-to-crack transition. The list here below summarises additional gaps and limitations:

- Pit evolution and crack propagation are predicted in separate phases. In other words, during the prediction of pit evolution (first phase), there is no mechanical load applied to the body, while, during the prediction of crack propagation, there is no pit evolution (i.e. metal dissolution). Therefore, the effect of the stress field, which is often found to encourage metal dissolution, is neglected. Moreover, if the timescale of crack propagation is equal or

greater to that of metal dissolution, the former phenomenon can have a significant impact on the overall process of material fracturing. This effect is also neglected by the current approach. Therefore, the model here described can be applied to all those practical applications where the stress field has a limited influence on metal dissolution and the timescale of crack propagation is much smaller than that of metal dissolution.

- Other mechanical loading conditions can be investigated.
- The onset, propagation and interaction of multiple cracks generated from corrosion pits can be investigated.

7.6 Summary

High stress regions around corrosion pits can lead to crack nucleation and propagation. In fact, in many engineering applications, corrosion pits act as precursor to cracking, but prediction of structural damage has been hindered by lack of understanding of the process by which a crack develops from a pit and limitations in visualisation and measurement techniques. An experimental approach able to accurately quantify the stress and strain field around corrosion pits is still lacking. For long cracks, standards for quantifying environment-assisted crack growth rates can be found. However, in relation to the growth rate of small cracks emerging from corrosion pits, there are no standards to guide the measurement process. In this regard, numerical modelling can be helpful. Several numerical models, usually based on FEM, are available for predicting the evolution of long cracks. However, the methodology for dealing with the nucleation of damage is less well developed, and, often, numerical instabilities arise during the simulation of crack propagation. Moreover, the popular assumption that the crack has the same depth as the pit at the point of transition and by implication initiates at the pit base, has no intrinsic foundation. The numerical approach described in this chapter can model nucleation and propagation of cracks without being affected by any numerical instability, and does not need to assume crack initiation from the base of the pit.

The couple material/environment considered in this study is austenitic stainless steel grade 304 exposed to 1M NaCl aqueous solution. Pitting corrosion is predicted by using the PD pitting corrosion model described in Chapter 6, while the PD micro-mechanical model described in Chapter 4 is used to predict intergranular crack propagation. Future work should focus on all the points already mentioned for these two models. On top of that, the following considerations can be added for the PD model of pit-to-crack transition: 1) the modules of pit evolution and crack propagation can be fully coupled, 2) other loading conditions can be considered to better investigate crack nucleation from the pit shoulder and pit mouth and 3) the interaction of multiple corrosion pits can be investigated. To the best of the author's knowledge, no PD model of pit-to-crack transition is currently available in the literature (De Meo & Oterkus 2016).

8 Conclusions

8.1 Achievements against the objectives

The ultimate goal of this research was to use peridynamics to produce non-conventional and more effective numerical frameworks that can be helpful in failure analysis and in the design of new fracture-resistant and corrosion-resistant materials. The list here below summarises the main achievements of this work, which are in line with the research objectives:

- A peridynamic model for the prediction of fracture of polycrystalline materials was created. Complex fracture phenomena such as crack nucleation and crack branching have been modelled without using any external fracture criterion or experiencing any numerical instability, and a satisfactory quantitative and qualitative agreement with other numerical data was found. The effect of different microstructural features on the fracture behaviour of the material was investigated. This framework was, then, used as a starting point for the creation of the PD models of SCC and pit-to-crack transition.

- A peridynamic model for the prediction of hydrogen grain boundary diffusion, embrittlement, and resulting SCC, was created. Crack propagation speeds calculated for five different loading conditions were found to be in good qualitative and quantitative agreement with the experimental data available in the literature. Remarkably, the peridynamic model of SCC was also capable of capturing the fracture behaviour of the structure, and different micro-branching behaviours and associated geometrical features (i.e. micro-branching width) observed in experiments.

- A peridynamic model of pitting corrosion damage was created by extending an already existing PD framework to allow for 1) the reproduction of realistic pitting morphologies, 2) the modelling of microstructural effects

such as the presence of intermetallic particles and 3) the reduction of the computational cost of the simulations. A satisfactory qualitative and quantitative agreement with experimental data and other numerical results available in the literature was found. This framework was, then, used as starting point for the creation of the PD model of pit-to-crack transition.

- A peridynamic model of pit-to-crack transition was created by coupling the PD models of pitting corrosion and fracture in polycrystalline materials.

8.2 Gaps and recommended future work

Despite the realistic appearance of the microstructures analysed in this work, a random and artificial procedure was used for their realisation. Instead, experimental techniques can be coupled to the present approach to reproduce and investigate real microstructures.

Parallel computing and multiscale approaches can be used to reduce the computational cost of the simulations and for allowing the modelling of problems having greater dimension, lengthscale and timescale.

Concerning the PD model of fracture in polycrystalline materials, further investigations are necessary to understand the shielding and GBC effect on the time-to-failure of steel pre-cracked plates.

Concerning the PD model of SCC, experimental validation is required for the values of fracture initiation time.

Concerning the PD model of pitting corrosion, experimental validation is required for the diffusion-controlled regime. Moreover, the numerical framework could be extended by modelling passive film degradation and repassivation mechanisms. The model needs also to become fully autonomous in the prediction of different pit morphologies. Finally, validation is required for the 2D models.

Concerning the PD model of pit-to-crack transition, the modules of pit evolution and crack propagation can be coupled. Moreover, other loading conditions can be considered to better investigate crack nucleation from the pit shoulder and pit mouth. Finally the interaction of multiple corrosion pits can be investigated.

8.3 Novelty and contribution to the field

Polycrystalline materials are among the most common materials used in practical engineering applications. Owing to the high number of microstructural variables affecting the fracture behaviour of this class of materials, the task of designing safe structures without abusing the use of safety factors is often challenging. Despite the resulting valuable information provided by experimental approaches, these techniques are not always viable. Therefore, computational approaches represent a precious complement for understanding the fracturing of polycrystalline materials. However, the mathematical modelling of the transition from microscopic defects to macroscopic cracks is not entirely understood at present, and the numerical approaches currently employed suffer from several limitations. The study described in Chapter 4 demonstrates that PD can overcome some of these limitations and is a valuable numerical tool for the modelling of fracture in polycrystalline materials. The literature was lacking of such a framework, whose formulation can now be found in (De Meo, Zhu, et al. 2016) and can be used for the microstructural design of fracture-resistant materials.

A wide range of systems related to different industries are affected by SCC. The published literature abounds with SCC experimental data, but their usefulness is limited by the large amount of parameters contributing to the phenomenon. Moreover, the numerical techniques currently available suffer from various limiting factors. The study described in Chapter 5 demonstrates that PD can overcome most of these shortcomings, and can predict detailed and realistic geometrical features concerning SCC damage in polycrystalline materials (i.e. stable crack propagation, micro-branching and the resulting penetration of the corrosive solution within the

structure) that facilitates hydrogen diffusion and accelerates the degradation of the material, which is a salient aspect in real cases. The literature was lacking of such a framework, whose formulation can now be found in (De Meo, Diyaroglu, et al. 2016) and can be used for the prediction of crack propagation rates of structures affected by SCC.

Pitting corrosion negatively affects several industries and structures, and is the most common, dangerous and destructive type of corrosion in marine and offshore structures. Due to material inhomogeneities, pits can evolve in very different shapes. Despite the significant improvements in the understanding of pitting corrosion, many aspects of this phenomenon remain unclear, corrosion rate prediction based on experimental data remains difficult and experimental measurements of corrosion rates under different electrochemical conditions can be complex and time consuming. In order to overcome some of these limitations, numerical approaches can be a valuable complement. However, due to the fact that the majority of corrosion deterministic models currently available only consider diffusion within the electrolyte solution, none of these models have been able to predict corrosion subsurface damage, which is a phenomenon documented in the experimental literature. The study described in Chapter 6 demonstrates that PD can overcome this shortcoming. Moreover, it can be used to simulate the formation of realistic pit morphologies and the effect of various microstructural features, e.g. intermetallic particles, and the novel approach used to solve the governing equations describing the problem can lead to significant reductions in computational time. The literature was lacking of such a framework, which can be used for failure analysis purposes and for the microstructural design of new pitting-resistant materials.

High stress regions around corrosion pits can lead to crack nucleation and propagation. In fact, in many engineering applications, corrosion pits act as precursor to cracking, but prediction of structural damage has been hindered by lack of understanding of the process by which a crack develops from a pit and limitations in visualisation and measurement techniques. An experimental approach able to

accurately quantify the stress and strain field around corrosion pits is still lacking. For long cracks, standards for quantifying environment-assisted crack growth rates can be found. However, in relation to the growth rate of small cracks emerging from corrosion pits, there are no standards to guide the measurement process. In this regard, numerical modelling can be helpful. Several numerical models, usually based on FEM, are available for predicting the evolution of long cracks. However, the methodology for dealing with the nucleation of damage is less well developed, and, often, numerical instabilities arise during the simulation of crack propagation. Moreover, the popular assumption that the crack has the same depth as the pit at the point of transition and by implication initiates at the pit base, has no intrinsic foundation. The study described in Chapter 7 demonstrates that PD can overcome these shortcomings, and can be used to model the nucleation and propagation of cracks without being affected by any numerical instability, and does not need to assume crack initiation from the base of the pit. The literature was lacking of such a framework, which can be used as a starting point for the development of a model that can be used for failure analysis, microstructural design and asset integrity assessments (De Meo & Oterkus 2016).

8.4 Research outputs

- **Journal papers**

  De Meo, D., Diyaroglu, C., et al., 2016. Modelling of stress-corrosion cracking by using peridynamics. *International Journal of Hydrogen Energy*, 41, pp.6593–6609.

  De Meo, D., Zhu, N. & Oterkus, E., 2016. Peridynamic Modeling of Granular Fracture in Polycrystalline Materials. *Journal of Engineering Materials and Technology*, 138, pp. 1-16.

Zhu, N., De Meo, D. & Oterkus, E., 2016. Ordinary-State Based Peridynamic Modeling of Fracture in Polycrystalline Materials. To be submitted to *Materials.* (Under review)

De Meo, D. & Oterkus, E., 2016. Finite Element Implementation of Peridynamic Pitting Corrosion Damage Model. To be submitted to *Ocean Engineering.* (Under review)

De Meo, D. & Oterkus, E., 2016. Modeling of the onset, propagation and interaction of multiple cracks generated from corrosion pits by using peridynamics. *Journal of Engineering Materials and Technology*. (Under review)

- **Conference papers/presentations**

De Meo, D. et al., 2017. Peridynamics for Predicting Pit-to-Crack Transition. The 58th AIAA/ASCE/AHS/ASC Structures, Structural Dynamics, and Materials Conference. Gaylord Texan, Grapevine, Texas.

De Meo, D. et al., 2015. Multiphysics Modelling of Stress Corrosion Cracking by Using Peridynamics. In C. Guedes Soares & R. A. Shenoi, eds. *5th International Conference on Marine Structures - MARSTRUCT*. Southampton: Taylor & Francis, pp. 499–504.

Diyaroglu, C., De Meo, D. & Oterkus, E., 2015. A Computational Framework for Underwater Shock Response of Marine Structures. In C. Guedes Soares & R. A. Shenoi, eds. *5th International Conference on Marine Structures - MARSTRUCT*. Southampton: Taylor & Francis, pp. 131–138.

Oterkus, E., De Meo, D., Zhu, N. & Diyaroglu, C., 2015. Stress Corrosion Cracking Modelling by Using Peridynamics. *ASME 2015 International Mechanical Engineering Congress & Exposition*. Houston, TX, USA.

Oterkus, E., De Meo, D. & Diyaroglu, C., 2015. Peridynamic Modelling of Granular Fracture in Polycrystalline Materials. *Sustainable Industrial Processing Summit & Exhibition*. Aifantis International Symposium, Antalya, Turkey.

Oterkus, E., De Meo, D., 2014. Multiscale Damage Modeling by Using Peridynamic Theory. *Defence Science and technology Laboratory (Dstl) exposition*. Glasgow, UK.

Oterkus, E., De Meo, D., 2014. Peridynamic Modelling of Hydraulic Fracturing. *Oil & Gas institute*. Glasgow, UK.

Oterkus, E., Amir Siddiq, M., De Meo, D. & Diyaroglu, C., 2014. Multiscale Damage Modeling by Using Peridynamic Theory. *Dstl exposition*. Glasgow, UK.

Oterkus, E., De Meo, D., 2014. Peridynamic Modelling of Materials and Structures. *Centre for Defence and enterprise (CDE) meeting*. London, UK.

- **Chapter books**

  Oterkus, E., Diyaroglu, C., De Meo, D. and Allegri G., 2016. Fracture modes, damage tolerance and failure mitigation in marine composites. In *Marine Applications of Advanced Fibre-Reinforced Composites*. Elsevier, pp. 79–103.

- **Research projects and collaborations**

  This research has contributed to the joint industry and research project "Multiscale Modelling of Stress-Corrosion Cracking by Using Peridynamics" (Grant No.: CDE35174).

This research has contributed, and continues to contribute, to the research collaboration between the Commonwealth Scientific and Industrial Research Organisation (CSIRO) Manufacturing Division in Clayton (Melbourne) and the University of Strathclyde, concerning the numerical modeling of pit-to-crack transition in aerospace vehicles.

8.5 Final remarks

The results obtained from this study support the idea that peridynamics, thanks to its non-conventional mathematical formulation, is a valuable and effective tool for the modelling of structural damage produced by various forms of localised corrosion. The numerical models produced as part of this research can, thus, be helpful in failure analysis and in the microstructural design of new fracture-resistant and corrosion-resistant materials.

Appendix A: Bond constants derivation for the PD micro-mechanical model

The aim of this appendix is to describe the derivation of the expression for type-1 bond constant c_{T1} and type-2 bond constant c_{T2} used in the peridynamic micro-mechanical model of cubic crystals.

As already shown in Section 4.4, three independent material constants, namely c_{11}, c_{12} and c_{44}, are necessary to fully describe the micro-mechanical response of the cubic crystal. Therefore, three independent peridynamic material constants would be necessary. Nevertheless, for the sake of simplicity, the current peridynamic micro-mechanical model is described by two independent material constants only, namely c_{T1} and c_{T2}. According to the procedure here described, a body under study is subjected to three independent loading conditions. The resulting PD and CCM strain energy densities are equated and the solution of the resulting equations leads to the PD micro-mechanical properties c_{T1} and c_{T2}. The following three subsections describe in detail the three different loading conditions and the relevant calculations.

First loading condition

The first loading condition consists in the application of a constant strain along direction-1 which, in this particular case, is equal to direction-*x*. (Fig. A.1):

$$\varepsilon_{11} = \zeta = 0.001 \qquad \varepsilon_{22} = 0.0 \qquad \gamma_{12} = 0.0 \tag{66}$$

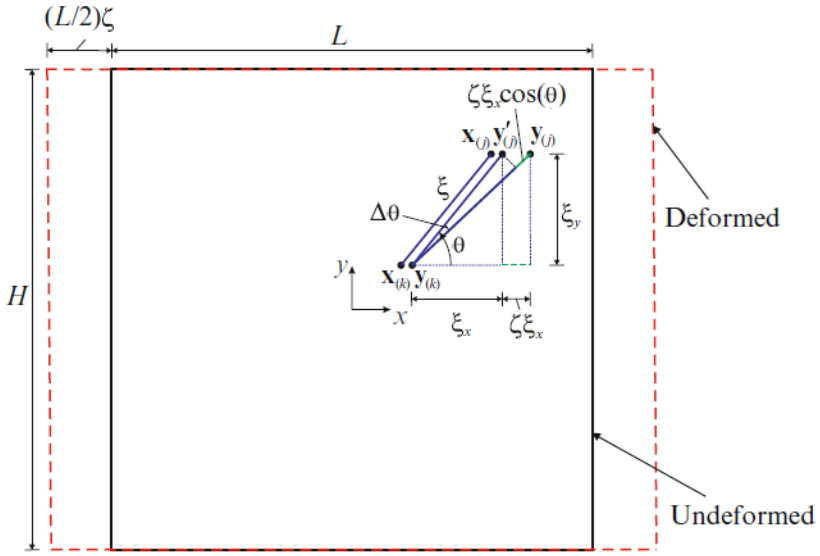

Fig. A.1 First loading condition

Since $\zeta << 1$, $\cos(\Delta\theta) \cong \cos(0) = 1$ and $\sin(\Delta\theta) \cong \sin(0) = 0$. By means of simple geometrical considerations, the bond length in the deformed configuration and the stretch can be calculated as shown in Fig. A.1:

$$l_{def} = l_{undef} + \zeta \cdot \xi_x \cdot \cos(\theta) = l_{undef} \cdot (1 + \zeta \cdot \cos^2(\theta)) \tag{67}$$

$$s = \frac{\Delta l}{l_{undef}} = \frac{l_{def} - l_{undef}}{l_{undef}} = \zeta \cdot \cos^2(\theta) \tag{68}$$

As described in (Silling & Askari 2005), the PD strain energy density associated with a generic material point can be written as

$$W_{PD} = \frac{1}{2} \cdot \int_{H_x} w \cdot dV \tag{69}$$

The micro-potential function *w* represents the strain energy accumulated in a single peridynamic bond due to the application of external loads on the body. It can be calculated by using the analogy of the well-known formula for the strain energy stored in a tensioned single spring as:

$$w = \frac{1}{2} \cdot c \cdot s^2 \cdot l_{\text{undef}} \tag{70}$$

Considering a neighbourhood H_x of disk shape, whose thickness equals the thickness of the plate *h*, the infinitesimal volume has the following expression:

$$dV = (\xi \cdot d\theta) \cdot d\xi \cdot h \tag{71}$$

Considering the contribution of both type-1 and type-2 bond constants, the expression of the peridynamic strain energy density for a generic material point *i* can be written as follows:

$$\begin{aligned} W_{PD}(i) = {} & \frac{1}{4} \cdot c_{T1} \cdot h \cdot \zeta^2 \cdot \int_0^{\delta} \xi^2 \cdot d\xi \cdot \int_0^{2 \cdot \pi} \cos^4(\theta)\, d\theta + \\ & \frac{1}{4} \cdot c_{T2} \cdot \zeta^2 \cdot \cos^4(\vartheta_A) \cdot \sum_{j=1}^{qA} \xi_{ij} \cdot V_j + \\ & \frac{1}{4} \cdot c_{T2} \cdot \zeta^2 \cdot \cos^4(\vartheta_B) \cdot \sum_{j=1}^{qB} \xi_{ij} \cdot V_j \end{aligned} \tag{72}$$

Consider the definition of the following parameters β_A and β_B:

$$\beta_A = \sum_{j=1}^{q_A} \xi_{ij} V_j \tag{73}$$

$$\beta_B = \sum_{j=1}^{q_B} \xi_{ij} V_j \tag{74}$$

where subscript *A* is associated with directions $\theta = \frac{\pi}{4}, \frac{5}{4}\pi$, whilst subscript *B* is associated with directions $\theta = \frac{3}{4}\pi, \frac{7}{4}\pi$. In Eqs. 72-73, i and j refer to a generic particle and its family member respectively, V_j denotes the volume of particle j, ξ_{ij} is the initial length of the bond between particles i and j, and q_A and q_B

represent the number of PD bonds along the directions associated with A and B, respectively.

After performing the integrations given in Eq. (72), the PD strain energy density can be rewritten as

$$W_{PD}(i) = \frac{1}{4}\cdot c_{T1}\cdot h\cdot \zeta^2 \cdot \frac{\delta^3}{3}\cdot\frac{3}{4}\cdot\pi + \frac{1}{4}\cdot c_{T2}\cdot\zeta^2\cdot 0.25\cdot\beta_A + \frac{1}{4}\cdot c_{T2}\cdot\zeta^2\cdot 0.25\cdot\beta_B \tag{75}$$

With few more simplifications, the final expression can be obtained as

$$W_{PD}(i) = \frac{1}{4}\cdot c_{T1}\cdot h\cdot \zeta^2 \cdot \frac{\delta^3}{3}\cdot\frac{3}{4}\cdot\pi + \frac{1}{4}\cdot c_{T2}\cdot\zeta^2\cdot 0.25\cdot(\beta_A+\beta_B) \tag{76}$$

The next step is to write the expression of the strain energy density according to CCM. In the case of a model with a two-dimensional simplification, the reduced global stiffness matrix [Q] of a cubic crystal can be written as

$$\begin{bmatrix}\sigma_{11}\\ \sigma_{22}\\ \tau_{12}\end{bmatrix} = \begin{bmatrix}Q_{11} & Q_{12} & 0\\ Q_{12} & Q_{11} & 0\\ 0 & 0 & Q_{44}\end{bmatrix}\cdot\begin{bmatrix}\varepsilon_{11}\\ \varepsilon_{22}\\ \gamma_{12}\end{bmatrix} \tag{77}$$

According to CCM, the expression of strain energy density can be written as

$$W_{CCM} = \frac{1}{2}\cdot(\sigma_{11}\cdot\varepsilon_{11}+\sigma_{22}\cdot\varepsilon_{22}+\tau_{12}\cdot\gamma_{12}) \tag{78}$$

This can be rewritten for the first loading condition as

$$W_{CCM} = \frac{1}{2}\cdot\sigma_{11}\cdot\varepsilon_{11} = \frac{1}{2}\cdot Q_{11}\cdot\varepsilon_{11}^2 = \frac{1}{2}\cdot Q_{11}\cdot\zeta^2 \tag{79}$$

The first equation of our system is obtained by equating PD and CCM strain energy density expressions:

$$\frac{1}{16}\cdot c_{T1}\cdot h\cdot\zeta^2\cdot\delta^3\cdot\pi+\frac{1}{4}\cdot c_{T2}\cdot\zeta^2\cdot 0.25\cdot(\beta_A+\beta_B)=\frac{1}{2}\cdot Q_{11}\cdot\zeta^2 \qquad (80)$$

Second loading condition

The second loading condition consists in the application of a constant strain along both direction-1 and direction-2 (Fig. A.2). In this particular case, direction-1 is equal to direction-*x* and direction-2 is equal to direction-*y*.

$$\varepsilon_{11}=\zeta=0.001 \qquad \varepsilon_{22}=\zeta=0.001 \qquad \gamma_{12}=0.0 \qquad (81)$$

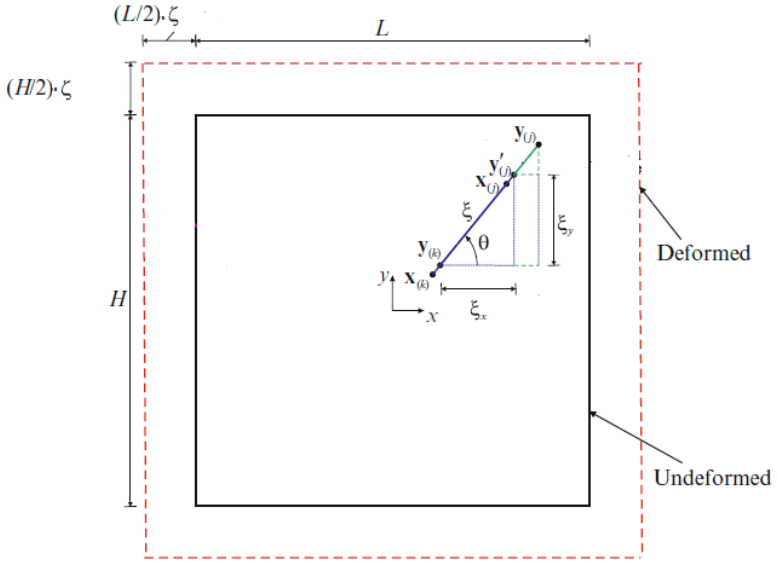

Fig. A.2 Second loading condition

By means of simple geometrical considerations, it is possible to derive the following expression for the generic bond length and stretch in the deformed configuration:

$$l_{def}=l_{undef}+l_{undef}\cdot\zeta\cdot(\sin^2(\theta)+\cos^2(\theta)) \qquad (82)$$

$$s = \frac{l_{def} - l_{undef}}{l_{undef}} = \zeta \cdot (\sin^2(\theta) + \cos^2(\theta)) \tag{83}$$

Similar to (A.6), the PD strain energy density can be written as

$$\begin{aligned} W_{PD}(i) &= \frac{1}{4} \cdot c_{T1} \cdot h \cdot \zeta^2 \cdot \int_0^{\delta} \xi^2 \cdot d\xi \cdot \\ &\left(\int_0^{2\cdot\pi} \cos^4(\theta)\, d\theta + \int_0^{2\cdot\pi} \sin^4(\theta)\, d\theta + 2 \cdot \int_0^{2\cdot\pi} \cos^2(\theta) \cdot \sin^2(\theta)\, d\theta \right) + \\ &+ \frac{1}{4} \cdot c_{T2} \cdot \zeta^2 \cdot \left(\cos^4(\vartheta_A) + \sin^4(\vartheta_A) + 2 \cdot \cos^2(\vartheta_A) \cdot \cos^2(\vartheta_A) \right) \cdot \beta_A + \\ &+ \frac{1}{4} \cdot c_{T2} \cdot \zeta^2 \cdot \left(\cos^4(\vartheta_B) + \sin^4(\vartheta_B) + 2 \cdot \cos^2(\vartheta_B) \cdot \cos^2(\vartheta_B) \right) \cdot \beta_B \end{aligned} \tag{84}$$

This can be further simplified as

$$W_{PD}(i) = \frac{1}{4} \cdot c_{T1} \cdot h \cdot \zeta^2 \cdot \frac{\delta^3}{3} \cdot 2\pi + \frac{1}{4} \cdot c_{T2} \cdot \zeta^2 \cdot (\beta_A + \beta_B) \tag{85}$$

Recalling (A.12), CCM strain energy density can be written for this loading condition as

$$W_{CCM} = \frac{1}{2} \cdot (\sigma_{11} \cdot \varepsilon_{11} + \sigma_{22} \cdot \varepsilon_{22}) = \sigma_{11} \cdot \varepsilon_{11} = (Q_{11} + Q_{12}) \cdot \zeta^2 \tag{86}$$

By equating PD and CCM expressions, the second equation of our system can be written as

$$\frac{1}{6} \cdot c_{T1} \cdot h \cdot \zeta^2 \cdot \delta^3 \cdot \pi + \frac{1}{4} \cdot c_{T2} \cdot \zeta^2 \cdot (\beta_A + \beta_B) = (Q_{11} + Q_{12}) \cdot \zeta^2 \tag{87}$$

Third loading condition

The third loading condition consists of the application of a constant simple shear strain (Fig. A.3):

$$\varepsilon_{11} = 0.0 \qquad \varepsilon_{22} = 0.0 \qquad \gamma_{12} = 0.001 = \zeta \tag{88}$$

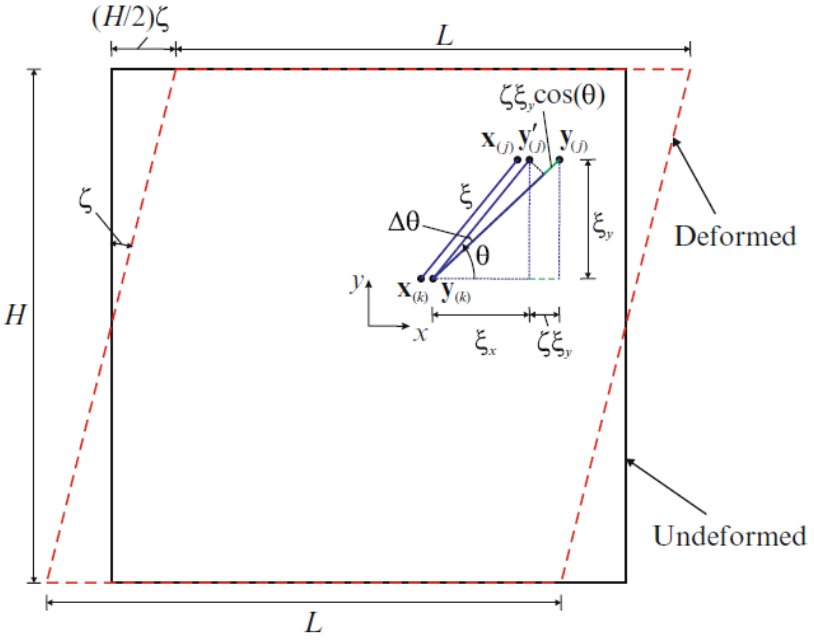

Fig. A.3 Third loading condition

Since $\zeta << 1$, $\cos(\Delta\theta) \cong \cos(0) = 1$ and $\sin(\Delta\theta) \cong \sin(0) = 0$. By means of simple geometrical considerations, the bond length and stretch in the deformed configuration can be calculated as

$$l_{def} = l_{undef} \cdot \left(1 + \zeta \cdot \cos(\theta) \cdot \sin(\theta)\right) \tag{89}$$

$$s = \frac{\Delta l}{l_{undef}} = \frac{l_{def} - l_{undef}}{l_{undef}} = \zeta \cdot \cos(\theta) \cdot \sin(\theta) \tag{90}$$

The PD strain energy density for this loading condition can be written as

$$W_{PD}(i)=\frac{1}{4}\cdot c_{T1}\cdot h\cdot\zeta^2\cdot\int_0^{\delta}\xi^2\cdot d\xi\cdot\int_0^{2\cdot\pi}\cos^2(\theta)\cdot\sin^2(\theta)\cdot d\theta+$$
$$+\frac{1}{4}\cdot c_{T2}\cdot\zeta^2\cdot\cos^2(\vartheta_A)\cdot\sin^2(\vartheta_A)\cdot\beta_A+ \tag{91}$$
$$+\frac{1}{4}\cdot c_{T2}\cdot\zeta^2\cdot\cos^2(\vartheta_B)\cdot\sin^2(\vartheta_B))\cdot\beta_B$$

The calculation of the integrals leads to the following expression:

$$W_{PD}(i)=\frac{1}{4}\cdot c_{T1}\cdot h\cdot\zeta^2\cdot\frac{\delta^3}{3}\cdot\frac{\pi}{4}+\frac{1}{4}\cdot c_{T2}\cdot\zeta^2\cdot\frac{1}{4}(\beta_A+\beta_B) \tag{92}$$

With few more simplification, it can be rewritten as

$$W_{PD}(i)=\frac{1}{48}\cdot c_{T1}\cdot h\cdot\zeta^2\cdot\delta^3\cdot\pi+\frac{1}{16}\cdot c_{T2}\cdot\zeta^2\cdot(\beta_A+\beta_B) \tag{93}$$

Recalling (A.12), CCM strain energy density for this loading condition can be written as

$$W_{CCM}=\frac{1}{2}\cdot(\tau_{12}\cdot\gamma_{12})=\frac{1}{2}\cdot Q_{44}\cdot\zeta^2 \tag{94}$$

By equating PD and CCM strain energy densities, the third equation of the system can be written as

$$\frac{1}{2}\cdot Q_{44}\cdot\zeta^2=\frac{1}{48}\cdot c_{T1}\cdot h\cdot\zeta^2\cdot\delta^3\cdot\pi+\frac{1}{16}\cdot c_{T2}\cdot\zeta^2\cdot(\beta_A+\beta_B) \tag{95}$$

The solution of the system constituted by the three equations (80), (87) and (95) leads to the following expressions for the peridynamic micro-mechanical material parameters:

$$c_{T1}=\frac{12\cdot(Q_{11}-Q_{44})}{\pi\cdot h\cdot\delta^3}\qquad c_{T2}=\frac{4\cdot(3\cdot Q_{44}-Q_{11})}{\beta_A+\beta_B}\qquad Q_{44}=Q_{12} \tag{96}$$

In the case of plane stress configuration:

$$Q_{11} = \frac{c_{11}^2 - c_{12}^2}{c_{11}} \qquad Q_{12} = \frac{c_{11}c_{12} - c_{12}^2}{c_{11}} \tag{97}$$

which results in:

$$c_{T1} = \frac{12(c_{11}^2 - c_{11}c_{12})}{\pi h \delta^3 c_{11}} \qquad c_{T2} = \frac{4(3c_{11}c_{12} - 2c_{12}^2 - c_{11}^2)}{(\beta_A + \beta_B)c_{11}} \tag{98}$$

In case of plane strain configuration:

$$Q_{11} = c_{11} \qquad Q_{12} = c_{12} \tag{99}$$

Resulting in:

$$c_{T1} = \frac{12 \cdot (c_{11} - c_{12})}{\pi \cdot h \cdot \delta^3} \qquad c_{T2} = \frac{4 \cdot (3 \cdot c_{12} - c_{11})}{\beta_A + \beta_B} \tag{100}$$

Since the quantities β_A and β_B depend on the grain orientation γ, the mechanical behaviour of each crystal is potentially different with respect to that of its neighbouring crystals.

Appendix B: Crack tip analysis for the SCC model

The aim of this appendix is to describe the method used to calculate the magnitude of the vertical enforced displacement "*u*" necessary to generate the desired values of SIF.

Since the model is symmetric along the horizontal direction, only the top half of the plate is modelled by using ANSYS 14.5 (Fig. B.1). The material is considered isotropic, its microstructure is disregarded, symmetric boundary conditions are applied along the bottom edge to mimic the bottom half of the plate, horizontal constraints are applied along the left edge, the vertical enforced displacement "*u*" is applied along the top edge of the plate and the resulting stress intensity factor is calculated by using ANSYS postprocessor. To capture the rapidly varying stress and deformation fields, the mesh is skewed around the crack tip by using the ANSYS command 'KSCON' as shown in Fig. B1. A certain arbitrary "*u*" is applied as above described and the SIF is calculated. The procedure is repeated until the crack tip has the desired value of SIF.

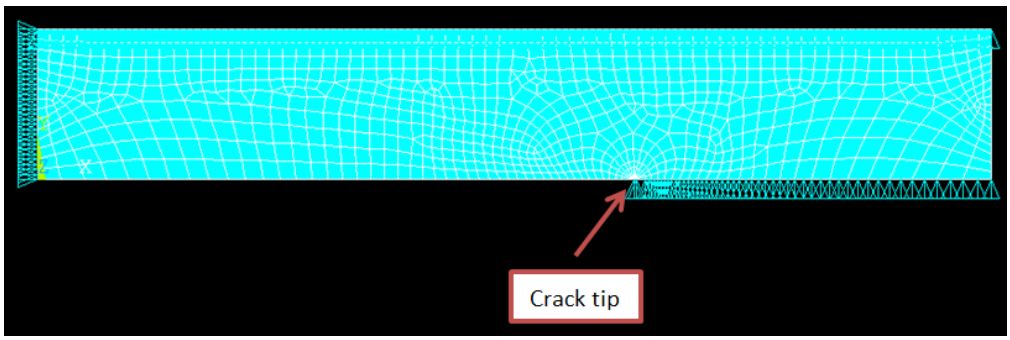

Fig. B1 Mesh and boundary conditions for the top half of the plate

References

Aliabadi, M.H. & Rooke, D.P., 1991. *Numerical Fracture Mechanics*, Computational Mechanics Publications Kluwer Academic Publishers.

Alvaro, A., Olden, V. & Akselsen, O.M., 2014. 3D cohesive modelling of hydrogen embrittlement in the heat affected zone of an X70 pipeline steel. *International Journal of Hydrogen Energy*, 39(18), pp.3528–3541.

Anderson, T.L., 2005. *Fracture Mechanics - Fundamentals and Applications* 3rd ed., Boca Raton: Taylor & Francis.

ANSYS, Mechanical User's Guide. Section 17.2. Available at: http://148.204.81.206/Ansys/150/ANSYS%20Mechanical%20Users%20Guide.pdf

Askari, E. Bobaru, F., Lehoucq, R. B., Parks, M. L., Silling, S. A., Weckner, O., 2008. Peridynamics for multiscale materials modeling. *Journal of Physics: Conference Series*, 125, p.012078.

Barenblatt, G. I., 1962. The mathematical theory of equilibrium cracks in brittle fracture. *Adv Appl Mech*, 7, pp.56–125.

Barsoum, R. S., 1975. Further application of quadratic isoparametric finite elements to linear fracture mechanics of plate bending and general shells. *Internation Journal of Fracture*, 11, pp.167–169.

Bechtle, Kumar, M., Somerday, B. P., Launey, M. E., Ritchie, R. O., 2009. Grain-boundary engineering markedly reduces susceptibility to intergranular hydrogen embrittlement in metallic materials. *Acta Materialia*, 57(14), pp.4148–4157.

Belytschko, T. & Black, T., 1999. Elastic crack growth in finite elements with minimal remeshing. *Int J Numer Meth Eng*, 45, pp.601–620.

Benedetti, I. & Aliabadi, M. H., 2013. A three-dimensional cohesive-frictional grain-boundary micromechanical model for intergranular degradation and failure in polycrystalline materials. *Computer Methods in Applied Mechanics and Engineering*, 265, pp.36–62.

Bhandari, J., Khan, F., Abbassi, R., Garaniya, V., Ojeda, R., 2015. Modelling of pitting corrosion in marine and offshore steel structures - A technical review. *Journal of Loss Prevention in the Process Industries*, 37, pp.39–62.

Black, A. R., Mathiesen, T. & Hilbert, L. R., 2015. *Corrosion protection of offshore wind fundations*. Force technology. NACE 2015.

Bobaru, F., 2007. Influence of van der Waals forces on increasing the strength and toughness in dynamic fracture of nanofibre networks: a peridynamic approach. *Modelling and Simulation in Materials Science and Engineering*, 15, pp.397–417.

Bobaru, F. & Hu, W., 2012. The meaning, selection, and use of the peridynamic horizon and its relation to crack branching in brittle materials. *International Journal of Fracture*, 176, pp.215–222.

Camacho, G. T. & Ortiz, M., 1996. Computational modelling of impact damage in brittle materials. *International Journal of Solids and Structures*, 33, pp.2899–2938.

Chandar, K. R. & Knauss, W. G., 1982. Dynamic crack-tip stresses under stress wave loading - A comparison of theory and experiment. *International Journal of Fracture*, 20, pp.209–222.

Chen, Z. & Bobaru, F., 2015. Peridynamic modeling of pitting corrosion damage. *Journal of the Mechanics and Physics of Solids*, 78, pp.352–381.

Chen, Z., Zhang, G. & Bobaru, F., 2015. The Influence of Passive Film Damage on Pitting Corrosion. *Journal of the Electrochemical Society*, 163(2), pp.C19–C24.

Cicek, V., 2014. Types of Corrosion. In *Corrosion Engineering*. pp. 43–81.

Crocker, A. G., Flewitt, P. E. J. & Smith, G. E., 2005. Computational Modelling of Fracture in Polycrystalline Materials. *International Materials Reviews*, 50(2), pp.99–125.

De Meo, D., Diyaroglu, C., et al., 2016. Modelling of stress-corrosion cracking by using peridynamics. International Journal of Hydrogen Energy, 41, pp.6593–6609

De Meo, D., Zhu, N. & Oterkus, E., 2016. Peridynamic Modeling of Granular Fracture in Polycrystalline Materials. Journal of Engineering Materials and Technology, 138, pp.1-16

De Meo, D. & Oterkus, E., 2016. Modeling of the onset, propagation and interaction of multiple cracks generated from corrosion pits by using peridynamics. Journal of Engineering Materials and Technology. (Under review)

Demmie, P. & Silling, S., 2007. An approach to modeling extreme loading of structures using peridynamics. *Journal of Mechanics of Materials and Structures*, 2, pp.1921–1945.

Duddu, R., 2014. Numerical modeling of corrosion pit propagation using the combined extended finite element and level set method. *Computational Mechanics*, 54, pp.613–627.

Duddu, R., Kota, N. & Qidwai, S., 2015. An extended finite element model of crevice and pitting corrosion. In *IMECE2015-50423*. pp. 1–11.

Dugdale, D. S., 1960. Yielding of steel sheets containing slits. *J Mech Phys Solids*, 8(2), pp.100–104.

Espinosa, H. D. & Zavattieri, P. D., 2002a. *A grain level model for the study of failure initiation and evolution in polycrystalline brittle materials. Part I: Theory and numerical implementation*,

Espinosa, H. D. & Zavattieri, P. D., 2002b. A grain level model for the study of failure initiation and evolution in polycrystalline brittle materials. Part II: Numerical examples. *Mechanics of Materials*, 35, pp.365–394.

Fisher, J. C., 1951. Calculation of diffusion penetration curves for surface and grain boundary diffusion. *Journal of Applied Physics*, 22(1951), pp.74–77.

Foster, J. T., Silling, S. A. & Chen, W. W., 2011. Viscoplasticity using peridynamics. *Int J Numer Meth Eng*, 81(2011), pp.1242–1258.

Gaudet, G. T., Mo, W. T., Hatton, T. A., Tester, J. W., Tily, J., Isaacs, H. S., Newman, R. C., 1986. Mass transfer and electrochemical kinetic interactions in localized pitting corrosion. *AIChE Journal*, 32(6), pp.949–958.

Gavrilov, S., Vankeerberghen, M., Nelissen, G., Deconinck, J., 2007. Finite element calculation of crack propagation in type 304 stainless steel in diluted sulphuric acid solutions. *Corrosion Science*, 49, pp.980–999.

Gerstle, W., Silling, S., Read, D., Tewary, V., Lehoucq, R., 2008. Peridynamic simulation of electromigration. *Computers, Materials and Continua*, 8(2), pp.75–92.

Ghajari, M., Iannucci, L. & Curtis, P., 2014. A peridynamic material model for the analysis of dynamic crack propagation in orthotropic media. *Computer Methods in Applied Mechanics and Engineering*, 276, pp.431–452.

Groeber, M., Haley, B. K., Uchic, M. D., Dimiduk, D. M., Ghosh, S., 2006. 3D reconstruction and characterization of polycrystalline microstructures using a FIB-SEM system. *Materials Characterization*, 57, pp.259–273.

Groysman, A., 2010. *Corrosion for Everybody*, Springer.

Ha, Y. D. & Bobaru, F., 2011. Characteristics of dynamic brittle fracture captured with peridynamics. *Engineering Fracture Mechanics,* 78(6), pp.1156–1168.

Ha, Y. D. & Bobaru, F., 2010. Studies of dynamic crack propagation and crack branching with peridynamics. *International Journal of Fracture,* 162, pp.229–244.

Han, G., He, J., Fukuyama, S., Yokogawa, K., 1998. Effect of strain-induced martensite on hydrogen environment embrittlement of sensitized austenitic stainless steels at low temperatures. *Acta Materialia,* 46(13), pp.4559–4570.

Harrison, L. G., 1961. Influence of dislocations on diffusion kinetics in solids with particular reference to the alkali halides. *Transactions of the Faraday Society*, 57, pp.1191-1199.

Herbig, M., King, A., Reischig, P., Proudhon, H., Lauridsen, E. M., Marrow, J., Buffire, J. Y., Ludwig, W., 2011. 3-D growth of a short fatigue crack within a polycrystalline microstructure studied using combined diffraction and phase-contrast X-ray tomography. *Acta Materialia*, 59, pp.590–601.

Hillerborg, A., Modeer, M. & Petersson, P. E., 1976. Analysis of crack formation and crack growth by means of fracture mechanics and finite elements. *Cem Concr Res*, 6(6), pp.773–781.

Hirose, Y. & Mura, T., 1984a. Growth mechanism of stress corrosion cracking in high strength steel. *Engineering Fracture Mechanics*, 19(6), pp.1057–1067.

Hirose, Y. & Mura, T., 1984b. Nucleation mechanism of stress corrosion cracking from notches. *Engineering Fracture Mechanics*, 19(2), pp.317–329.

Hoeppner, D. W., 2011. Pitting Corrosion : Morphology and Characterization. *Rto-Ag-Avt-140*, pp.5.1–5.16.

Horner, D. A., Connolly, B. J., Zhou, S., Crocker, L., Turnbull, A., 2011. Novel images of the evolution of stress corrosion cracks from corrosion pits. *Corrosion Science*, 53(11), pp.3466–3485.

Hosford, W. F., 1993. *The mechanics of crystals and textured polycrystals*, New York, USA: Oxford University Press.

Hutchinson, W. J., 1989. Mechanisms of toughening in ceramics. *Theoretical and applied mechanics*, pp.139–144.

Isaacs, H. S., Cho, J. H., Rivers, M. L., Sutton, S. R., 1995. In Situ X-Ray Microprobe Study of Salt Layers during Anodic Dissolution of Stainless Steel in Chloride Solution. *Journal of The Electrochemical Society*, 142(4), pp.1111–1118.

Isaacs, H. S., 1973. The Behavior of Resistive Layers in the Localized Corrosion of Stainless Steel. *Journal of The Electrochemical Society*, 120, pp.1456-1462.

Jiang, D. E. & Carter, E. A., 2004. First principles assessment of ideal fracture energies of materials with mobile impurities: implications for hydrogen embrittlement of metals. *Acta Materialia*, 52(16), pp.4801–4807.

Johnson, E., 2001. Simulations of microcracking in the process region of ceramics with a cell model. *International Journal of Fracture*, 111(1978), pp.361–380.

Jothi, S., Croft, T. N. & Brown, S. G. R., 2014. Multiscale multiphysics model for hydrogen embrittlement in polycrystalline nickel. *Journal of Alloys and Compounds*.

Kilic, B., Agwai, A. & Madenci, E., 2009. Peridynamic theory for progressive damage prediction in center-cracked composite laminates. *Composite Structures*, 90(2), pp.141–151.

Kilic, B. & Madenci, E., 2010. Peridynamic theory for thermomechanical analysis. *IEEE Transactions on Advanced Packaging*, 33(1), pp.97–105.

Kilic, B. & Madenci, E., 2009. Structural stability and failure analysis using peridynamic theory. *International Journal of Non-Linear Mechanics*, 44(8), pp.845–854.

Kondo, Y., 1989. Prediction of fatigue crack initiation life based on pit growth. *Corrosion Science*, 45(1), pp.7–11.

Krom, A. H. M., Koers, R. W. J. & Bakker, A., 1999. Hydrogen transport near a blunting crack tip. *Journal of the Mechanics and Physics of Solids*, 47, pp.971–992.

Kuo, H. C. & Landolt, D., 1975. Rotating disc electrode study of anodic dissolution or iron in concentrated chloride media. *Electrochimica Acta*, 20(May), pp.393–399.

Lawn, B., 1993. *Fracture of Brittle Solids* 2nd ed., Cambridge University Press.

Laycock, N. J., White, S. P., Noh, J. S., Wilson, P. T., Newman, R. C., 1998. Perforated Covers for Propagating Pits. *Journal of The Electrochemical Society*, 145(4), pp.1101–1108.

Laycock, N. J. & White, S. P., 2001. Computer simulation of single pit propagation in stainless steel under potentiostatic control. *J. Electrochem. Soc.*, 148, pp.B264–B275.

Liang, Y. & Sofronis, P., 2003. Toward a phenomenological description of hydrogen-induced decohesion at particle/matrix interfaces. *Journal of the Mechanics and Physics of Solids*, 51, pp.1509–1531.

Lin, L., Wang, X. & Zeng, X., 2015. The role of cohesive zone properties on intergranular to transgranular fracture transition in polycrystalline solids. *International Journal of Damage Mechanics*, 0(0), pp.1–16.

Ludwig, W., King, A., Reischig, P., Herbig, M., Lauridsen, E. M., Schmidt, S., Proudhon, H., Forest, S., Cloetens, P., Rolland Du Roscoat, S., Buffiere, J. Y., Marrow, T. J., Poulsen, H. F., 2009. New opportunities for 3D materials science of polycrystalline materials at the micrometre lengthscale by combined use of X-ray diffraction and X-ray imaging. *Materials Science and Engineering A*, 524, pp.69–76.

Lynch, S. P., 2011a. Hydrogen embrittlement (HE) phenomena and mechanisms. In V. S. Raja & T. Shoji, eds. *Stress corrosion cracking - Theory and practice*. Cambridge, UK: Woodhead Publishing Limited.

Lynch, S. P., 2011b. Mechanistic and fractographic aspects of stress-corrosion cracking (SCC). In V. S. Raja & T. Shoji, eds. *Stress corrosion cracking - Theory and practice*. Cambridge, UK: Woodhead Publishing Limited.

Madenci, E. & Oterkus, E., 2014. *Peridynamic theory and its applications*. Springer.

McCafferty, E., 2010. Crevice Corrosion and Pitting. In *Introduction to Corrosion Science*. pp. 263–313.

Mccafferty, E., 2010. *Introduction to Corrosion Science*, Springer.

De Meo, D., Diyaroglu, C., Zhu, N., Oterkus, E., Siddiq, M. A., 2016. Modelling of stress-corrosion cracking by using peridynamics. *International Journal of Hydrogen Energy*, 41, pp.6593–6609.

De Meo, D., Zhu, N., Oterkus, E., 2016. Peridynamic Modeling of Granular Fracture in Polycrystalline Materials. *Journal of Engineering Materials and Technology*.

Mine, Y. & Kimoto, T., 2011. Hydrogen uptake in austenitic stainless steels by exposure to gaseous hydrogen and its effect on tensile deformation. *Corrosion Science*, 53(8), pp.2619–2629.

Mishin, Y. & Herzig, C., 1999. Grain boundary diffusion: recent progress and future research. *Materials Science and Engineering: A*, 260, pp.55–71.

Mitchell, J. A, 2011. *A nonlocal, ordinary, state-based plasticity model for peridynamics*. SANDIA report.

Olden, V., Saai, A., Jemblie, L., Johnsen, R., 2014. FE simulation of hydrogen diffusion in duplex stainless steel. *International Journal of Hydrogen Energy*, 39(2), pp.1156–1163.

Onishi, Y., Takiyasu, J., Amaya, K., Yakuwa, H., Hayabusa, K., 2012. Numerical method for time-dependent localized corrosion analysis with moving boundaries by combining the finite volume method and voxel method. *Corrosion Science*, 63, pp.210–224.

Oriani, R. A. & Josephic, P. H., 1974. Equilibrium aspects of hydrogen-induced cracking of steels. *Acta Metallurgica*, 22(9), pp.1065–1074.

Ortiz, M. & Pandolfi, A., 1999. Finite-deformation irreversible cohesive elements for three dimensional crack-propagation analysis. *International Journal for Numerical Methods in Engineering*, 44, pp.1267–1282.

Oterkus, E., Guven, I. & Madenci, E., 2012. Impact damage assessment by using peridynamic theory. *Central European Journal of Engineering*, 2(4), pp.523–531.

Oterkus, E. & Madenci, E., 2012. Peridynamic Analysis of Fiber-Reinforced Composite Materials. *Journal of Mechanics of Materials and Structures*, 7(1).

Oterkus, S., Madenci, E., Oterkus, E., Hwang, Y., Bae, J., Han, S., 2014. Hygro-Thermo-Mechanical Analysis and Failure Prediction in Electronic Packages by Using Peridynamics. , pp.973–982.

Pidaparti, R. M. & Patel, R. K., 2010. Investigation of a single pit/defect evolution during the corrosion process. *Corrosion Science*, 52(9), pp.3150–3153.

Pidaparti, R. M. & Patel, R. R., 2008. Correlation between corrosion pits and stresses in Al alloys. *Materials Letters*, 62, pp.4497–4499.

Pidaparti, R. M. & Patel, R. R., 2011. Modeling the Evolution of Stresses Induced by Corrosion Damage in Metals. *Journal of Materials Engineering and Performance*, 20(October), pp.1114–1120.

Pidaparti, R. M. & Rao, A. S., 2008. Analysis of pits induced stresses due to metal corrosion. *Corrosion Science*, 50, pp.1932–1938.

Popov, B. N., 2015. Pitting and Crevice Corrosion. In *Corrosion Engineering Principles and Solved Problems*. pp. 290–321.

Pouillier, E., Gourgues, A. F., Tanguy, D., Busso, E. P., 2012. A study of intergranular fracture in an aluminium alloy due to hydrogen embrittlement. *International Journal of Plasticity*, 34, pp.139–153.

Qian, J. & Li, S.F., 2011. Application of Multiscale Cohesive Zone Model to Simulate Fracture in Polycrystalline Solids. *Journal of Engineering Materials and Technology-Transactions of the Asme*, 133(January 2011), pp.1-17.

Rabczuk, T., Bordas, S. & Zi, G., 2010. On three-dimensional modelling of crack growth using partition of unity methods. *Computers & Structures*, 88(23-24), pp.1391–1411.

Raja, V. S. & Shoji, T. eds., 2011. *Stress corrosion cracking - Theory and practice*, Cambridge, UK: Woodhead Publishing Limited.

Rajabipour, A. & Melchers, R. E., 2013. A numerical study of damage caused by combined pitting corrosion and axial stress in steel pipes. *Corrosion Science*, 76, pp.292–301.

Raykar, N. R., Maiti, S. K. & Singh Raman, R. K., 2011. Modelling of mode-I stable crack growth under hydrogen assisted stress corrosion cracking. *Engineering Fracture Mechanics*, 78(18), pp.3153–3165.

Rimoli, J. J., 2009. *A Computational Model for Intergranular Stress Corrosion Cracking*. PhD Thesis. Caltech.

Rimoli, J. J. & Ortiz, M., 2010. A three-dimensional multiscale model of intergranular hydrogen-assisted cracking. *Philosophical Magazine*, 90(917270850), pp.2939–2963.

Rizzo, F. J., 1967. An integral equation approach to boundary value problems of classical elastostatics. *Q.App Math*, 25, pp.83–95.

Rose, J. H., Smith, J. R., Guinea, F., Ferrante, J., 1984. Universal features of the equation of state of metals. *Physical Review B*, 29(6), pp.2963–2969.

Ruhle, M., Evans, A. G. & et al, 1987. Microcrack toughening in alumina/zirconia. *Acta metall.*, 35(11), pp.2701–2710.

Sadd, M. H., 2005. *Elasticity Theory, Applications and Numerics*, Elsevier.

Scheider, I., Pfuff, M., Dietzel, W., 2008. Simulation of hydrogen assisted stress corrosion cracking using the cohesive model. *Engineering Fracture Mechanics*, 75, pp.4283–4291.

Scheiner, S., Hellmich, C., 2009. Finite Volume model for diffusion- and activation-controlled pitting corrosion of stainless steel. *Computer Methods in Applied Mechanics and Engineering*, 198(37-40), pp.2898–2910.

Scheiner, S., Hellmich, C., 2007. Stable pitting corrosion of stainless steel as diffusion-controlled dissolution process with a sharp moving electrode boundary. *Corrosion Science*, 49, pp.319–346.

Serebrinsky, S., Carter, E. A., Ortiz, M., 2004. A quantum-mechanically informed continuum model of hydrogen embrittlement. *Journal of the Mechanics and Physics of Solids*, 52, pp.2403–2430.

Sfantos, G. K., Aliabadi, M. H., 2007a. A boundary cohesive grain element formulation for modelling intergranular microfracture in polycrystalline brittle materials. *International Journal for numerical methods in engineering*, 69, pp.1590–1626.

Sfantos, G. K., Aliabadi, M. H., 2007b. Multi-scale boundary element modelling of material degradation and fracture. *Computer Methods in Applied Mechanics and Engineering*, 196, pp.1310–1329.

Sharland, S. M., 1987. A review of the theoretical modelling of crevice and pitting corrosion. *Corrosion Science*, 27(3), pp.289–323.

Sharland, S. M., Jackson, C.P., Diver, A.J., 1989. A finite-element model of the propagation of corrosion crevices and pits. *Corrosion Science*, 29(9), pp.1149–1166.

Shum, D. K. M., Hutchinson, J.W., 1990. On toughening by microcracks. *Mechanics of Materials*, 9, pp.83–91.

Silling, S. A., Epton, M., Weckner, O., Xu, J., Askari, E., 2007. *Peridynamic states and constitutive modeling*, Journal of Elasticity, pp. 88-151.

Silling, S. A., 2000. Reformulation of elasticity theory for discontinuities and long-range forces. *Journal of the Mechanics and Physics of Solids*, 48, pp.175–209.

Silling, S. A. & Askari, E., 2005. A meshfree method based on the peridynamic model of solid mechanics. *Computers and Structures*, 83, pp.1526–1535.

Silling, S. A. & Bobaru, F., 2005. Peridynamic modeling of membranes and fibers. *International Journal of Non-Linear Mechanics*, 40, pp.395–409.

Silling, S. A. & Askari, A., 2004. Peridynamic modeling of impact damage. In *ASME*. New York, USA, pp. 197–205.

Silling, S.A. & Lehoucq, R.B., 2010. Peridynamic Theory of Solid Mechanics. In H. Aref & E. van der Giessen, eds. *Advances in Applied Mechanics*. Elsevier, pp. 73–168.

Sofronis, P. & McMeeking, R.M., 1989. Numerical analysis of hydrogen transport near a blunting crack tip. *Journal of the Mechanics and Physics of Solids*, 37, pp.317–350.

Song, W., Martin, H. J., Hicks, A., Seely, D., Walton, C. A., Lawrimore, W. B., Wang, P. T., Horstemeyer, M. F., 2014. Corrosion behaviour of extruded

AM30 magnesium alloy under salt-spray and immersion environments. *Corrosion Science*, 78, pp.353–368.

Ståhle, P., Bjerkén, C. & Jivkov, A.P., 2007. On dissolution driven crack growth. *International Journal of Solids and Structures*, 44, pp.1880–1890.

Sukumar, N., Srolovitz, D. J., Baker, T. J., Prévost, J. H. , 2003. Brittle fracture in polycrystalline microstructures with the extended finite element method. *International Journal for Numerical Methods in Engineering*, 56(January 2002), pp.2015–2037.

Suter, T., Webb, E. G., Bohni, H., Alkire, R. C., 2001. Pit initiation on stainless steels in 1 M NaCl with and without mechanical stress. *Journal of the Electrochemical Society*, 148, pp.B174–B185.

Swedlow, J. L., Williams, M. L., Yang, W. H., 1965. Elasto-plastic stresses and strains in cracked plates. In *International Conference Fracture*. pp. (1), 259–282.

Thomas, L. E., Bruemmer, S. M., 2000. High-Resolution Characterization of Intergranular Attack and Stress Corrosion Cracking of Alloy 600 in High-Temperature Primary Water. *Corrosion*, 56(6), pp.572–587.

Toi, Y., Atluri, S. N., 1990. Finite element analysis of static and dynamic fracture of brittle microcracking solids. Part 1: Formulation and simple numerical examples. *International Journal of Plasticity*, 6, pp.166–188.

Tracey, D. M., 1971. Finite elements for determination of crack tip elastic stress intensity factors. *Engineering Fracture Mechanics*, 3, pp.255–266.

Trethewey, K. R., Chamberlain, J., 1995. The theory of aqueous corrosion. In *Corrosion for Science and Engineering*. pp. 69–129.

Turnbull, A., Horner, D. A., Connolly, B. J., 2009. Challenges in modelling the evolution of stress corrosion cracks from pits. *Engineering Fracture Mechanics*, 76(5), pp.633–640.

Turnbull, A., McCartney, L. N., Zhou, S., 2006a. A model to predict the evolution of pitting corrosion and the pit-to-crack transition incorporating statistically distributed input parameters. *Corrosion Science*, 48, pp.2084–2105.

Turnbull, A., McCartney, L.N., Zhou, S., 2006b. Modelling of the evolution of stress corrosion cracks from corrosion pits. *Scripta Materialia*, 54, pp.575–578.

Turnbull, A., Wright, L., Crocker, L., 2010. New insight into the pit-to-crack transition from finite element analysis of the stress and strain distribution around a corrosion pit. *Corrosion Science*, 52(4), pp.1492–1498.

Turnbull, A., 2014. Corrosion pitting and environmentally assisted small crack growth. In *Proceedings of the Royal Society*.

Tvergaard, V., 1990. Effect of fibre debonding in a whisker-reinforced metal. *Materials Science and Engineering A: Structural Materials: Properties, Microstructure and Processing A*, 125, pp.203–213.

Vagbharathi, A. S., Gopalakrishnan, S., 2014. An extended finite-element model coupled with level set method for analysis of growth of corrosion pits in metallic structures. In *Proceedings of the Royal Society A: Mathematical, Physical and Engineering Sciences*.

Walton, J. C., 1990. Mathematical modeling of mass transport and chemical reaction in crevice and pitting corrosion. *Corrosion Science*, 30(8-9), pp.915–928.

Walton, J. C., Cragnolino, G., Kalandros, S. K., 1996. A numerical model of crevice corrosion for passive and active metals. *Corrosion Science*, 38(1), pp.1–17.

Wang, H., Liu, Z., Xu, D., Zeng, Q., Zhuang, Z., 2014. Extended finite element method analysis for shielding and amplification effect of a main crack interacted with a group of nearby parallel microcracks. *International Journal of Damage Mechanics*, 0(0), pp.1–22.

Warren, T. L., Silling, S. A., Askari, A., Weckner, O., Epton, M. A., Xu, J., 2009. A non-ordinary state-based peridynamic method to model solid material deformation and fracture. *International Journal of Solids and Structures*, 46(5), pp.1186–1195.

Van der Weeën, P., Zimer, A. M., Pereira, E. C., Mascaro, L. H., Bruno, O. M., De Baets, B., 2014. Modeling pitting corrosion by means of a 3D discrete stochastic model. *Corrosion Science*, 82, pp.133–144.

Wei, Y.J., Anand, L., 2004. Grain-boundary sliding and separation in polycrystalline metals: Application to nanocrystalline fcc metals. *Journal of the Mechanics and Physics of Solids*, 52, pp.2587–2616.

Wu, Q., Zikry, M. A., 2015. Prediction of diffusion assisted hydrogen embrittlement failure in high strength martensitic steels. *Journal of the Mechanics and Physics of Solids*, 85, pp.143–159.

Xiao, J., Chaudhuri, S., 2011. Predictive modeling of localized corrosion: An application to aluminum alloys. *Electrochimica Acta*, 56(16), pp.5630–5641.

Xu, X., Needleman, A., 1996. Numerical simulations of dynamic crack growth along an interface. *International Journal of Fracture*, 74, pp.289–324.

Yagodzinskyy, Y., Saukkonen, T., Kilpeläinen, S., Tuomisto, F., Hänninen, H., 2010. Effect of hydrogen on plastic strain localization in single crystals of austenitic stainless steel. *Scripta Materialia*, 62, pp.155–158.

Zeng, X. W., Li, S., 2010. A multiscale cohesive zone model and simulations of fracture. *Computer Methods in Applied Mechanics and Engineering*, 199, pp.547–556.

Zhu, L. K., Yan, Y., Qiao, L. J., Volinsky, A. A., 2013. Stainless steel pitting and early-stage stress corrosion cracking under ultra-low elastic load. *Corrosion Science*, 77, pp.360–368.